



**Correlation Study and Control of Mechanical Vibration and
Psychoacoustic Parameters in Hard Disk Drive**

Yichao Ma

Faculty of Science, Agriculture and Engineering

Newcastle University

This thesis is submitted for the degree of

Doctor of Philosophy

March 2018

Abstract

The sound quality of 2.5-inch Hard Disk Drives (HDD) has received an interest in the industry. However, the quantification of human feelings of HDD noise annoyance has rarely been studied. A social survey was conducted to determine how annoying an HDD noise affects people. Jury Test 1 was used to examine the four main classes of annoying HDD noise on the psychoacoustic parameters using multiple regression analysis. The result shows that the Roughness has a significant effect on the annoyance level. The Jury Test 2 using Bradley-Terry-Luce model on the proposed subjective sound paired-comparison was performed on thirteen different sounds (from different HDD showing the four main classes of annoying HDD noise) to quantify the degree of HDD noise annoyance level on sound pressure level and the psychoacoustic parameters for young and old age groups.

However, the noise from HDD mainly comes from its components such as spindle motor, voice coil motor, and other mechanical components enclosed in a small aluminum mechanical casing. Performing noise control on such a small complex system has been a challenge. The conventional approach of using frequency analysis is not sufficient to identify the noise source from the HDD. In this thesis, a detailed mathematical formulation and a noise source identification were demonstrated. The near field experimental results indicated that near-field acoustic holography is an excellent way to identify noise location, amplitude and frequency content of the HDD. Moreover, using near field velocity, the far field sound pressure can be computed. The computed value is well agreeable with the measured far field sound pressure level.

Acknowledgements

I would like to express my gratitude to the many people who have made this thesis possible. First of all, I am sincerely grateful to my PhD main supervisor, Dr. Chin Cheng Siong, for his constant professional guidance and personal inspiration throughout my PhD study. No matter whether it was paper writing, conference preparation or thesis writing, he gave me a lot of sound advice and good suggestions.

I would also like to thank my PhD co-supervisor, Dr. Woo Wai Lok for the guidance and fruitful discussions during monthly meetings. Without the help from my supervisors, I would not have the opportunity to complete the PhD course on time.

I would like to express my special thankfulness to Dr. Tan Yong Jie and Dr. Hong Yi Ren for their professional engineering advice on the hard disk drive structural dynamics. Many thanks also go to Mr. Aravind Pitty and Dr. Sun Hao for their kind help in allocating simulation resources and sharing the simulation experience and knowledge, to my company manager Mr. Lionel Young, director Mr. Ooi Kian Keong and Mr. Niroot Jierapipatanakul for their support and understandings, to Mr. Joseph Lau and Ms Jessica Kuang for their help in coordinating between Economic Development Board Singapore, Newcastle University and Seagate Technology LLC, as well as to all my colleagues in Seagate Singapore Design Center. Furthermore I would like to thank the Seagate Technology LLC for the test facilities and technical advice, and thank the Economic Development Board-Industrial Postgraduate Programme (EDB-IPP) scholarship (BH148500) for the scholarship.

Finally, I would like to express my heartfelt gratitude to my parents and my wife for their unconditional love and support.

Table of Contents

Abstract.....	i
Acknowledgements	iii
Table of Contents	v
List of Figures.....	ix
List of Tables	xiii
List of Abbreviations	xiv
Chapter 1. Introduction	1
1.1. Overview, motivation and background	1
1.1.1. The receiver response of the noise	3
1.1.2. Vibrating body and near field.....	5
1.1.3. Noise propagation	8
1.2. Challenges and outline of the thesis.....	10
Chapter 2. HDD noise annoyance study	11
2.1. Introduction	11
2.2. Social survey of HDD noise	13
2.3. Acoustic Jury Test 1.....	15
2.3.1. Setup for sound sample collection	16
2.3.2. Sound stimuli selection and Jury Test 1	17
2.3.3. Jury Test 1 procedure	19
2.3.4. Psychoacoustic evaluation and discussion	21
2.4. Acoustic Jury Test 2.....	24

2.4.1.	Sound stimuli selection	26
2.4.2.	Jury Test 2 procedure and results	27
2.4.3.	BTL analysis	29
2.4.4.	Emotional state study	33
Chapter 3.	Theoretical formulation.....	39
3.1.	Overview and assumptions	39
3.2.	Two point sources	41
3.3.	HDD Stationary parts.....	46
3.4.	Rotating disk.....	55
3.5.	HSA	67
3.6.	Summary.....	77
Chapter 4.	Validation study	80
4.1.	Experimental measurement.....	80
4.1.1.	At far field (Receiver end)	81
4.1.2.	Near field measurements (source plane)	83
4.2.	Numerical solution of Vibro-acoustic Transfer Function	86
4.2.1.	Near field simulation.....	87
4.2.2.	Far field sound pressure prediction	102
4.2.3.	Far field psychoacoustic loudness prediction	104
4.3.	Result and discussion	104
4.3.1.	At the source.....	104
4.3.2.	At the receiver.....	106
Chapter 5.	Conclusions and Future Work.....	108
5.1.	Conclusions and contributions	108

5.2. Future work.....	110
5.3. Publications.....	112
Reference	113

List of Figures

Figure 1-1 An operational HDD on a table and in front of a sitting person	2
Figure 1-2 Sound event studied in this thesis	2
Figure 1-3 Typical 2.5" HDD interior.....	6
Figure 1-4 Sound field definition	8
Figure 1-5 A source plane lying in the x - y plane and an observer at far field.....	9
Figure 2-1 Questionnaire used in the social survey	14
Figure 2-2 Tolerable level in random sound, high pitch screeching sound and grinding sound from HDD.....	15
Figure 2-3 Schematic flow of the jury test approach	16
Figure 2-4 Measurement setup of HDD on ISO table for psychoacoustic assessment of HDD in anechoic chamber	16
Figure 2-5 Anechoic chamber background noise for 5 days	17
Figure 2-6 Spectrogram for sound #1 used in Jury Test 1 (time in x -axis, frequency in y -axis and color bar is sound pressure level).....	18
Figure 2-7 Spectrogram for Sound #2 used in Jury Test 1 (time in x -axis, frequency in y -axis and color bar is sound pressure level).....	18
Figure 2-8 Spectrogram for Sound #3 used in Jury Test 1 (time in x -axis, frequency in y -axis and color bar is sound pressure level).....	18
Figure 2-9 Spectrogram for Sound #4 used in Jury Test 1 (time in x -axis, frequency in y -axis and color bar is sound pressure level).....	19
Figure 2-10 A typical example of participant taking Jury Test 1 in the library (Left) and sound recording setup for playback system in acoustic chamber (Right)	20
Figure 2-11 Boxplot of the volume at which the majority of participants started to find each sound intolerable.....	20
Figure 2-12 Noise annoyance level vs SPL (in dBA) of HDD on both ears	22
Figure 2-13 Psychoacoustic parameters vs noise annoyance level on both ears	22

Figure 2-14 Questionnaire used in Jury Test 2	26
Figure 2-15 Participant taking Jury Test 2 and HEAD Acoustics equipment.....	28
Figure 2-16 Correlation between neural network predicted and actual BTL scale for young age group (left) and older group (right)	32
Figure 2-17 Emotional states of 34 participants on different HDD sound events.....	33
Figure 3-1 Near field calculating/measuring layer for 2.5" HDD	39
Figure 3-2 Green's first Identity	43
Figure 3-3 A schematic diagram of HDD internal with two point sources	45
Figure 3-4. The flow chart for the acoustic analysis on HDD stationary components	47
Figure 3-5 A type 2.5" HDD drive casing with an arbitrary point P	47
Figure 3-6 The spindle motor forces in a single tooth	52
Figure 3-7 The VCM used in a 2.5" HDD	53
Figure 3-8 Model Disk spindle system	55
Figure 3-9 Rotation transformation between XYZ and xyz.....	57
Figure 3-10 A typical example of HDD HSA.....	67
Figure 3-11 Reference frame for HDD HSA.....	68
Figure 4-1 Background noise of the anechoic chamber measured by B&K 4955 microphone.....	81
Figure 4-2 Far field sound measurement using binaural head (Left); sound measurement using microphone (Right)	82
Figure 4-3 Far field measurement setup.....	82
Figure 4-4 HDD far field FFT results: sound pressure in Pa ² (Left) and SPL in dB (Right)	83
Figure 4-5 Dimensions of microphone 4955.....	83
Figure 4-6 The design of the aluminum fixture	84
Figure 4-7 Setup of the near-field acoustic measurement.....	85
Figure 4-8 Results of 2.5" HDD acoustic measurement at near field	86
Figure 4-9 Flowchart of the psychoacoustic loudness computation for HDD random write/read via VaTF	86
Figure 4-10 Schematic of a 10-node tetrahedral acoustic element	87
Figure 4-11. ANSYS Maxwell for the 2.5" HDD spindle motor.....	89
Figure 4-12. ANSYS Maxwell for the 2.5" HDD VCM.....	89

Figure 4-13. ANSYS Transient Structural for 2.5" HDD component - Stationary parts	90
Figure 4-14. ANSYS Transient Structural for 2.5" HDD component - HSA	91
Figure 4-15. ANSYS Transient Structural for 2.5" HDD component - Rotating Disk.....	91
Figure 4-16 All the components used in simulation.....	92
Figure 4-17 A Schematic diagram of the FEM setup	93
Figure 4-18 Z-directional forces location for 2.5" HDD HSA	94
Figure 4-19 Z-directional forces location for 2.5" HDD Rotating Disk.....	95
Figure 4-20 Z-directional forces location for 2.5" HDD Stationary Parts	95
Figure 4-21 ANSYS Harmonic Response simulation for 2.5" HDD HSA	96
Figure 4-22 ANSYS Harmonic Response simulation for 2.5" HDD Rotating disk.....	96
Figure 4-23 ANSYS Harmonic Response simulation for 2.5" HDD Stationary Parts.....	97
Figure 4-24 ANSYS Harmonic Response simulation for 2.5" HDD Two Point Sources.....	97
Figure 4-25 Typical examples of Sound pressure at near field for difference 2.5" HDD HSA.....	98
Figure 4-26 Typical examples of Sound pressure at near field for difference 2.5" HDD Rotating disk.....	98
Figure 4-27 Typical examples of Sound pressure at near field for difference 2.5" HDD Stationary Parts.....	99
Figure 4-28 Typical examples of Sound pressure at near field for difference 2.5" HDD Two Point Sources	99
Figure 4-29 Identification of arbitrary weight function, A using curve fitting method	101
Figure 4-30. Microphone locations on top of the HDD measured.....	105
Figure 4-31 Linear correlation study between FEM results and Measured results at the far field	106

List of Tables

Table 2-1 Intolerable Volumes from Sound #1 to #4	21
Table 2-2 Correlation between Jury Test 1 results and psychoacoustic parameters	23
Table 2-3 P values between psychoacoustic metrics in Jury Test 1	23
Table 2-4 . Psychoacoustic parameters and SPL for sounds used in Jury Test 2.....	27
Table 2-5 Preference matrix of young age group.....	30
Table 2-6 Preference matrix of the old age group	30
Table 2-7 BTL scale and psychoacoustic metrics of each sound and their correlations in different age groups	31
Table 2-8 P-value for different age groups.....	32
Table 4-1 Magnetic properties used in simulation for motor force calculation	88
Table 4-2 HDD spindle forces at different frequencies in the z-direction.	90
Table 4-3 The force input used in the near field simulation	94
Table 4-4 the material properties of the component for the HDD simulation	88
Table 4-5 FEM calculated natural frequency with respect to its corresponding model shape	92
Table 4-6 FEM result for each component.....	Error! Bookmark not defined.
Table 4-7 FEM results component level and final results	102
Table 4-8 FEM near field velocity results	103
Table 4-9 Computed far field sound pressure level computation results base on velocity data	103
Table 4-10 FEM vs. measurement results	105
Table 4-11 Result comparison: far field measurement vs. FEM result	106

List of Abbreviations

HDD	Hard Disk Drive
FEM	Finite Element Method
VaTF	Vibro-aoustic Transfer Function
NAH	Near-field Acoustical Holography
SPL	Sound Pressure Level
VCM	Voice Coil motor
HSA	Head Stack Actuator

Chapter 1. Introduction

This thesis investigates the relationship between the psychoacoustic annoyance and the 2.5” Hard Disk Drive (HDD) structural vibration. The system studied is limited to the very small enclosure with a size of 100 mm (Length) × 70 mm (Width) × 7 mm (Thickness) and it only emits 25 dB noise.

The introduction provides the background, motivation and outline of this thesis.

1.1. Overview, motivation and background

This thesis is motivated by both industrial applications and academic challenges. The objective is to develop an effective method to reduce people’s uncomfortable feeling over any household and office noise caused by electrical and mechanical products. In this thesis, a 2.5” HDD noise has been studied. The author believes that the method and approach described in this thesis can be applied to the noises of other products that affect the wellbeing of individuals at home and in office. In this thesis, typical situations that may take place at home or in an office is studied (see Figure 1-1).

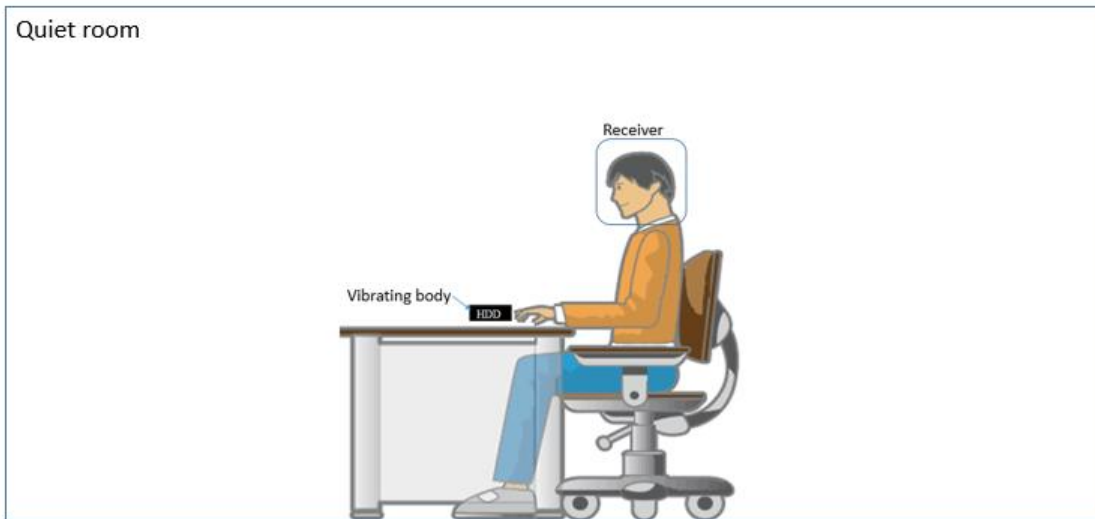


Figure 1-1 An operational HDD on a table and in front of a sitting person

Figure 1-1 shows a typical example of an office environment, with a person sitting in front of an office desk and an operational HDD resting on the desk in a large and quiet room. The room is large enough so that the sound will not reflect.

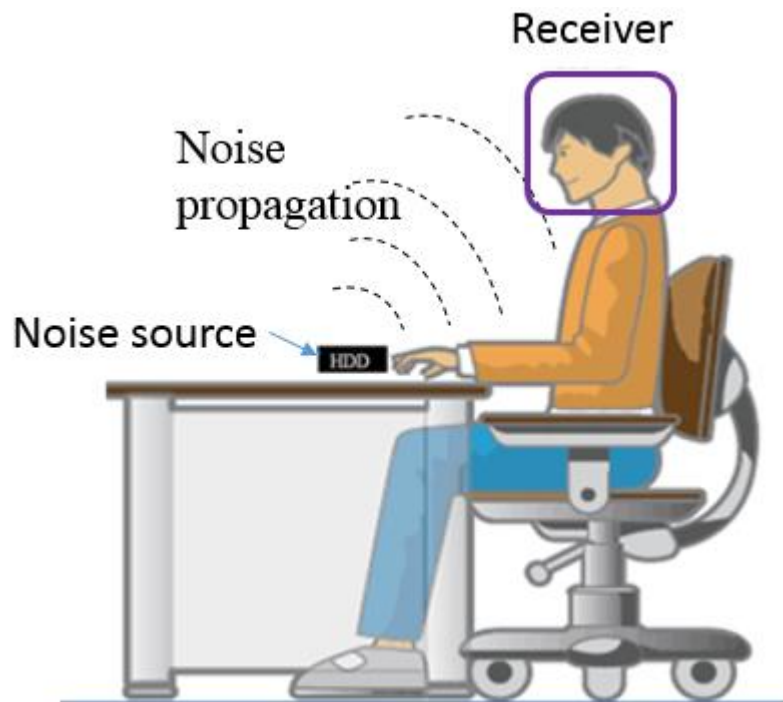


Figure 1-2 Sound event studied in this thesis

Figure 1-2 further illustrated the complete sound event studied in this thesis. When the HDD is operating, the HDD body vibrates, and oscillates the air near the vibrating body. The sound wave further radiates out, reaching the receiver at the far field. The energy of the sound wave can be dissipated in four ways: (1) being reflected back to the source; (2) reaching the human

perception system through the ears; (3) reaching the human perception system through channels on the human body other than the ears, and (4) being dissipated to the infinite space. Hence, a sound event should be studied for three regions, i.e., the receiver, the vibrating body and the near field, as well as the noise propagation from the near field to the far field.

1.1.1. The receiver response of the noise

Many researchers have done studies on how noise affects individuals. In 1980, Broadbent (Broadbent, 1980) pointed out that noise annoyance can affect people's mental health in his study. Since then, many researchers have conducted studies to understand the individual noise-annoyance. For example, Babisch et. al (Babisch et al., 2009) investigated aircraft noise annoyance. Novak (Novak and Refai-Ahmed, 2005, Novak et al., 2005) inspected PC CPU cooling fan and graphical card noise. Some researchers (Ng and Koh, 2008b, Rohrmeier et al., 2012, Rohrmeier et al., 2015) studied snoring noise. Most recently, among many others (Schäffer et al., 2016, Kane and Andhare, 2016, Egab and Wang, 2016, Yang et al., 2015, Schell-Majoor et al., 2015, Di et al., 2015, Wang et al., 2014, Torija and Flindell, 2014, Peris et al., 2014), Gauthier (Gauthier et al., 2017) studied consumer electronics.

Recently, the human annoyance caused by small interior devices such as HDD (Ma et al., 2016, Ma et al., 2015) was studied. Several psychoacoustic metrics such as sharpness, roughness, loudness and fluctuation strength were correlated with subjective judgements through a social survey on selected participants of different age groups.

Loudness (Fastl and Zwicker, 2007) is the sensation value of the human perception of sound volume. The unit of loudness is "sone". By definition, a sine tone of the frequency of 1 kHz with a level of 40 dB has a loudness of 1 sone. The determination of loudness of stationary signals has been specified in the DIN 45631 (DIN45631, 1990, DIN45631/A1, 2008), ISO 532B (ISO532B, 1975) and ANSI S3.4 (ANSI-S3.4, 2007) standards. A large sound intensity value results in a "loud" sound. The loudness may also be a measure of the total activity of the basilar membrane. ISO 532 Section B provides a standard graphical method for loudness

computation. A computer program developed based on this method is attached under DIN 45631. In this thesis, this computer program was used for the loudness computation.

Sharpness (Fastl and Zwicker, 2007) is a sensation value caused by high frequency components in a given noise. The unit of sharpness is “acum”. Sharpness (Ng and Koh, 2008a) of 1 acum is due to a narrow-band noise at 1 kHz with a bandwidth less than 150 Hz at a level of 60 dB. A higher sharpness value shows greater energy in higher frequencies. It relies on the weighted centroid of the specific loudness content, as shown below.

$$S = 0.11 \frac{\int_0^{24Bark} N' g(z) z dz}{\int_0^{24Bark} N' dz} \quad (1)$$

where S denotes the sharpness in acum, and g(z) denotes the weighing function of the critical band rate z. Higher sharpness value indicates greater energy in high frequencies.

Roughness (Fastl and Zwicker, 2007) is a sensation (Ng and Koh, 2008a) that arises from rapid temporal variations of sounds caused by beats between tones in a critical band. The unit of roughness is “asper”. Using the boundary criterion (Ng and Koh, 2008a), a 1 kHz tone at 60 dB with 100% amplitude modulation at 70 Hz generates the roughness of 1 asper. With increasing roughness, noise emissions are perceived as increasingly noticeable and can be quite aggressive and annoying even when the loudness and SPL remain unchanged. Roughness increases with increasing modulation depth of the temporal masking pattern of sounds (Aures, 1985).

$$R = 0.3 \frac{f_{mod}}{kHz} \int_0^{24Bark} \frac{\Delta L_E(z) dz}{dB/Bark} \quad (2)$$

where f_{mod} signifies the modulation frequency, and ΔL_E signifies the range of excitation level within an auditory filter. Roughness increases with increasing modulation depth of the temporal masking pattern of sounds.

Fluctuation strength (Fastl and Zwicker, 2007) shows human sensitivity (Ng and Koh, 2008a) towards slow moving amplitude modulation for sounds with frequency modulated at approximately 4 Hz. The unit of fluctuation strength (Ng and Koh, 2008a) is vacil, referenced

to a 1 kHz tone at 60 dB with 100% amplitude modulation at 4 Hz. Fluctuation strength is associated to a fluent speech at a speaking rate of 4 syllables/s, since its amplitude modulation is concentrated around 4 Hz. The fluctuation strength of a sound can be expressed as

$$F = \frac{0.008 \int_0^{24Bark} (\Delta L / dB Bark) dz}{(f_{mod} / 4Hz) + (4Hz / f_{mod})} \quad (3)$$

where ΔL is the masking depth (i.e., the difference between the maxima and the minima in the temporal masking pattern).

1.1.2. Vibrating body and near field

As the overall size of a 2.5" HDD is small, the small enclosure approach has been adopted. There are many studies performed on modeling of small enclosures (Lyon, 1963, Li et al., 2007, Ruber et al., 2015, D. J. Oldham, 1991, Panza, 2014, Tang, 2007, Gao et al., 2003). In 1963, Lyon (Lyon, 1963) studied noise reduction of small rigid boxes with only one flexible wall at very low frequencies. Li and his team (Li et al., 2007) worked on the modeling for T-shaped resonators. Ruber (Ruber et al., 2015) studied the sound transmission loss of a small enclosure. Oldham and Hillarry (D. J. Oldham, 1991) developed the theoretical models of small close fitting enclosures. The model was able to predict both low and high frequencies of sound fields across the non-uniform panel. Michael (Panza, 2014) formulated a very special acoustic image model for sound field inside small close fitting enclosures. Tang (Tang, 2007) measured the vibroacoustic performance of a honeycomb structure for close fitting enclosures.

For the past half-century, the Hard Disk Drive (HDD) has become a major storage device for digital information and data (Tandon et al., 2006). It is widely used in many applications such as home entertainment system, gaming consoles and personal laptops.

Figure 1-3 shows a typical example of 2.5" HDD and its interior components. A 2.5" HDD mainly consists of the magnetic disk and spindle motor, a voice coil motor (VCM), a head stack actuator (HSA), a baseplate and a cover (Wood, 2009). In the spindle motor, there is a fluid dynamic bearing, which allows the disk to rotate at high speed. For HSA to move in radial range across the disk, there are two ball bearings at the pivot location.

During operation, the magnetic disk rotates at a constant speed anti-clockwise while the HSA swings radially across the disk. With the combination of constant disk spinning and HSA swinging, the magnetic head at the tip of the HSA reads and/or writes data on the magnetic disk. At the same time, these movements also generate vibration and noise. In this consideration, HDD noise is mainly caused by force-excited mechanical vibration of the HDD structure (Wang et al., 2010). The main source of mechanical vibration is the forces generated by the VCM motor and the spindle motor. (Gao et al., 2003). Most of these acoustical studies were conducted on a relative small enclosure, however, a typical 2.5" HDD has only 15 cm³ volume of air and is much smaller than any enclosure that has been studied so far. Moreover, both acoustical and vibration transmissions (Gao et al., 2003) are present inside an HDD.



Figure 1-3 Typical 2.5" HDD interior

Over the years, many academic studies and industrial effort have been made to reduce the HDD noise level. However, those works was mainly targeted to reduce the sound pressure level (SPL) or sound power level (Choi et al., 2004). Nowadays the sound power level of 2.5" HDD has been reduced to less than 30 dB(A) for most 2.5" HDDs in the market, however,

there are still complaints about the HDD noise. Because of this, sound power level or SPL is not good enough to address the annoyance level (Guidati, 2008, Fastl, 2010).

An HDD vibrating body causes near field sound fluctuation. Understanding such near field sound fluctuation will help to locate and reduce noise at the noise source (Wang and Crocker, 1983). For noise source identification, the important factors are the frequency, the amplitude and the location. Over many years of study, techniques and methods have been developed, including the lattice Boltzmann method (Vergnault et al., 2013), the field programmable gate array (Veggeberg and Zheng, 2009), the beam-forming algorithm (Suzuki, 2006) and the near-field acoustic holography (NAH) method. Among these methods, NAH, initially developed by Williams and Maynard et al. (Williams and Maynard, 1980), was the most commonly used, as it gives the most promising sound field reconstruction from the vibrating body. The method used a microphone array or probes placed close to the structure to reconstruct the spatial acoustic field at one frequency or in a frequency range (Maynard et al., 1985, Veronesi and Maynard, 1987, Williams, 1999). As a result, it could identify the dominant modes in the noise source that caused vibrations within the structure (Prezelj et al., 2013).

Since NAH was proposed (Williams and Maynard, 1980), many methods have been developed base on their underlying theory (Wu et al., 2016):

- Statistically optimal NAH (SONAH) (Steiner and Hald, 2000, Cho et al., 2005, Hald, 2009) calculated the varies acoustic quantities such as sound power, acoustic pressure and velocity on the measuring plane using the transfer matrix that is defined with optimal average accuracy for all the propagating waves. Weighted evanescent waves are projected (Hald, 2009).
- Boundary Element Method (BEM) based NAH (KIM and LEE, 1990, Bai, 1992, Veronesi and Maynard, 1989, Zhang et al., 2000, Schuhmacher et al., 2003) used integral equations to generate the transformer matrix between measured layer and source layer for the arbitrarily shaped model. Depending on the integral equations used, there were two types of BEM based NAH, namely, direct (Helmholz integral equation) (KIM and LEE, 1990, Bai, 1992, Veronesi and Maynard, 1989) and indirect formulation (single or double layer of integral equation) (Zhang et al., 2000).

- The Method of Wave Superposition (MWS) was proposed by Kopman in 1989 (Koopmann et al., 1989). MWS used the principle of wave superposition to reproduce the surface velocity of the radiator to compute the surface pressure of the source strength (Koopmann et al., 1989, Sarkissian, 2005, Song et al., 1991, Zhang et al., 2012).
- Helmholtz equation least-squares method (HELs) (Wu, 2000, Wang and Wu, 1997) was developed from spherical wave expansion theory to obtain the acoustic pressure field of a vibrating body.

NAH can be used to reconstruct sound field with pressure, fluid velocity and intensity vectors near the source (Williams, 1999). With Fourier tools such as Rayleigh's integrals, far field sound radiation can be calculated.

1.1.3. Noise propagation

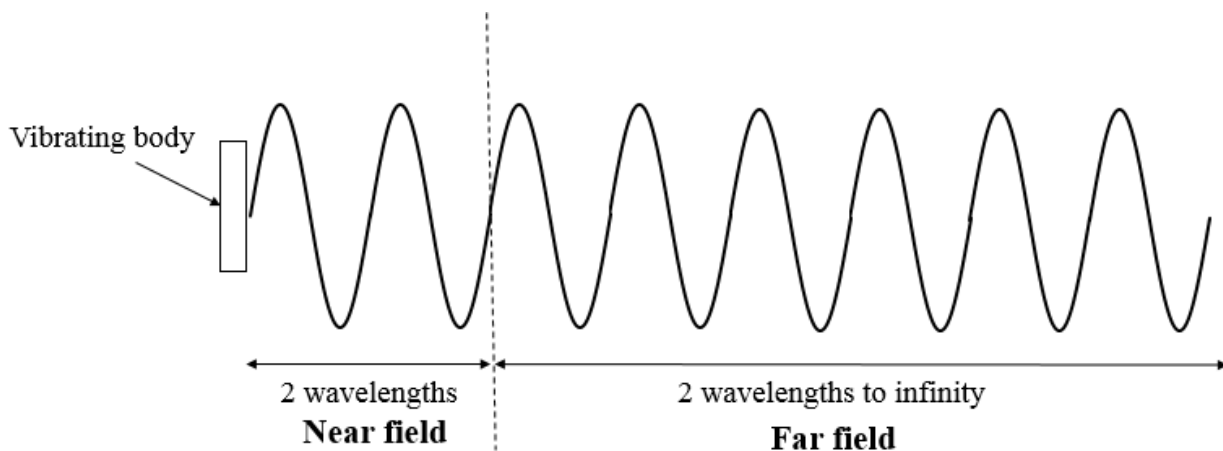


Figure 1-4 Sound field definition

Noise propagates from a vibrating body to the near field, and then radiates out to the infinite distance under free field condition where there is no sound reflection. The sound field can be divided into two regions, i.e., the near field and the far field. By definition, near field means the distance to the vibrating body is within two wavelengths, and the sound pressure and sound velocity are out of phase; far field means the distance is beyond two wavelengths, and the sound pressure and velocity are in phase (IEC60050, 1994).

In the previous section, NAH was used to address the sound quantities in the near field. This section will discuss more on the sound radiation at the far field. Sound radiation has been studied by many researchers. In 1962, Maidanik first proposed a method to compute sound radiation from a vibrating rectangular plate (Maidanik, 1962). Ten years later, sound radiation efficiency was further studied using Rayleigh's integral for each vibration mode (Wallace, 1972). Lately, Williams and Maynard conducted a numerical evaluation on a planar radiator using Rayleigh's integral, and fast Fourier transfer was used to compute the specific velocity in the frequency domain (Williams and Maynard, 1982). Rayleigh's integral (Rayleigh, 1896) states

$$p(x, y, z) = \frac{j\rho ck}{2\pi} \int_S v_p(x, y) \frac{e^{-jkR}}{R} dS \quad (4)$$

where ρ is the air density, c is the air speed, k is the wavenumber, $v_p(x, y)$ is the normal specific velocity to the source plane, and R is the distance between the source point and the observer.

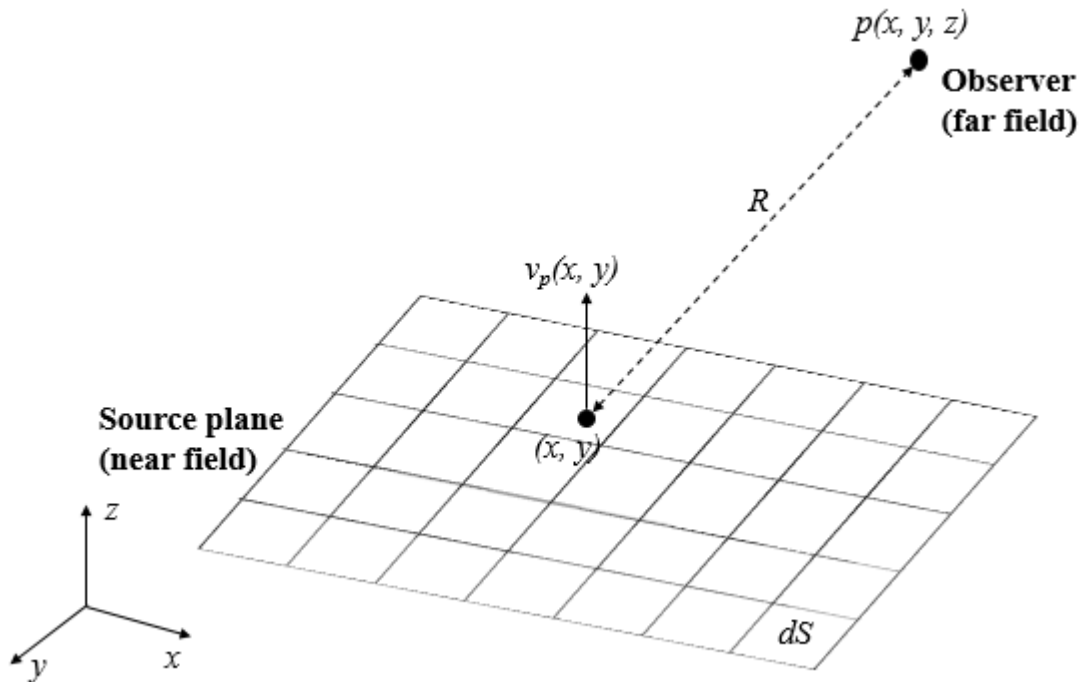


Figure 1-5 A source plane lying in the x-y plane and an observer at far field

1.2. Challenges and outline of the thesis

There are two main challenges in this thesis. First, the HDD studied is small in dimension i.e. 100 mm (Length) \times 70 mm (width) \times 7 mm (thickness). The parts in such a small enclosure are all flexible. Second, the HDD used in this study is already very quiet. The average noise level is less than 23 dB(A). Precise measuring instrument and very quiet facility are required in order to obtain accurate measurements.

This thesis develops the method to correlate human uncomfortable feeling to 2.5" HDD vibration. It reports a psychoacoustic study on 2.5" HDD (Chapter 2) and analyzes the HDD noise source base on both theoretical and experimental results (Chapters 3 and 4).

Chapter 2 presents the step-by-step approach to quantify and predict the noise annoyance of 2.5" HDD with known parameters. Base on Fastl's book (Fastl and Zwicker, 2007), psychoacoustic metrics can be used to quantify the noise annoyance. This chapter studies it in detail and proposes a model to predict the noise annoyance of the 2.5" HDD.

Chapter 3 shows the derivation of the vibro-acoustic transfer function (VaTF) for the HDD. The mathematical formulation is developed from the principle of wave superposition (Zhang et al., 2012, Wang et al., 2012, Junyi et al., 2016, Junyi and Balint, 2015). The new VaTF includes all the HDD major components, i.e. HSA, VCM, rotating disk, HDD housing and rubbing noises due to the bearing system.

In Chapter 4, the pressure results at the near field is measured using microphone array. The numerical solution is computed based on the formulation in Chapter 3 using the finite element method (FEM). The measured result and the numerical solution are compared. Finally, Chapter 5 concludes the thesis and provides suggestions for the future work.

Chapter 2. HDD noise annoyance study

This chapter provides the detail psychoacoustic study on the 2.5" HDD noise. Part of following section 2.1, 2.2, 2.3 and 2.4 used the materials from the following paper published during the PhD.

MA, Y. C., CHIN, C. S., WOO, W. L. & GAO, B. 2016. An Acoustic Annoyance Study of Hard Disk Drive for Laptop. *IEEE Transactions on Magnetics*, 52, 1-9.

MA, Y. C., CHIN, C. S. & WOO, W. L. 2015. Neural Networks-Based Acoustic Annoyance Model for Laptop Hard Disk Drive. *International Journal of Electrical, Computer, Energetic, Electronic and Communication Engineering*, 9.

2.1. Introduction

In the early 20th century, people started to understand the noise annoyance impacts (Nasmyth, 1929). It is recognized that noise annoyance or feeling of being bothered by one particular source of noise can lead to undesired responses (Basner et al., 2014) such as displeasure, symptoms, anger, and stress-related exhaustion. The rapid growth of Internet of Things (IoT), digital media and 3D movies has increased the storage capacity and usage of laptops. The noises generated from laptop HDD are usually low and was hardly noticed in most urban environment during normal daytime activities. However, such noises have become one of the important factors affecting the users' well-being as sounds otherwise masked can be clearly heard and prove distracting to sleep comfort especially for elderly who sleep more lightly while the laptop is still operating in the room during wee hours when most people are already asleep (Tandon et al., 2006, Choi et al., 2004, Dang-Vu et al., 2010). Additional noise can influence just noticeable sound changes at around 20 to 30dB above masked threshold in quiet environment. Recent study has shown a SPL of 33 dB(A) (Basner et al., 2014) can cause physiological effects during sleep for shift-workers, children, elderly and people with sleep disorder because such noises induced sleep disturbance (Muzet, 2007, Basner et al., 2006) and resulted in rapid eye movement sleep, early awakenings, delayed sleep onset and increased time spent awakened. World Health Organization (WHO) reported

the Night Noise Guidelines for different average night noise levels for Europe ((WHO) and Copenhagen, 2009). It indicates that 30–40 dB(A) causes some sleep disturbance, 40–55 dB(A) adversely affects the health of individuals and above 55 dB(A) causes sizable population to have serious sleep-disturbance, annoyance and increase in cardiovascular diseases.

With aging populations in modern industry, many frequent users of consumer products may have slight to moderate hearing loss (Shepherd, 1975). There is also an increase number of the younger generation showing hearing deficits due to extremely loud leisure activities. Besides loudness, the annoyance reaction also depends on the type of noise exposure. Psychoacoustics covers a spectrum of human reactions to noise and includes mainly the study of loudness, roughness, sharpness and fluctuation strength (Shepherd, 1975, Fastl and Zwicker, 2007). The common practice is to study how human feels about the sound in a system using data collection methods such as survey and listening test (also called jury test) (Pierrette et al., 2012, Lyon, 2000b, Lyon, 2000a). The location to conduct the jury test is critical, because certain sound is only noticeable in a specific (e.g. quiet) environment. For example, an experiment has been conducted on how people's emotions change with the sound they heard (Asutay et al., 2012). A test was done on 40 participants (fifteen females) from 22 to 44 years old in a classroom. A fixed scaling method was used in the experiment for measuring the current arousal level, the sound sample annoyance level and the loudness level. Participants ranked the sounds they heard according to their feelings.

A few researchers demonstrated the derivation of a model of annoyance through conducting a jury test on 50 students of the age between 19 and 31 (Ellermeiera et al., 2004). Forty sounds were tested during the experiment. The sounds were recorded by a single (mono) microphone. The psychoacoustical metrics were formed and the modelling of the overall annoyance was derived.

After the first jury test, a second improved test was conducted. This jury test was performed in a semi-anechoic chamber using sounds generated from eight different HDDs (Choi et al., 2004). Each of the 56 jury members was required to hear 28 pairs of HDD noises in about half an hour and compare the loudness and annoyance levels between the two noises grouped in each pair. A new Preference Index was developed on how to measure HDD noise

annoyance, but the results could be inaccurate because the jury members were required to listen to many sounds in a relatively short period of time. Fatigue might affect the jury members' judgment as the test was conducted in a semi-anechoic chamber, which is an isolated and quiet environment.

Some researchers had also proposed a standard set of survey questions on long-term annoyance of people at home (Fields et al., 2001), however, the survey developed showed that the acoustical factors could not correlate well with the subjective ratings on annoyance level and the objective measurements using just SPL (Basner et al., 2014) and loudness. This suggests that other non-acoustic factors may affect human judgment. A team had conducted in-depth studies on the relation between subjective human ratings and psychoacoustical metrics associated with large-interior noise (Öhrström et al., 2006). However, the participants of relatively narrow age gaps and applications had limited the usefulness of their findings.

The understanding of noise annoyance on different age groups and its impact on design for acoustic ergonomics are still not complete. In addition, study needs to be conducted on the user's emotional perceptions caused by different sound events in HDD's operation. There are a few studies that concentrated on the impact of the acoustical space on emotional perceptions to sound (Bradley, 1999, Knudsen, 1932) but the extent of the impacts to the emotional responses by different sound events on HDD has not been explored.

2.2. Social survey of HDD noise

Social survey is a common method used to find out how people are annoyed by particular machinery and transportation noise sources (Fields et al., 2001), for example, aircraft (Kroesen et al., 2013), wind turbine (Schäffer et al., 2016), traffic noise (Elmenhorst et al., 2014), railways (Peris et al., 2014) and industrial applications (Pierrette et al., 2012). In this thesis, a similar method has been used on HDD, which has a lower noise level as compared to the noise mentioned above. A questionnaire (Figure 2-1) was developed by taking reference from ISO 15666 (ISO/TS15666, 2003). The aim of this questionnaire is to find out how noticeable the noise from HDD is and the daily time spent by each participant on using their

laptops. The types of noise surveyed on are continuous clicking sound, random sound, high pitch screeching sound and grinding sound.

PLEASE CIRCLE THE APPROPRIATE OPTION

Age: 10-19 20-29 30-39 40-49 50-59 others

Gender: Male Female

- 1) Have you noticed the hard disk making noise while using a laptop?
Yes No

- 2) If Yes, please select from below noises and rank them in 1 to 5
(1 is intolerable & 5 is tolerable)
 - A. Continuous clicking sound
Noise Rank: 1 2 3 4 5
 - B. Radom sound
Noise Rank: 1 2 3 4 5
 - C. High pitch screeching sound
Noise Rank: 1 2 3 4 5
 - D. Grinding sound
Noise Rank: 1 2 3 4 5

- 3) How long do you normally spend on the laptop
 - A. Less than 2 hours
 - B. 2 to 3 hours
 - C. 3 to 5 hours
 - D. 5 to 8 hours
 - E. More than 8 hours

Figure 2-1 Questionnaire used in the social survey

A total of 160 people aged between 10 and 59 took part in the survey. They were randomly engaged at shopping complexes and train stations where participants were easily found. Figure 2-2 shows the survey results, which indicates that most participants felt moderately-to-highly intolerable when random sound, high pitch screeching sound and grinding sound were heard from their laptops. Moreover, the result shows that participants younger than 30 years old are less tolerable to random sound and high pitch sound, whilst participants aged

between 30 and 39 are less tolerable to the random sound and grinding sound (approximately 6 kHz to 10 kHz). On the other hand, participants older than 40 are more acceptable to the noises from HDD in general.

The above result indicates that age is an important factor to consider when evaluating the HDD noise annoyance and conducting the psychoacoustic parameters measurement. To further quantify human feeling using numerical parameters, two acoustic jury tests were conducted.

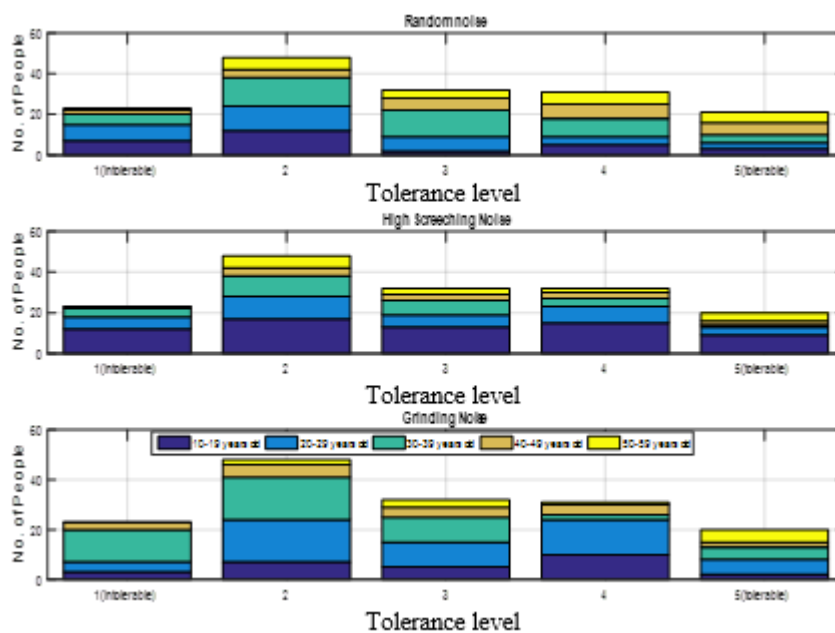


Figure 2-2 Tolerable level in random sound, high pitch screeching sound and grinding sound from HDD

2.3. Acoustic Jury Test 1

Figure 2-3 shows the schematic flow chart of the jury test. A set of HDD noises were first recorded and processed in the auditory model and the various psychoacoustic metrics (PM) were computed. The same noise signals were then played to the jury test participants. The participants were asked to rank the annoyance level based on their perceptions, which was regarded as the subjective rating (SR). Finally, the relationship between the subjective rating and the psychoacoustic metrics were determined.

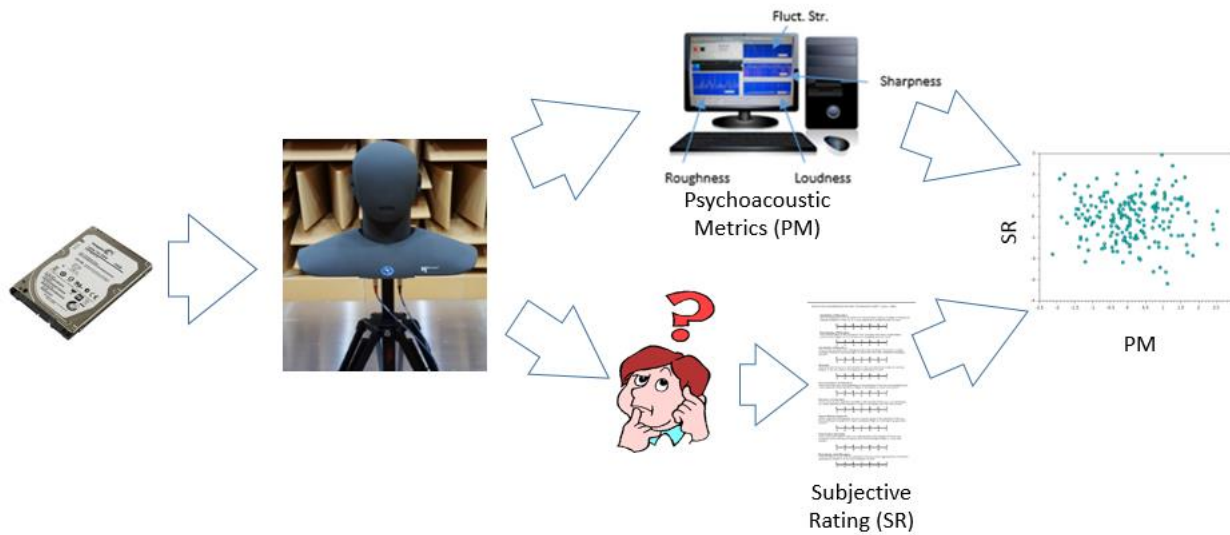


Figure 2-3 Schematic flow of the jury test approach

2.3.1. Setup for sound sample collection

The setup of sound sample collection was designed to simulate the situation in an office working environment (Figure 2-4). A HEAD Acoustics™ binaural head was used and replaced the sitting user as shown in the left and middle panels of Figure 2-4. An operational HDD was placed on the ISO table, which is mentioned in ISO 7779 (ISO7779, 2010) Annex A as a standard testing table. To ensure the consistency in testing condition, a standard setup (shown in Figure 2-4 right panel) was developed based on ISO 7779 (ISO7779, 2010).

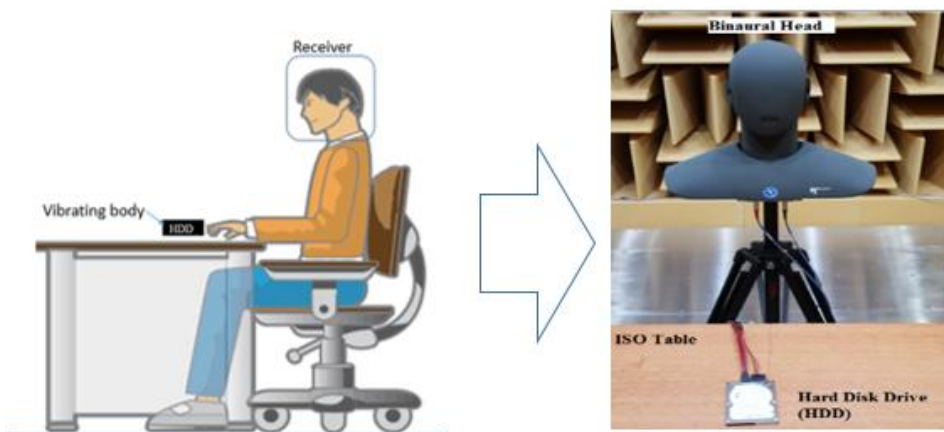


Figure 2-4 Measurement setup of HDD on ISO table for psychoacoustic assessment of HDD in anechoic chamber

The measurement condition of the sound sample collection was strictly carried out throughout the process. The temperature of acoustic anechoic chamber was maintained at $23\pm 2^{\circ}\text{C}$, the humidity level at $50\pm 5\%$, and the atmospheric pressure at 1 atmospheric pressure. The plots of background noise data collected over five days show a good overlap as in Figure 2-5, indicating no significant variation in the background noise inside the chamber.

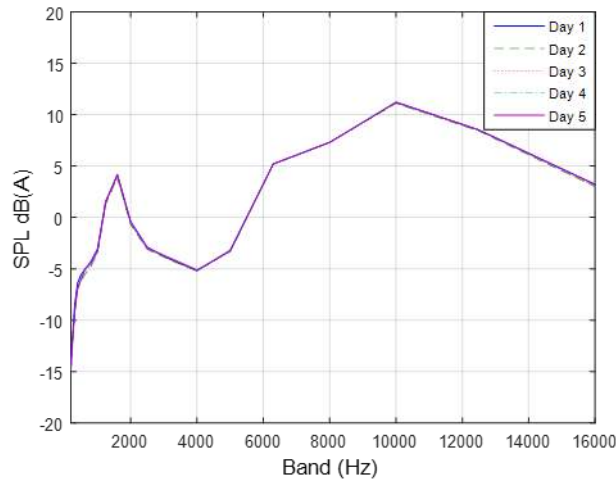


Figure 2-5 Anechoic chamber background noise for 5 days

2.3.2. Sound stimuli selection and Jury Test 1

A total of 100 HDD noises were recorded using the above setup. The following four sounds were selected based on the social survey results (section 2.2):

1. Random sounds generated by the HDD when it encounters some random events during normal operations, such as Sound #1, which was recorded when there was a sudden power loss. Two ‘click’ sounds occurred at 1.2 seconds and 2.5 seconds respectively, as shown in Figure 2-6, and the second ‘click’ sound was louder than the former. Such sounds could be quite annoying.
2. High pitch screeching sounds such as the sound generated by a faulty spindle motor, which resembles Sound #2. It exhibits a screeching sound at approximately 3000 Hz (Figure 2-7).
3. Grinding sounds that are generated during HDD operation. Sound #3 (Figure 2-8) is a sound recorded when HDD was performing writing and reading operation, while Sound #4 (Figure 2-9) is a sound when HDD was on random seek.

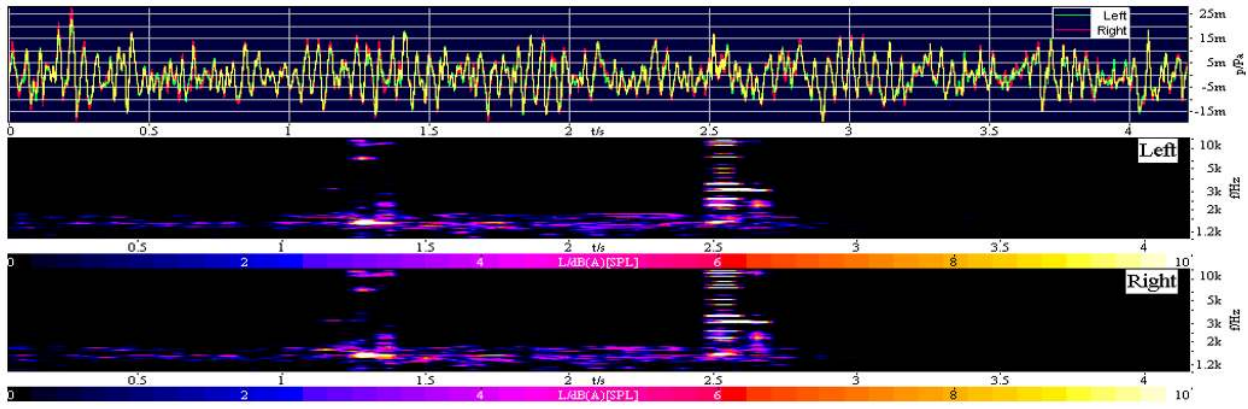


Figure 2-6 Spectrogram for sound #1 used in Jury Test 1 (time in x-axis, frequency in y-axis and color bar is sound pressure level)

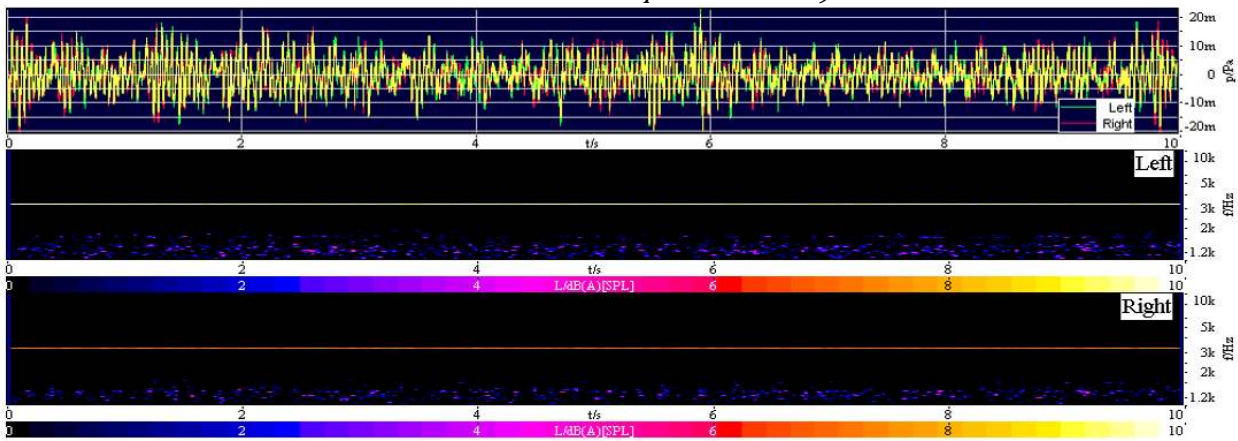


Figure 2-7 Spectrogram for Sound #2 used in Jury Test 1 (time in x-axis, frequency in y-axis and color bar is sound pressure level)

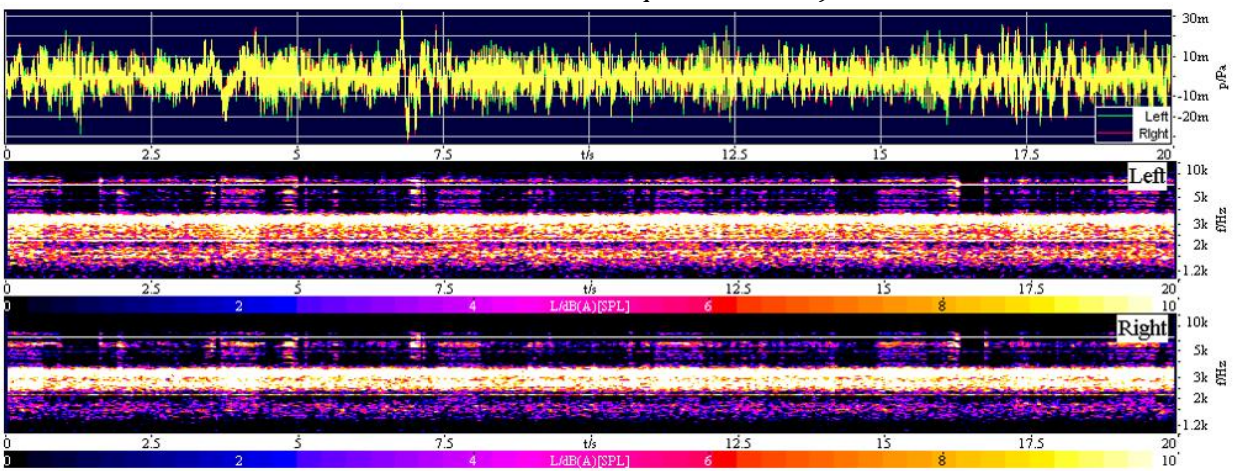


Figure 2-8 Spectrogram for Sound #3 used in Jury Test 1 (time in x-axis, frequency in y-axis and color bar is sound pressure level)

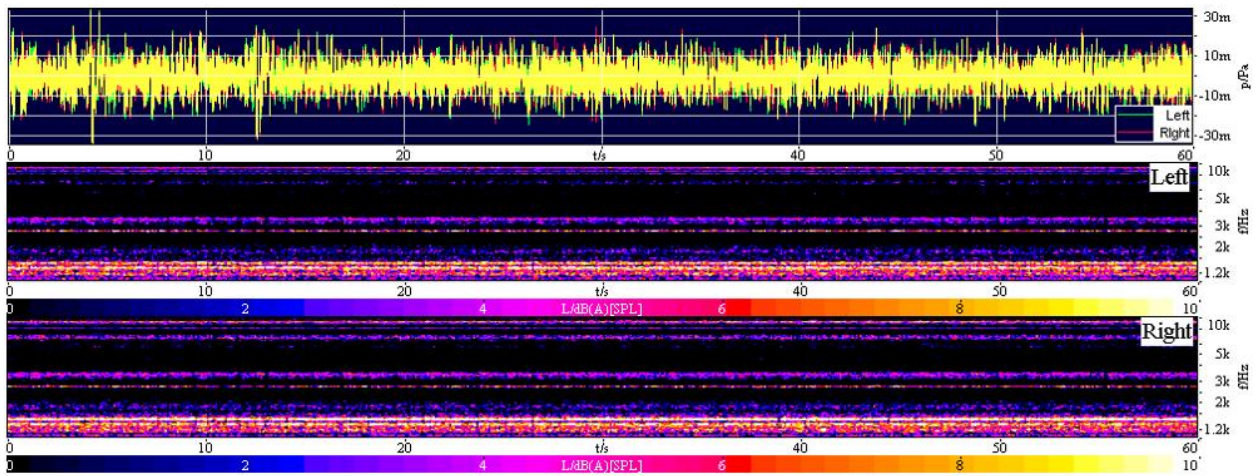


Figure 2-9 Spectrogram for Sound #4 used in Jury Test 1 (time in x-axis, frequency in y-axis and color bar is sound pressure level)

2.3.3. Jury Test 1 procedure

The four sound recordings (Sounds #1 to #4) were exported into MP3 format and downloaded to the playback system, which is equipped with a smartphone and earphones (Samsung HS330 Wi Headset with Inline Mic). A smartphone and earphones were used in this test due to their convenience and portability. The sound volume of the smartphone was initially tuned to 0 (silent), and is adjustable from 0 to 10 (the maximum volume).

Jury Test 1 was conducted in the library during the evening time. The time chosen was a quiet time during the day without many people around, hence the background noise is considered minimal. All the participants were instructed to increase the smartphone volume to the level at which he/she could just hear the sound, and then rate the sound from 1 (most acceptable) to 10 (most intolerable). After the first rating, he/she needed to further increase the volume to the maximum or to the level at which he/she felt absolutely intolerable, whichever is lower, and rate it again. A total of 139 people (including males and females) from age 21 to 25 participated in the test. Most of them were university students. A typical example of how the jury test was done is shown in Figure 2-10 (Left).



Figure 2-10 A typical example of participant taking Jury Test 1 in the library (Left) and sound recording setup for playback system in acoustic chamber (Right)

Figure 2-11 plots the volumes at which the participants felt intolerable for each sound. The overall annoyance was found from high to low as: Sound #3, Sound #4, Sound#1 and lastly Sound #2. This trend is further shown in Table 2-1: comparing to sounds generated during random stops and seeking operations (Sounds #1 and #4 respectively), sounds generated during HDD reading and writing operations (Sound #3) was more annoying even at moderated volumes (volumes 5 to 8). On the other hand, the idling operation (Sound #2) is more tolerable as it was regarded less annoying at its maximum volume (mean annoyance level is around 5 at volume 10).

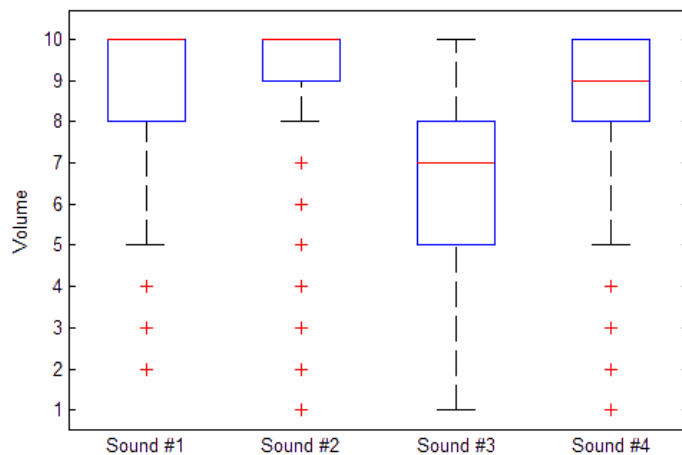


Figure 2-11 Boxplot of the volume at which the majority of participants started to find each sound intolerable

Table 2-1 Intolerable Volumes from Sound #1 to #4

Sound Types	Volume	Mean Annoyance	Ranking
Sound #1 (continuous-stop operation)	8	7.62	3
	9	6.50	
	10	5.97	
Sound #2 (Idle operation)	9	7.67	4
	10	4.98	
Sound #3 (write and read operation)	5	9.50	1
	6	9.27	
	7	9.63	
	8	9.58	
Sound # 4 (files seeking operation)	8	8.59	2
	9	8.52	
	10	7.16	

Because analysing the MP3 format sounds directly might have issues of inconsistent sound level, for the subsequent psychoacoustic evaluation the sounds used were recorded again in the anechoic chamber with the same playback system played into the Head Acoustic™ binaural head (Figure 2-10 (Right)). During the recording, the same smartphone used in the Jury Test 1 was placed on the table and the same earphones were put on the binaural head. The four sounds were successively played at each volume level and were recorded into the binaural head.

2.3.4. Psychoacoustic evaluation and discussion

It is commonly believed that a high SPL has the direct correlation with high annoyance level (Mats, 2007). However, this is not obvious from the result of Jury Test 1 as the correlation (R^2) was only 0.59 and 0.64 for the left and the right ears, respectively (Figure 2-12). A lack of strong correlation between SPL and the annoyance level requires a more in-depth analysis of the psychoacoustic parameters of the HDD besides SPL, such as loudness, sharpness, roughness and fluctuation strength.

In Figure 2-13, a good correlation was found in loudness (highest R^2 for 2nd order correlation) and roughness (highest 1st order correlation). Sharpness (due to the high frequency content) and fluctuation strength (of speed fluctuation) do not seem to show much correlation.

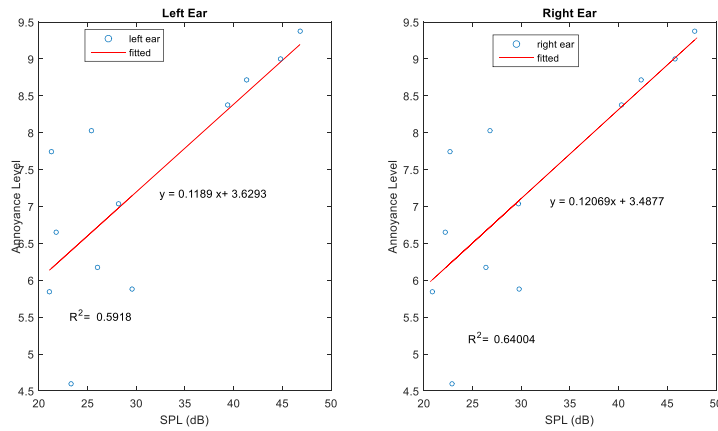


Figure 2-12 Noise annoyance level vs SPL (in dBA) of HDD on both ears

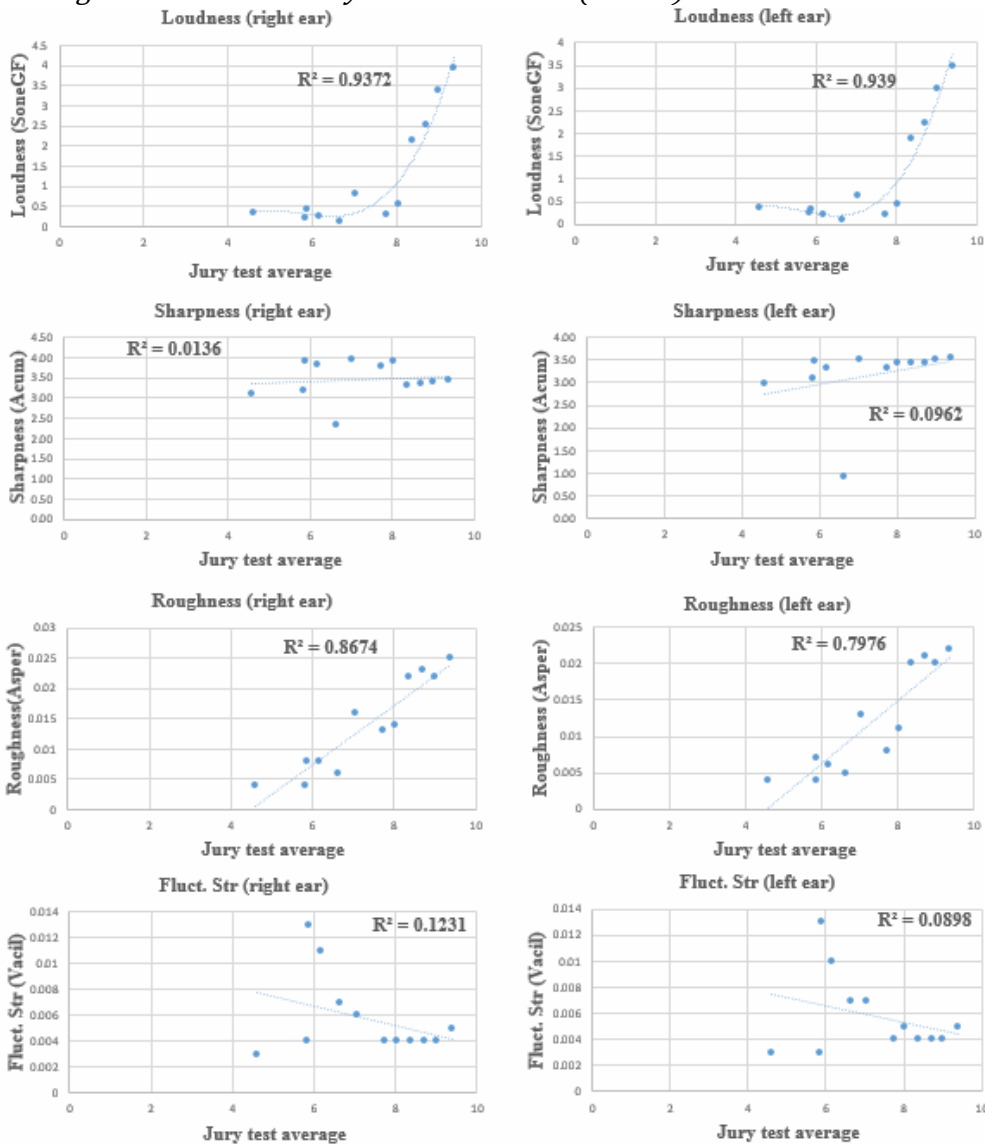


Figure 2-13 Psychoacoustic parameters vs noise annoyance level on both ears

A multiple regression analysis was performed to model the HDD noise annoyance using linear relationship. Table 2-2 summarizes the P values for the fitting between annoyance

level and the psychoacoustic metrics as well as SPL. P value for roughness was less than 0.05, verifying the more significant correlation between it and the noise annoyance level.

Table 2-2 Correlation between Jury Test 1 results and psychoacoustic parameters

		Jury Test 1			SPL	Loudness	Sharpness	Roughness	Fluctuation
		Q1	Median	Q3	[dBA]	[sone]	[acum]	[asper]	Strength
		[vacil]							
Sound #1	vol 8	5.5	7	8	22.2	0.15	2.34	0.006	0.007
	vol 9	6	6	7	26.4	0.28	3.85	0.008	0.011
	vol 10	4	6	7	29.8	0.44	3.91	0.008	0.013
Sound #2	vol 8	3	7	8	21.1	0.25	3.21	0.004	0.004
	vol 9	3	5	6	23.3	0.36	3.12	0.004	0.003
Sound #3	vol 5	7	9	10	40.3	2.14	3.42	0.022	0.004
	vol 6	7.75	10	10	42.3	2.52	3.45	0.023	0.004
	vol 7	9	10	10	45.8	3.38	3.5	0.022	0.004
	vol 8	10	10	10	47.8	3.92	3.53	0.025	0.005
Sound #4	vol 8	6.5	9	10	22.7	0.31	3.81	0.013	0.004
	vol 9	7.75	9	10	26.8	0.56	3.91	0.014	0.005
	vol 10	6	8	9	29.7	0.8	3.98	0.016	0.007
Correlation coefficient (Q1)					0.79	0.80	0.23	0.89	-0.23
Correlation coefficient (Median)					0.72	0.75	0.19	0.89	-0.48
Correlation coefficient (Q3)					0.59	0.62	0.22	0.83	-0.48

Table 2-3 P values between psychoacoustic metrics in Jury Test 1

	P-value		
	Q1	Median	Q3
SPL (dBA)	0.099	0.112	0.105
Loudness (Sone)	0.100	0.235	0.403
Sharpness (Acum)	0.853	0.736	0.714
Roughness (Asper)	0.019	0.008	0.005
Fluctuation Strength (Vacil)	0.133	0.766	0.819

Hence, equation (4) was formulated to predict the noise annoyance level using roughness.

$$NA_{(HDD)} = \alpha R + \beta \quad (5)$$

where $NA_{(HDD)}$ denotes HDD noise annoyance level in Jury Test 1, R is the Roughness, α and β are arbitrary constants having the following values: $245.99 > \alpha > 158.52$ and $2.66 < \beta < 6.57$. Although the preliminary findings in Jury Test 1 revealed that there is a relationship between the participants' annoyance level and the psychoacoustic parameters, more refinement is

required for drawing further conclusions. Many researchers have reported that noise with impulsive and tonal components could annoy people (Hellman, 1985, Gockel et al., 2012). An impulsive noise means a single burst sound for a short duration. Such noise will increase annoyance perception of individuals (Willemsen and Rao, 2010). In Jury Test 1, Sound #1 is an impulsive noise, however, because the maximum SPL level was less than 30 dBA, most of the participants did not find this sound more annoying than other sound samples. Tonality, on the other hand, refers to the harmonics components in the noise. Modern electrical machines with rotating parts such as motors in HDD generate audible tones that would induce noise annoyance (Hellman, 1985). Another sound quality study of vacuum cleaner also confirmed similar results (Yanagisawa et al., 2011). In Sottek's study (Sottek, 2015), he found that consonant tones would please individual and inconsonant tones would annoy people. The pleasantness of a sound was affected by the ratio of the fundamental frequency and the harmonics (Töpken et al., 2010). In Jury Test 1, Sound #2 contained a very high tonal component at around 3240 Hz (the fundamental frequency of the HDD spindle motor). However, the jury test results showed that most of participants were not annoyed by Sound #2 even when it was played at the highest volume. This is most likely because the SPL was only 23.3 dB(A). As mentioned previously in this thesis (Chapter 1), the 2.5" HDD will only generate noise less than 25 dB(A). The tonality component will not be a significant factor at such SPL. On the other hand, Sound #3 was found very annoyed by most of the participants. However, it could be due to the high SPL level (higher than 30 dB(A)) resulted from the volume adjustment procedure in the jury test. When participant adjusted the playback system volume, inevitably the SPL of the sound increased as well as the loudness. The observed relatively good correlation between the participants' annoyance and loudness may not be applicable to HDD because it has already exceeded the common range of SPL in HDD. A new jury test in which no volume adjustment was allowed must be conducted. In this Jury Test 2, sound paired comparison using Bradley-Terry-Luce (BTL) model (Bradley and Terry, 1952, Luce, 1959) was presented.

2.4. Acoustic Jury Test 2

The contents in this section has been submitted to the following journal for publication:

MA, Y. C., CHIN, C. S., Predicting 2.5” Hard Disk Drive Noise Annoyance using Psychoacoustic Metrics and Subjective Sound Paired-Comparison, International Journal of Product Sound Quality, submitted first revision on Oct 2017.

The approach of Jury Test 2 was almost the same as Jury Test 1 (Figure 2-3). The differences lie in the number of sound stimuli, the listening test procedure and the equipment used during listening test:

- 1) Thirteen sounds from randomly selected 2.5” HDDs were used.
- 2) The recorded sounds were then played to the participants through the Head Acoustics™ playback systems.
- 3) The participants were asked to complete the survey shown in Figure 2-14, and the subjective ratings (SR) on selected sound pairs were computed using Bradley-Terry-Luce model (Luce, 1959, Bradley and Terry, 1952). The recorded sounds were processed by the Artemis Suite software to compute the psychoacoustic metrics (PM).
- 4) A correlation study was conducted to find the relationship between SR and PM.

2. Power Management Transition (PMT). This is an HDD operation when the HDD is in a reduced power management state with the drive head still on the disk. This operation may generate the grinding sound.
3. Random Seek. Sounds may be generated when the actuated arm seeks to cover a long distance in the shortest time. These sounds will be similar to high pitch screeching sounds.
4. Random Write/Read. It occurs when the HDD is writing or reading a large amount of data. The sounds generated are random.

A total of 50 HDDs was measured during these above four operations and 13 annoying sounds were selected by the authors for the Jury Test 2. Table 2-4 shows the psychoacoustic parameters such as loudness, roughness and A-weighted SPL for the selected sounds. Among these sounds, Sounds #1 to #3 are Emergency Retract sound, Sounds #4 to #6 are Power Management Transition sound, Sounds #7 to #9 are Random Write/Read sound, and Sounds #9 to #13 are Random Seek sound.

Table 2-4 . Psychoacoustic parameters and SPL for sounds used in Jury Test 2

Noise Sample	Sound characteristics	Loudness (Sone)	Sharpness (Acum)	Fluctuation Strength (Vacil)	Roughness (Asper)	SPL [dB(A)]
1	random sound	0.45	2.21	0.0059	0.0103	24.8
2	random sound	0.40	2.15	0.0051	0.0093	25.0
3	random sound	0.25	2.20	0.0047	0.0079	22.5
4	grinding sound and screeching sound	0.35	1.85	0.0059	0.0104	24.0
5	grinding sound and screeching sound	0.36	1.86	0.0059	0.0106	24.1
6	grinding sound and screeching sound	0.36	1.78	0.0049	0.0093	24.6
7	random write/read	0.41	2.09	0.0073	0.0177	25.4
8	random write/read	0.25	2.38	0.0023	0.0095	22.5
9	random write/read	0.29	2.21	0.0029	0.0130	23.2
10	random seek	0.34	1.80	0.0043	0.0103	25.4
11	random seek	0.50	1.80	0.0051	0.0145	25.4
12	random seek	0.57	1.80	0.0063	0.0173	26.2
13	random seek	0.53	1.81	0.0051	0.0167	25.7

2.4.2. Jury Test 2 procedure and results

Figure 2-15 shows the equipment used in Jury Test 2, which provided an extremely low-background-noise condition when the sound samples were recorded. The sound recordings

were passed to the PEQ V system through the USB. The participant listened the recordings using the Bose noise-cancellation headphone (see Figure 2-15 bottom).



Figure 2-15 Participant taking Jury Test 2 and HEAD Acoustics equipment

It is impossible to conduct a perfect listening test that can measure individual's feeling correctly. There are two approaches: one is the direct scaling that has been used in Jury Test 1, while the other is using the paired comparison from Bradley-Terry-Luce (BTL) model (Bradley and Terry, 1952, Luce, 1959). In the BTL model, the general form of the likelihood function is

$$L = \prod_i \pi_i^{2n(t-1) - \sum_{j \neq i} \sum_k r_{ijk}} \prod_{i < j} (\pi_i + \pi_j)^{-n} \quad (5)$$

where π_1, \dots, π_i denotes as true rating of a particular subjective continuum throughout an experiment and $\pi_i \geq 0$ and $\sum \pi_i = 1$; t is a treatments in the experiment; n as number of repetitions of the design; r_{ijk} as rank of the i th treatment in the k th repetition of the block in which treatment i appears with treatment j .

The duration of the paired comparison test could be very long as participant need to listen all possible combination of the sounds. This is reported in Lee's study (Lee et al., 2013).

A pre-listening test that listened to all the sound samples was conducted first. Results showed that

- the participants need to be very focused in order to listen to the sound and rank responsibly;
- the time taken was more than an hour.
- a shorter jury test is preferred as most participants may feel uncomfortable after a prolonged stay in a room.

To improve the efficiency, a new procedure was established. The participants are requested to compare the sound annoyance level of a sound currently played with that of the sound played right before. When a participant had put on the headphone, he/she was requested to remain silence and calm for 30 seconds before playing the first sound. Then the participant was requested to listen to the first sound and compare the first sound against the silence and rate it as '1 vs. silence'. Similarly, Sound #2 was played after Sound #1, and the feeling was rated as '2 vs. 1'. In this way, the average time taken was drastically reduced to about 10 minutes. A scale of 'much worse, worse, same, better and much better' was used for the participant to describe his/her annoyance feeling of a sound relevant to another. A total of 34 people aged between 18 and 54 took part in Jury Test 2. Each participant listened to all the thirteen sound stimuli. The sequential effect due to the immediately previous and earlier listening enable the listeners to differentiate the annoyance level better as they can recall the noise level before and hence able to judge and provide an accurate comparison of the annoyance levels. As shown in Table 2-4, the order of presentation will not create any bias as the loudness, roughness, and SPL are randomly distributed from Sounds #1 to #13. They are not in an increasing or decreasing order.

2.4.3. BTL analysis

Thirty-four participants were divided into two groups based on their ages, namely the younger age group for participants who aged below 26 and the older age group for participants aged above 30 (there were no participants with age between 26 and 30). Table 2-5 and Table 2-6 summarized the 'preference' matrix. Using the MATLAB script provided (WICKELMAIER and SCHMID, 2004), the BTL scale for each sound was computed. Table 2-7 shows the BTL scales, the psychoacoustic metrics and their correlation of the thirteen sounds for the young and the old age groups respectively. Based on the low multiple R values, there

is no correlation between BTL scales and psychoacoustic metrics for both the young and the old age groups.

Table 2-5 Preference matrix of young age group

(each value shows the number of people who feel sound in respective rows was more annoying than the sound in corresponding columns)

Young Age Group	Sound #1	Sound #2	Sound #3	Sound #4	Sound #5	Sound #6	Sound #7	Sound #8	Sound #9	Sound #10	Sound #11	Sound #12	Sound #13
Sound #1	-	1	6	9	6	9	9	9	12	12	13	14	13
Sound #2	16	-	4	6	5	8	9	9	12	12	13	14	13
Sound #3	11	13	-	3	5	8	9	9	12	12	13	13	13
Sound #4	8	11	14	-	3	7	8	9	12	12	11	13	13
Sound #5	11	12	12	14	-	6	8	9	12	11	12	13	13
Sound #6	8	9	9	10	11	-	8	9	12	11	12	13	13
Sound #7	8	8	8	9	9	9	-	6	11	11	11	12	13
Sound #8	8	8	8	8	8	8	11	-	10	9	13	12	13
Sound #9	5	5	5	5	5	5	6	7	-	3	12	12	13
Sound #10	5	5	5	5	6	6	6	8	14	-	9	11	11
Sound #11	4	4	4	6	5	5	6	4	5	8	-	6	11
Sound #12	3	3	4	4	4	4	5	5	5	6	11	-	8
Sound #13	4	4	4	4	4	4	4	4	4	6	6	9	-

Table 2-6 Preference matrix of the old age group

(each value shows the number of people who feel sound in respective rows was more annoying than the sound in corresponding columns)

Old Age Group	Sound #1	Sound #2	Sound #3	Sound #4	Sound #5	Sound #6	Sound #7	Sound #8	Sound #9	Sound #10	Sound #11	Sound #12	Sound #13
Sound #1	-	6	10	11	9	7	9	8	10	8	10	11	10
Sound #2	11	-	3	6	6	7	8	8	9	9	10	11	9
Sound #3	7	14	-	3	6	5	7	8	9	9	9	12	10
Sound #4	7	11	14	-	7	6	8	10	11	10	10	12	10
Sound #5	8	11	11	10	-	3	8	11	13	9	10	12	11
Sound #6	10	10	12	11	14	-	11	8	12	10	10	11	9
Sound #7	8	9	10	9	9	6	-	8	10	11	10	13	14
Sound #8	9	9	9	7	6	9	9	-	10	8	10	9	10
Sound #9	7	8	8	6	4	5	7	7	-	3	9	8	10
Sound #10	9	8	8	7	8	7	6	9	14	-	10	9	9
Sound #11	7	7	8	7	7	7	7	7	8	7	-	9	12
Sound #12	6	6	5	5	5	6	4	8	9	8	8	-	9
Sound #13	7	8	7	7	6	8	3	7	7	8	5	8	-

Table 2-7 BTL scale and psychoacoustic metrics of each sound and their correlations in different age groups

BTL scale		Loudness	Sharpness	Roughness	Flu. Str.	SPL
Young Age Group	Old Age Group	[sone]	[acum]	[asper]	[vacil]	[dBA]
0.086	0.086	0.447	2.50	0.010	0.006	24.8
0.100	0.070	0.398	2.40	0.009	0.005	25.0
0.100	0.072	0.245	2.44	0.008	0.005	22.5
0.100	0.098	0.345	2.03	0.010	0.006	24.0
0.128	0.101	0.356	2.06	0.011	0.006	24.1
0.108	0.125	0.357	2.02	0.009	0.005	24.6
0.089	0.101	0.405	2.45	0.018	0.007	25.4
0.091	0.081	0.247	2.75	0.009	0.002	22.5
0.048	0.053	0.286	2.47	0.013	0.003	23.2
0.056	0.079	0.343	2.00	0.010	0.004	25.4
0.035	0.065	0.503	2.18	0.015	0.005	25.4
0.031	0.050	0.567	2.26	0.017	0.005	26.2
0.028	0.052	0.527	2.21	0.017	0.006	25.7
Correlation in young age group		-0.59	0.01	-0.67	0.13	-0.49
Correlation in old age group		-0.35	-0.30	-0.40	0.29	-0.15

In addition to the psychoacoustic metrics such as loudness, sharpness, roughness and fluctuation strength, psychoacoustic annoyance (PA) has also been used to express these psychoacoustic metrics as in (Fastl and Zwicker, 2007)

$$PA = N_5 \left(1 + \sqrt{\omega_s^2 + \omega_{FR}^2} \right) \quad (6)$$

where

$$\omega_s = \left(\frac{S}{acum} - 1.75 \right) \cdot 0.25 \log \left(\frac{N_5}{sone} + 10 \right) \quad \text{for } S > 1.75$$

$$\omega_{FR} = \frac{2.18}{(N_5 / sone)^{0.4}} \left(0.4 \cdot \frac{F}{vacil} + 0.6 \cdot \frac{R}{asper} \right)$$

and N_5 indicates the percentile Loudness in sone.

With Equation (6), the PA value and its associated parameters were computed. Linear multiple correlation was first studied. Table 2-8 summarizes the multiple regression analysis results between the BTL scale and the PA value. No relations were found to have both high R value and low p-value, hence it was concluded that no strong linear relationship could be

established. In other words, the relationship between the obtained BTL scale and the psychoacoustic metrics could be nonlinear.

An artificial neural network (ANN) was then used to obtain this nonlinear and new relationship. The ANN with back-propagation (Brocolinia et al., 2012) was used to approximate the relationship between the psychoacoustic metrics and the BTL scales obtained in Jury Test 2. The inputs are the loudness, roughness and SPL (as shown in Table 2-8), and the output is the BTL scale values achieved over the paired comparison test for both the young and the old age groups. 50% of the data were used for the training, 30% for varication and 20% for testing. Figure 2-16 shows that the values predicted from the model fit the obtained BTL scale values accurately with $R^2=0.999$ for the young age group and $R^2=0.961$ for the old age group.

Table 2-8 P-value for different age groups

Parameters	R _{young}	P _{young}	R _{old}	P _{old}	Comments
N ₅	0.574	0.040	0.220	0.471	Not significant
ω_s	0.282	0.350	0.107	0.729	Not significant
ω_{fr}	0.527	0.065	0.288	0.340	Not significant
PA	0.572	0.041	0.300	0.319	Not significant

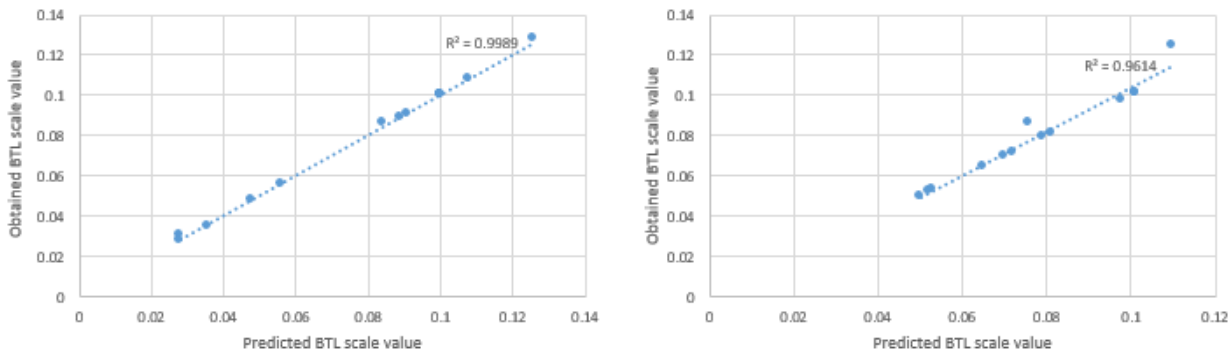


Figure 2-16 Correlation between neural network predicted and actual BTL scale for young age group (left) and older group (right)

2.4.4. Emotional state study

It is assumed that the emotional response to sound varies from person to person due to an interaction between the listeners, the sound source and the environment (TAJADURA-JIMÉNEZ, 2008). In Jury Test 2, a total of 34 participants listened to the 13 sounds and rated each sound on the scale of “much worse, worse, same, better and much better” as compared to the previously heard sound. The participants were also asked to identify their current emotional state as one of the following: stressed, sad, angry, annoyed, excited, calm and happy (as shown in Figure 2-14). The assessment of the emotional states was done at the beginning of the test, and was repeated after each new HDD’s sound event was played, i.e., after random sounds, after power manage transition sounds, after random write/read sounds and after random seek sounds. As shown in Figure 2-17, the emotional states of most participants changed over the jury test. Although the fluctuation of emotional state varied from person to person, the general observation is that more participants felt an increase in annoyance after listening to one type or several types of sounds.

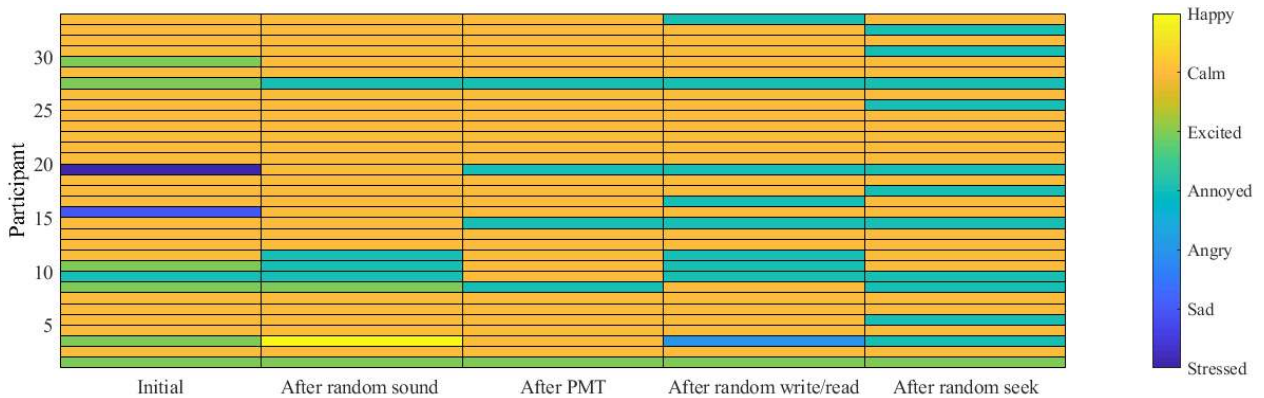


Figure 2-17 Emotional states of 34 participants on different HDD sound events

The impact of participants’ emotional states should always be considered when analyzing the jury test results. First, the limited room auralization and the selection of sound sources may make it difficult to generalize the results. Second, it can be quite useful to conduct a same study where participants are mostly in the same emotional condition since the differences in their emotional state could have influenced in the results. However, it may be difficult to find such groups of participants. Third, social surveys could have shown the different usage patterns of people, such as certain groups tend to spend more time on laptops. Additionally, it is worth to investigate how multisensory interaction affects emotional processing and perception of the room at different times of the day.

```

MATLAB script used in incomplete paired comparison calculation
function [p,chistat,u,LL_eba,LL_sat,fit,cova] = OptiPt(M,A,s)
% OptiPt parameter estimation for BTL/Pretree/EBA models
% p = OptiPt(M,A) estimates the parameters of a model specified
% in A for the paired-comparison matrix M. M is a matrix with
% absolute frequencies. A is a cell array.
% [p,chistat,u] = OptiPt(M,A) estimates parameters and reports
% the chi2 statistic as a measure of goodness of fit. The vector
% of scale values is stored in u.
%
% [p,chistat,u,LL_eba,LL_sat,fit,cova] = OptiPt(M,A,s) estimates
% parameters, checks the goodness of fit, computes the scale values,
% reports the log-likelihoods of the model specified in A and of the
% saturated model, returns the fitted values and the covariance
% matrix of the parameter estimates. If defined, s is the starting
% vector for the estimation procedure. Otherwise each starting value
% is set to 1/length(p).
% The minimization algorithm used is FMINSEARCH.
%
% Examples
% Given the matrix M =
%      0  36  35  44  25;
%     19  0  31  37  20
%     20  24  0  46  24
%     11  18  9  0  13
%     30  35  31  42  0
%
% A BTL model is specified by A = {[1];[2];[3];[4];[5]}
% Parameter estimates and the chi2 statistic are obtained by
% [p,chistat] = OptiPt(M,A)
%
% A Pretree model is specified by A = {[1 6];[2 6];[3 7];[4 7];[5]}

```

```

% A starting vector is defined by s = [2 2 3 4 4 .5 .5]
% Parameter estimates, the chi2 statistic, the scale values, the
% log-likelihoods of the Pretree model and of the saturated model,
% the fitted values, and the covariance matrix are obtained by
% [p,chistat,u,lL_eba,lL_sat,fit,cova] = OptiPt(M,A,s)
%
% Authors: Florian Wickelmaier (wickelmaier@web.de) and Sylvain Choisel
% Last mod: 03/JUL/2003
% For detailed information see Wickelmaier, F. & Schmid, C. (2004). A Matlab
% function to estimate choice model parameters from paired-comparison data.
% Behavior Research Methods, Instruments, and Computers, 36(1), 29-40.

```

```

I = length(M); % number of stimuli
mmm = 0;
for i = 1:I
    mmm = [mmm max(A{i})];
end
J = max(mmm); % number of pt parameters
if(nargin == 2)
    p = ones(1,J)*(1/J); % starting values
elseif(nargin == 3)
    p = s;
end

```

```

for i = 1:I
    for j = 1:I
        diff{i,j} = setdiff(A{i},A{j}); % set difference
    end
end
end

```

```

p = fminsearch(@ebalik,p,optimset('Display','iter','MaxFunEvals',10000,...
    'MaxIter',10000),M,diff,I); % optimized parameters

```

```
ll_eba = -ebalik(p,M,diff,I); % likelihood of the specified model
```

```
ll_sat = 0; % likelihood of the saturated model
```

```
for i = 1:I-1
```

```
    for j = i+1:I
```

```
        ll_sat = ll_sat + M(i,j)*log(M(i,j)/(M(i,j)+M(j,i)))...  
            + M(j,i)*log(M(j,i)/(M(i,j)+M(j,i)));
```

```
    end
```

```
end
```

```
fit = zeros(I); % fitted PCM
```

```
for i = 1:I-1
```

```
    for j = i+1:I
```

```
        fit(i,j) = (M(i,j)+M(j,i))/(1+sum(p(diff{j,i}))/sum(p(diff{i,j})));
```

```
        fit(j,i) = (M(i,j)+M(j,i))/(1+sum(p(diff{i,j}))/sum(p(diff{j,i})));
```

```
    end
```

```
end
```

```
chi = 2*(ll_sat-ll_eba);
```

```
df = I*(I-1)/2 - (J-1);
```

```
chistat = [chi df]; % 1-chi2cdf(chi,df); % goodness-of-fit statistic
```

```
u = sum(p(A{1}) % scale values
```

```
for i = 2:I
```

```
    u = [u sum(p(A{i}))];
```

```
end
```

```
H = hessian('ebalik',p',M,diff,I);
```

```
C = inv([H ones(J,1); ones(1,J) 0]);
```

```
cova = C(1:J,1:J);
```

```
function ll_eba = ebalik(p,M,diff,I) % computes the likelihood
```

```

if min(p)<=0 % bound search space
    LL_eba = inf;
    return
end

thesum = 0;
for i = 1:I-1
    for j = i+1:I
        thesum = thesum + M(i,j)*log(1+sum(p(diff{j,i}))/sum(p(diff{i,j})))...
            + M(j,i)*log(1+sum(p(diff{i,j}))/sum(p(diff{j,i})));
    end
end
LL_eba = thesum;
function H = hessian(f,x,varargin) % computes numerical Hessian
k = size(x,1);
fx = feval(f,x,varargin{:});
h = eps.^(1/3)*max(abs(x),1e-2);
xh = x+h;
h = xh-x;
ee = sparse(1:k,1:k,h,k,k);
g = zeros(k,1);
for i = 1:k
    g(i) = feval(f,x+ee(:,i),varargin{:});
end
H = h*h';
for i = 1:k
    for j = i:k
        H(i,j) = (feval(f,x+ee(:,i)+ee(:,j),varargin{:})-g(i)-g(j)+fx)...
            / H(i,j);
        H(j,i) = H(i,j);
    end
end
end

```

Ethical approval for using human participants

SECTION 5: Human Participants in a Non-Clinical Setting

	YES	NO
Does the research involve human participants e.g. use of questionnaires, focus groups, observation or surveys? (if you are unsure please tick 'Yes' and complete the sub-questions)	<input checked="" type="checkbox"/>	<input type="checkbox"/>

If you answered NO to this question, please go to Section 6
If you answered YES to this question, please complete the rest of the questions below:

	YES	NO
a. Does the study involve other vulnerable groups, as defined in Section 52 of the Safeguarding Vulnerable Adults Act 2006 as those who are relatively or absolutely incapable of protecting their own interests, or those in unequal relationships e.g. your own students?	<input type="checkbox"/>	<input checked="" type="checkbox"/>
b. Will the study require the co-operation of a gatekeeper for initial access to the groups or individuals to be recruited e.g. students at school, members of a self-help group, or residents of a nursing home?	<input type="checkbox"/>	<input checked="" type="checkbox"/>
c. Will it be necessary for participants to take part in the study without their knowledge and consent e.g. covert observation of people in non-public places?	<input type="checkbox"/>	<input checked="" type="checkbox"/>
d. Will this study involve deliberately misleading participants in any way?	<input type="checkbox"/>	<input checked="" type="checkbox"/>
e. Will the study involve discussion of sensitive topics e.g. sexual activity or drug use?	<input type="checkbox"/>	<input checked="" type="checkbox"/>
f. Are any drugs, placebos or other substances (e.g. food substances, vitamins) to be administered to the study participants or will the study involve invasive, intrusive or potentially harmful procedures of any kind?*	<input type="checkbox"/>	<input checked="" type="checkbox"/>
g. Will blood or tissue samples be obtained from subjects?*	<input type="checkbox"/>	<input checked="" type="checkbox"/>
h. Is pain or more than mild discomfort likely to result from the study?	<input type="checkbox"/>	<input checked="" type="checkbox"/>
i. Could the study induce psychological stress or anxiety or cause harm or negative consequences beyond the risks encountered in normal life?	<input type="checkbox"/>	<input checked="" type="checkbox"/>
j. Will the study involve prolonged or repetitive testing?	<input type="checkbox"/>	<input checked="" type="checkbox"/>
k. Will financial inducements (other than reasonable expenses and compensation for time) be offered to participants?	<input type="checkbox"/>	<input checked="" type="checkbox"/>

* Please Note: Depending on the details of this project, this may require NHS approval. You will be given further clarification if the project is awarded. You are also advised to consult the [JRD Policy Regarding the Participation of Volunteers in Research Projects](#)

If you have answered YES to any of questions in Section 5, you will need to describe more fully how you plan to deal with the ethical issues raised by your research by completing the Full Ethical Approval application form (after your project has successfully been awarded). Please continue with the rest of the form.



Louise Jones
Fri 7/29/2016, 5:29 PM



Re: Confirmation of ethical approval

Dear Yichao,

Having reviewed the Preliminary Ethics Form submitted for this project, I am satisfied that no further action is required. Although the use of human participants is indicated in Section 5, the following sub questions have all been answered "no". This indicates that the study can be classified as low risk.

I am therefore happy to provide approval on behalf of the Faculty Ethics Committee.

Please let me know if you need anything further from me.

Best Wishes,

Louise

Louise Jones
Faculty Research Administrator
SAGe Faculty

Chapter 3. Theoretical formulation

With the understanding that acoustic perceptions can be predicted using the psychoacoustic metrics, which can be computed from the measured acoustic pressure, this chapter attempts to provide the detailed and complete formulation of the 2.5" HDD vibro-acoustic transfer function (VaTF) at the near-field that can be used to calculate the acoustic pressure.

The contents in this Chapter has been submitted to the following journal for publication:

- Near-Field Vibro-Acoustic Transfer Function Prediction of Small Close Fit Enclosure with Multiple Rotating Components, Applied Acoustics, submitted in Jan 2018.

3.1. Overview and assumptions

A typical 2.5" HDD comes with the following dimensions: 10 cm (length) \times 7 cm (width) \times 0.7 cm (thickness).



Figure 3-1 Near field calculating/measuring layer for 2.5" HDD

To analyze it, the following statements and assumptions have been made:

1. The spindle motor rotates at 5400 rpm or 90 revolutions per second. It is simulated as a point source and denoted with $Q^{(S)}$.
2. The disk is 65 mm in diameter and 0.635 mm in thickness. A superscript 'D' is used.

3. Since 15 cm³ volume of air is very small, the windage noise due to rotating disk will not be considered.
4. The Head Stack Actuator (HSA) is a stainless steel part in triangle shape with an average thickness of 0.6 mm. A superscript 'A' is used.
5. The Voice Coil Motor (VCM) is a motor that controls the HSA motion. The pivot bearing is simulated as another point source and assumed to have a different frequency from the spindle motor. It is denoted as Q^(A).
6. The main source of mechanical vibration is the forces generated by the VCM motor and the spindle motor. The forces from other parts are not considered.
7. The cover and the base are considered as the casing of the HDD. The cover is a thin aluminum plate with a constant thickness of 0.35 mm.
8. The clearances between the cover and the disk, as well as that between the cover and the HSA, are small. Hence, sound energy due to reflection is very small and is not considered in the analysis.
9. There is no cancellation effect between two point sources as they have different point source strengths.

The disk spindle motor ($\phi^{(D)}$), the HDD stationary parts ($\phi^{(S)}$) and the head actuator ($\phi^{(A)}$) are used in the vibro-acoustic model analysis. Hence, the total velocity potential (ϕ_{total}) outside the HDD casing can be estimated as

$$\phi_{total} \approx A\phi_{point\ sources} + B\phi^{(S)} + C\phi^{(D)} + D\phi^{(A)} \quad (7)$$

where A, B, C and D are arbitrary weighting functions. The velocity potential (ϕ) is used because it conveniently relates to air particle velocity and pressure, p , as shown. (Baek, 1999)

$$\dot{u} = \frac{\partial \phi}{\partial x}, \dot{v} = \frac{\partial \phi}{\partial y}, \dot{w} = \frac{\partial \phi}{\partial z} \quad (8)$$

$$p = -\rho \frac{\partial \phi}{\partial t} \quad (9)$$

where \dot{u} , \dot{v} and \dot{w} are the air velocities with respect to the corresponding axes. ρ is the air density.

Recall Equation (4)

$$p(x, y, z) = \frac{j\rho ck}{2\pi} \int_S v_p(x, y) \frac{e^{-jkR}}{R} dS$$

Substituting (8) into (4) to obtain the expression of predicting the far field acoustic pressure:

$$p(x, y, z) = \frac{j\rho ck}{2\pi} \int_S \dot{w} \frac{e^{-jkR}}{R} dS$$

Finite Element Method (FEM) is an approximate numerical method suitable for providing an estimated solution for boundary volume problems. It starts with idealizing a structure with many small elements known as finite elements, which are connected with nodes. In the following sections, this method will be used to formulate the approximate velocity potential for each parts, starting with two point sources.

3.2. Two point sources

The inhomogeneous wave equation takes the form of (10)

$$\nabla^2 \phi - \frac{1}{c^2} \frac{d^2 \phi}{dt^2} = -Q \quad (10)$$

where, k is the wavenumber and can be computed as $k = \frac{\omega}{c}$ and Q is the external sound field in this case. It is the sound field due to the point source, and it can be computed by

$$Q = j\omega\rho_0q \quad (11)$$

where $j = \sqrt{-1}$, ω is the angular velocity and $\omega = 2\pi f$, ρ_0 is medium density (Baek;, 1999). The analysis refers to the air density in the HDD, and q is the strength of the point source, having a unit of volume velocity per unit volume.

And ϕ is the three dimensional (3D) velocity potential which can be calculated as

$$\phi(x, y, z, t) = \tilde{\phi}(x, y, z)e^{j\omega t} \quad (12)$$

where $\tilde{\phi}(x, y, z)$ is the amplitude of $\phi(x, y, z, t)$.

Taking the time derivative of (12) gives

$$\begin{aligned} \frac{d\phi}{dt} &= j\omega\phi \\ \frac{d^2\phi}{dt^2} &= -\omega^2\phi \end{aligned} \quad (13)$$

The wavenumber, k is defined as

$$k = \frac{\omega}{c} \quad (14)$$

Substitute (13) and (10) thus,

$$\begin{aligned} \nabla^2 \phi - \left(-\frac{\omega^2 \phi}{c^2} \right) + Q &= 0 \\ \nabla^2 \phi + \left(\frac{\omega}{c} \right)^2 \phi + Q &= 0 \end{aligned}$$

By applying equation (13),

$$\nabla^2 \phi + k^2 \phi + Q = 0 \quad (15)$$

Equation (15) is a second order differential equation that is difficult to solve. Weighted residual methods have been widely used by many researchers to solve such an equation, for example, by Wu (Wu and Seybert, 1991) and P. Goransson (Goransson, 1995). It starts with computing the residual in equation (16):

$$R = \int_V W_i(x, y, z) (\nabla^2 \phi + k^2 \phi + Q) dV \quad (16)$$

where R is the residual and $W_i(x, y, z)$ is the independent weight function. To minimize the residual, i.e., setting $R \rightarrow 0$,

$$\int_V W_i(x, y, z) [(\nabla^2 + k^2)\phi + Q] dV = 0 \quad (17)$$

Green's first identity (Strauss, 2007) states that

$$\int_V [\phi \nabla^2 \varphi + (\nabla \phi) \cdot (\nabla \varphi)] dV = \oint_{\partial V} \phi (\nabla \varphi \cdot \mathbf{n}) dS \quad (18)$$

where ϕ and φ are the scalar functions in the region V , ∇^2 is the Laplace operator, ∇ is the gradient, ∂V is the boundary surface for the region V , and \mathbf{n} is the outward pointing unit normal of boundary surface.

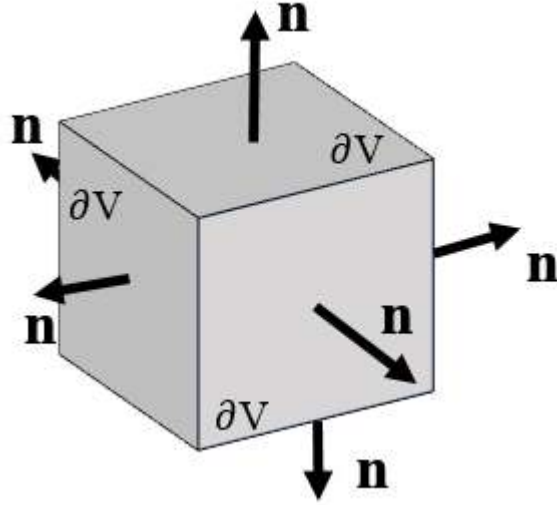


Figure 3-2 Green's first Identity

By rearranging (18) gives

$$\begin{aligned} \int_V \phi \nabla^2 \phi dV + \int_V (\nabla \phi) \cdot (\nabla \phi) dV &= \oint_{\partial V} \phi (\nabla \phi \cdot \mathbf{n}) dS \\ \int_V \phi \nabla^2 \phi dV &= \oint_{\partial V} \phi (\nabla \phi \cdot \mathbf{n}) dS - \int_V (\nabla \phi) \cdot (\nabla \phi) dV \end{aligned} \quad (19)$$

Equation (19) can be used to reduce the second order differential equation to first order differential equations.

Applying the equation (19) to (17) results in the following derivation:

$$\begin{aligned} \int_V [W_i(x, y, z)(\nabla^2 \phi) + W_i(x, y, z)k^2 \phi + W_i(x, y, z)Q] dV &= 0 \\ \int_V W_i(x, y, z)(\nabla^2 \phi) dV + \int_V [W_i(x, y, z)k^2 \phi + W_i(x, y, z)Q] dV &= 0 \\ \oint_{\partial V} W_i(\nabla \phi \cdot \mathbf{n}) dS - \int_V (\nabla W_i) \cdot (\nabla \phi) dV + \int_V (W_i k^2 \phi + W_i Q) dV &= 0 \\ \oint_{\partial V} W_i(\nabla \phi \cdot \mathbf{n}) dS - \int_V (\nabla W_i) \cdot (\nabla \phi) dV + \int_V W_i k^2 \phi dV + \int_V W_i Q dV &= 0 \\ \oint_{\partial V} W_i(\nabla \phi \cdot \mathbf{n}) dS + \int_V W_i Q dV - \int_V (\nabla W_i) \cdot (\nabla \phi) dV + \int_V W_i k^2 \phi dV &= 0 \\ - \int_V (\nabla W_i) \cdot (\nabla \phi) dV + \int_V W_i k^2 \phi dV = - \oint_{\partial V} W_i(\nabla \phi \cdot \mathbf{n}) dS - \int_V W_i Q dV \\ \int_V (\nabla W_i) \cdot (\nabla \phi) dV - \int_V W_i k^2 \phi dV = \oint_{\partial V} W_i(\nabla \phi \cdot \mathbf{n}) dS + \int_V W_i Q dV \end{aligned} \quad (20)$$

One can define the outflow over surface S as γ and

$$\gamma = \nabla\phi \cdot \mathbf{n} \quad (21)$$

$$\tilde{\phi}(x, y, z) = \sum_{m=1}^M \phi_m N_m(x, y, z) \quad (22)$$

where M is total number of modals, the subscript m in ϕ_m means the m^{th} modal, and $N_m(x, y, z)$ is its corresponding shape function.

Many techniques can be used to determine the weight function, one of which is the Galerkin Method and has been used by R. J. Astley (Astley and Eversman, 1978). In the Galerkin method, the shape function can be used as a weight function:

$$W_i(x, y, z) = N_m(x, y, z) \quad (23)$$

where $m = 1, 2, \dots, M$.

Substituting (21), (22) and (23) into (20) gives,

$$\int_V (\nabla N_n) \cdot \left(\nabla \sum_{m=1}^M \phi_m N_m \right) dV - \int_V N_n k^2 \sum_{m=1}^M \phi_m N_m dV = \oint_{\partial V} N_n \gamma dS + \int_V N_n Q dV \quad (24)$$

The derivatives on ϕ are related to the derivatives of the shape functions N_m . In other words,

$$\frac{\partial \phi}{\partial x} = \sum_{m=1}^M \phi_m \frac{\partial N_m}{\partial x}; \quad \frac{\partial \phi}{\partial y} = \sum_{m=1}^M \phi_m \frac{\partial N_m}{\partial y}; \quad \frac{\partial \phi}{\partial z} = \sum_{m=1}^M \phi_m \frac{\partial N_m}{\partial z} \quad (25)$$

$$\sum_{m=1}^M \left(\phi_m \int_V \nabla N_m \nabla N_n dV - k^2 \phi_m \int_V N_m N_n dV \right) = \int_S \gamma N_n dA + \int_V Q N_n dV \quad (26)$$

where $n = 1, 2, \dots, N$.

Thus, equation (22) is obtained,

$$-k^2 c^2 \mathbf{M}_a \phi_a + \mathbf{K}_a \phi_a = \mathbf{f}_a + \mathbf{Q}_{\text{source}} \quad (27)$$

where \mathbf{K}_a is the $m \times n$ stiffness matrix in acoustic domain, \mathbf{M}_a is the $m \times n$ mass matrix in acoustic domain and both \mathbf{M}_a and \mathbf{K}_a are diagonal matrix ((Filippi, 1983), (Nehete et al., 2015)). \mathbf{f}_a is $n \times 1$ force matrix in acoustic domain, $\mathbf{Q}_{\text{source}}$ is the acoustic source matrix, and ϕ_a is the velocity potential matrix.

$$\mathbf{K}_a = \int_V \nabla N_m \nabla N_n dV$$

$$\mathbf{M}_a = \frac{1}{c^2} \int_V N_m N_n dV$$

$$\mathbf{f}_a = \int_S \gamma N_n dA$$

$$\mathbf{Q}_{\text{source}} = \int_V Q N_n dV$$

$$\phi_a = \phi_m$$

Apply equation (14) to (27) results in

$$\begin{aligned} -\left(\frac{\omega}{c}\right)^2 c^2 \mathbf{M}_a \phi_a + \mathbf{K}_a \phi_a &= \mathbf{f}_a + \mathbf{Q}_{\text{source}} \\ \mathbf{M}_a (-\omega^2 \phi_a) + \mathbf{K}_a \phi_a &= \mathbf{f}_a + \mathbf{Q}_{\text{source}} \end{aligned} \quad (28)$$

Recall equation (13)

$$\frac{d^2 \phi}{dt^2} = -\omega^2 \phi$$

Hence, equation (28) becomes

$$\mathbf{M}_a \ddot{\phi}_a + \mathbf{K}_a \phi_a = \mathbf{f}_a + \mathbf{Q}_{\text{source}} \quad (29)$$

Therefore, equation (29) is the force excitation equation in acoustic domain used in this analysis.

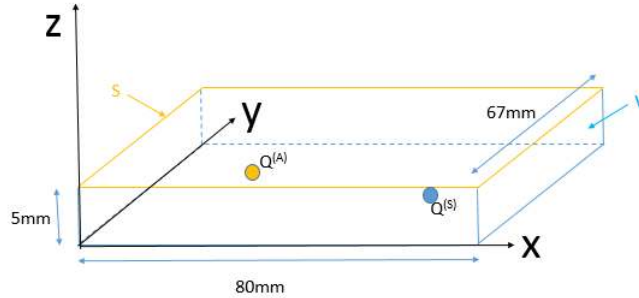


Figure 3-3 A schematic diagram of HDD internal with two point sources

Define the boundary condition used in this computation:

$$\text{At } x = 0 \text{ and } x = 80 \text{ mm, } \frac{\partial \phi}{\partial x} = 0;$$

At $y = 0$ and $y = 67 \text{ mm}$, $\frac{\partial \phi}{\partial y} = 0$;

At $z = 0$, $\frac{\partial \phi}{\partial z} = 0$;

At $z = 5 \text{ mm}$, $\frac{\partial \phi}{\partial z} = \gamma$.

The superposition is applied to both point sources, hence,

$$\mathbf{Q}_{\text{source}} = Q^{(A)} + Q^{(S)} = j\omega\rho_0[q^{(A)} + q^{(S)}] \quad (30)$$

J. Pan (Baek, 1999) also pointed out that the shape function can be written as

$$N_m(x, y, z) = N_{abc}(x, y, z) = \cos \frac{a\pi x}{L_x} \cos \frac{b\pi y}{L_y} \cos \frac{c\pi z}{L_z} \quad (31)$$

Hence,

$$N_m(x, y, z) = N_{abc}(x, y, z) = \cos \frac{a\pi x}{80} \cos \frac{b\pi y}{65} \cos \frac{c\pi z}{5} \quad (32)$$

The point source can be computed by

$$\begin{aligned} \mathbf{Q}_{\text{source}} = j\omega\rho_0 [& q^{(A)} \cos \frac{a\pi x^{(A)}}{80} \cos \frac{b\pi y^{(A)}}{65} \cos \frac{c\pi z^{(A)}}{5} \\ & + q^{(S)} \cos \frac{a\pi x^{(S)}}{80} \cos \frac{b\pi y^{(S)}}{65} \cos \frac{c\pi z^{(S)}}{5}] \end{aligned} \quad (33)$$

From equation (27)

$$\begin{aligned} -k^2 \mathbf{M}_a \phi_a + \mathbf{K}_a \phi_a &= \mathbf{f}_a + \mathbf{Q}_{\text{source}} \\ (-k^2 \mathbf{M}_a + \mathbf{K}_a) \phi_a &= \mathbf{f}_a + \mathbf{Q}_{\text{source}} \\ \phi_{\text{point source}} &= (-k^2 \mathbf{M}_a + \mathbf{K}_a)^{-1} (\mathbf{f}_a + \mathbf{Q}_{\text{source}}) \end{aligned} \quad (34)$$

Equation (34) is the equation used to calculate the velocity potential due to the point sources.

3.3. HDD Stationary parts

HDD can be divided into two parts based on their characteristics, i.e. the stationary components and the rotational components. The stationary components are the non-moving parts which are the spindle motor stator, the base, the VCM magnetic poles and the cover. Unlike the 3.5" HDD, the thickness of 2.5" HDD is much thinner. As a result, the baseplate in the 2.5" HDD becomes more flexible in the HDD. Figure 3-4 shows the flow chart of the

analysis methods. It starts with force excited vibration formulation followed by the coupled vibro-acoustic formulation.

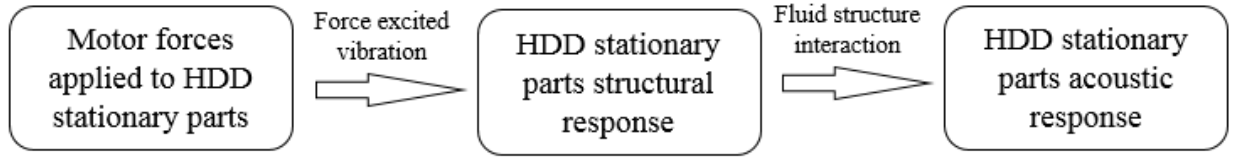


Figure 3-4. The flow chart for the acoustic analysis on HDD stationary components

W. Tseng (Tseng et al., 2003) presented their work on the mathematic model of the flexible HDD casing. The detail derivation is shown below. The HDD casing is defined in the XYZ coordinate system as shown in Figure 3-5. The corresponding unit vector is I, J and K. An arbitrary point P is located on the casing.

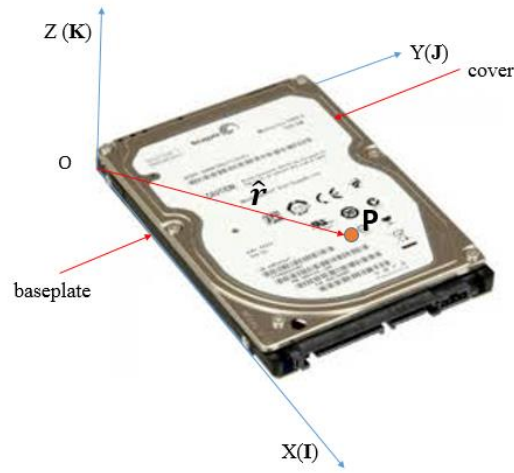


Figure 3-5 A type 2.5" HDD drive casing with an arbitrary point P

The displacement of P due to elastic deformation can be written as

$$P(\hat{\mathbf{r}}, t) = \sum_{n=1}^{\infty} W_n^{(c)}(\hat{\mathbf{r}}) q_n^{(c)}(t) \quad (35)$$

where $\hat{\mathbf{r}}$ is the position vector of point P, superscript (c) refers to the cover, W_n is the nth mode shape, and q_n is the corresponding general coordinate.

In XYZ coordinate system, $W_n(\hat{\mathbf{r}})$ can also be represented as

$$W_n^{(c)}(\hat{\mathbf{r}}) = W_{xn}^{(c)}(\hat{\mathbf{r}})\mathbf{I} + W_{yn}^{(c)}(\hat{\mathbf{r}})\mathbf{J} + W_{zn}^{(c)}(\hat{\mathbf{r}})\mathbf{K} \quad (36)$$

These mode shapes are orthonormal. From equation (36), the velocity of point P can be written as

$$\dot{P}(\hat{r}, t) = \sum_{n=1}^{\infty} W_n^{(C)}(\hat{r}) \dot{q}_n^{(C)}(t) \quad (37)$$

The kinetic energy, $T^{(C)}$ can be expressed as

$$T^{(C)} = \frac{1}{2} m v^2 = \frac{1}{2} \int \dot{P} \cdot \dot{P} \, dm \quad (38)$$

Substitute (37) to (38) gives

$$T^{(C)} = \frac{1}{2} \int \left[\sum_{m=1}^{\infty} W_m^{(C)}(\hat{r}) \dot{q}_m^{(C)}(t) \right] \cdot \left[\sum_{n=1}^{\infty} W_n^{(C)}(\hat{r}) \dot{q}_n^{(C)}(t) \right] dm$$

$$T^{(C)} = \frac{1}{2} \sum_{m=1}^{\infty} \sum_{n=1}^{\infty} \left[\int W_m^{(C)}(\hat{r}) \cdot W_n^{(C)}(\hat{r}) dm \right] \dot{q}_m^{(C)}(t) \dot{q}_n^{(C)}(t) \quad (39)$$

Two orthogonal functions, $f_m(x)$ and $f_n(x)$, when $m \neq n$, then $\int f_m(x) \cdot f_n(x) dx = 0$. However, when $m = n$, then $\int f_m(x) \cdot f_n(x) dx = 1$. Hence, after applying this property to equation (32)

$$T^{(C)} = \frac{1}{2} \sum_{n=1}^{\infty} \left[\dot{q}_n^{(C)}(t) \right]^2 \quad (40)$$

The potential energy for the rigid body can be expressed as

$$V^{(C)} = \frac{1}{2} k x^2 \quad (41)$$

Where, x is the displacement, k is the stiffness which has a relationship with mass and natural frequency for an undamped system. It is shown in the formula below.

$$\omega_n = \sqrt{\frac{k}{m}}$$

$$k = \omega_n^2 m \quad (42)$$

Where, ω_n is the natural frequency and m is the mass of the rigid body.

Substitute (42) to (41) gives

$$V^{(C)} = \frac{1}{2} \left[\omega_n^{(C)} \right]^2 m x^2$$

$$V^{(C)} = \frac{1}{2} \left[\omega_n^{(C)} \right]^2 (m x^2) \quad (43)$$

In this case, the displacement is P and corresponding mass can be written as $\int dm$, hence,

$$\begin{aligned}
V^{(C)} &= \frac{1}{2} [\omega_n^{(C)}]^2 \int P \cdot P \, dm \\
V^{(C)} &= \frac{1}{2} \int \left[\sum_{m=1}^{\infty} \omega_n^{(C)} W_m^{(C)}(\hat{r}) q_m^{(C)}(t) \right] \cdot \left[\sum_{n=1}^{\infty} \omega_n^{(C)} W_n^{(C)}(\hat{r}) q_n^{(C)}(t) \right] dm \\
V^{(C)} &= \frac{1}{2} \sum_{m=1}^{\infty} \sum_{n=1}^{\infty} \left[\int W_m^{(C)}(\hat{r}) \cdot W_n^{(C)}(\hat{r}) dm \right] \omega_m^{(C)} q_m^{(C)}(t) \omega_n^{(C)} q_n^{(C)}(t)
\end{aligned} \tag{44}$$

Apply the same property of the orthogonal functions, equation (44) becomes

$$V^{(C)} = \frac{1}{2} \sum_{n=1}^{\infty} [\omega_n^{(C)}]^2 \cdot [q_n^{(C)}(t)]^2 \tag{45}$$

The Lagrange equation is used to establish the relationship between the generalized excitation forces with the generalized displacement. It states that

$$\frac{d}{dt} \left(\frac{\partial L}{\partial \dot{q}} \right) - \frac{\partial L}{\partial q} = Q \tag{46}$$

where q is the generalized displacement, \dot{q} is the velocity form of q , Q is the generalized force, and L is the Lagrange operator which can be computed using

$$L = T - V \tag{47}$$

Where, T is the kinetic energy and V is the potential energy.

Substitute (40) and (45) into (47)

$$\begin{aligned}
L^{(C)} &= \frac{1}{2} \sum_{n=1}^{\infty} [\dot{q}_n^{(C)}(t)]^2 - \frac{1}{2} \sum_{n=1}^{\infty} [\omega_n^{(C)}]^2 \cdot [q_n^{(C)}(t)]^2 \\
L^{(C)} &= \frac{1}{2} \sum_{n=1}^{\infty} \left\{ [\dot{q}_n^{(C)}(t)]^2 - [\omega_n^{(C)}]^2 \cdot [q_n^{(C)}(t)]^2 \right\}
\end{aligned} \tag{48}$$

From equation (48),

$$\begin{aligned}
\frac{\partial L}{\partial \dot{q}} &= \frac{\partial}{\partial \dot{q}} \left\{ \frac{1}{2} \sum_{n=1}^{\infty} \left\{ [\dot{q}_n^{(C)}(t)]^2 - [\omega_n^{(C)}]^2 \cdot [q_n^{(C)}(t)]^2 \right\} \right\} \\
\frac{\partial L}{\partial \dot{q}} &= \sum_{n=1}^{\infty} [\dot{q}_n^{(C)}(t)]
\end{aligned} \tag{49}$$

And

$$\begin{aligned}\frac{\partial L}{\partial q} &= \frac{\partial}{\partial q} \left\{ \frac{1}{2} \sum_{n=1}^{\infty} \left\{ [\dot{q}_n^{(C)}(t)]^2 - [\omega_n^{(C)}]^2 \cdot [q_n^{(C)}(t)]^2 \right\} \right\} \\ \frac{\partial L}{\partial q} &= - \sum_{n=1}^{\infty} [\omega_n^{(C)}]^2 \cdot [q_n^{(C)}(t)]\end{aligned}\quad (50)$$

Substitute (49) and (50) into (46),

$$\begin{aligned}\frac{d}{dt} \left\{ \sum_{n=1}^{\infty} [\dot{q}_n^{(C)}(t)] \right\} + \sum_{n=1}^{\infty} [\omega_n^{(C)}]^2 \cdot [q_n^{(C)}(t)] &= \sum_{n=1}^{\infty} Q_n^{(C)} \\ \sum_{n=1}^{\infty} \left\{ [\ddot{q}_n^{(C)}(t)] + [\omega_n^{(C)}]^2 \cdot [q_n^{(C)}(t)] \right\} &= \sum_{n=1}^{\infty} Q_n^{(C)}\end{aligned}\quad (51)$$

Using the same approach for the other stationary components, the generalized equation of motion for the base can be written as

$$\sum_{n=1}^{\infty} \left\{ [\ddot{q}_n^{(B)}(t)] + [\omega_n^{(B)}]^2 \cdot [q_n^{(B)}(t)] \right\} = \sum_{n=1}^{\infty} Q_n^{(B)} \quad (52)$$

For VCM top and bottom pole (52) is written as

$$\sum_{n=1}^{\infty} \left\{ [\ddot{q}_n^{(P)}(t)] + [\omega_n^{(P)}]^2 \cdot [q_n^{(P)}(t)] \right\} = \sum_{n=1}^{\infty} Q_n^{(P)} \quad (53)$$

Combine equation (51), (52) and (53) to form the structure vibration generalized equation of motion

$$\begin{bmatrix} I^{(C)} & 0 & 0 \\ 0 & I^{(B)} & 0 \\ 0 & 0 & I^{(P)} \end{bmatrix} \begin{bmatrix} \ddot{q}_n^{(C)} \\ \ddot{q}_n^{(B)} \\ \ddot{q}_n^{(P)} \end{bmatrix} + \begin{bmatrix} \omega_n^{(C)} & 0 & 0 \\ 0 & \omega_n^{(B)} & 0 \\ 0 & 0 & \omega_n^{(P)} \end{bmatrix} \begin{bmatrix} q_n^{(C)} \\ q_n^{(B)} \\ q_n^{(P)} \end{bmatrix} = \begin{bmatrix} Q_n^{(C)} \\ Q_n^{(B)} \\ Q_n^{(P)} \end{bmatrix} \quad (54)$$

One can define the following terms,

$\mathbf{M}_S^{(S)} = \text{diag}\{[I^{(C)}, I^{(B)}, I^{(P)}]\}$, where $I^{(C)}$, $I^{(B)}$ and $I^{(P)}$ are the identical matrix for the cover, base and pole plates respectively.

$\mathbf{K}_S^{(S)} = \text{diag}\{[\omega_n^{(C)}, \omega_n^{(B)}, \omega_n^{(P)}]\}$, where $\omega_n^{(C)}$, $\omega_n^{(B)}$ and $\omega_n^{(P)}$ are the natural frequencies for the cover, base and pole plates respectively.

$$\mathbf{F}_S^{(S)} = \begin{bmatrix} Q_n^{(C)} \\ Q_n^{(B)} \\ Q_n^{(P)} \end{bmatrix}$$

where $Q_n^{(C)}$, $Q_n^{(B)}$ and $Q_n^{(P)}$ are the generalized force vendors for the cover, base and pole plates respectively.

$$\mathbf{u}_S^{(S)} = \begin{bmatrix} q_n^{(C)} \\ q_n^{(B)} \\ q_n^{(P)} \end{bmatrix}$$

where $q_n^{(C)}$, $q_n^{(B)}$, $q_n^{(P)}$ are generalized displacement vendors for cover base and pole plates.

The subscript S means structural components and superscript (S) refers to the stationary parts. As a result, equation (54) becomes

$$\mathbf{M}_S^{(S)} \ddot{\mathbf{u}}_S^{(S)} + \mathbf{K}_S^{(S)} \mathbf{u}_S^{(S)} = \mathbf{F}_S^{(S)} \quad (55)$$

where \mathbf{M} is the mass matrix, \mathbf{K} is stiffness matrix, \mathbf{F} is the force matrix, and \mathbf{u} is the displacement matrix.

The force excitation in equation (55) consists of two magnetic forces from two motor systems, i.e., the spindle motor and the voice coil motor (VCM). These forces can be obtained using the Maxwell stress tensor method (Sun et al., 2016, Park et al., 2013). The Maxwell stress tensor is a useful method to compute the electromagnetic forces within the electromechanical boundary deduced from the electromagnetic linear and angular momentum balance method (Julian et al., 1998, Wolfgang and Melba, 1962).

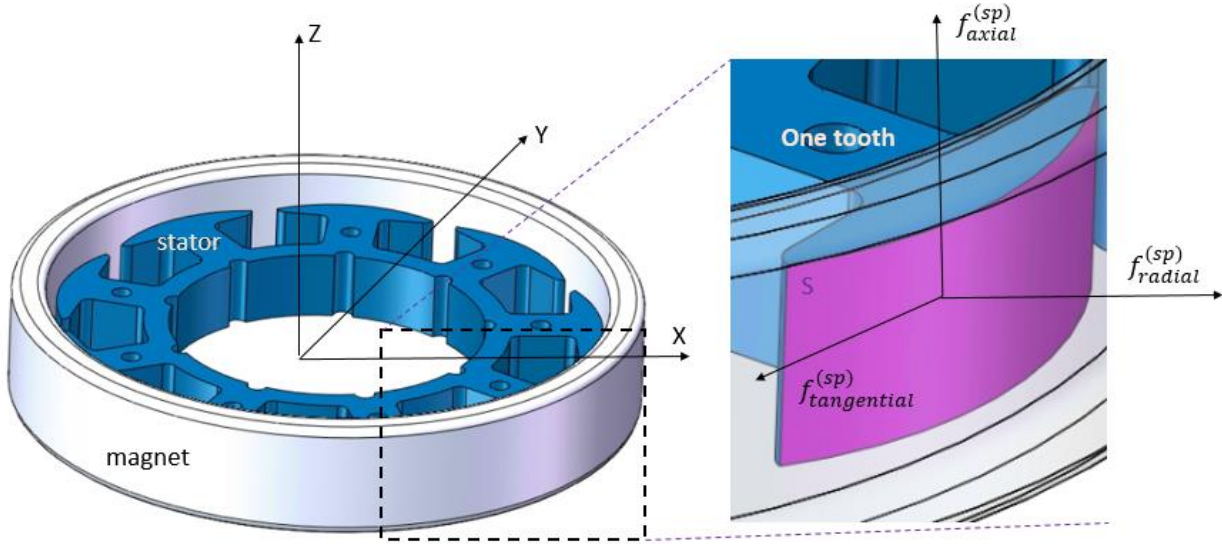


Figure 3-6 The spindle motor forces in a single tooth

For spindle motor, the excitation force (Park et al., 2013) can be calculated by

$$f_n = \frac{1}{2\mu_0} (B_n^2 - B_t^2 - B_z^2) \quad (56)$$

$$f_t = \frac{B_n B_t}{\mu_0} \quad (57)$$

$$f_z = \frac{B_n B_z}{\mu_0} \quad (58)$$

where B_n , B_t , B_z , μ_0 , f_n , f_t and f_z are the normal, tangential and axial flux densities, the permeability of air, the normal, tangential and axial force densities, respectively.

$$f_{radial}^{(sp)} = \int_S (f_n \cos \lambda + f_t \sin \lambda) dS$$

$$f_{tangential}^{(sp)} = \int_S (-f_n \sin \lambda + f_t \cos \lambda) dS$$

$$f_{axial}^{(sp)} = \int_S f_z dS$$

where the superscript (sp) refers to the spindle motor, S is the surface area of a single tooth, λ is the phase angle from the x -axis in the spindle motor, and f is the force.

In the spindle motor, there are several such teeth, hence the motor forces in the direction of x , y and z can be computed by

$$F_x^{(sp)} = \sum_i^{tn} (f_{radial})_i \cos \theta_i + (f_{tangential})_i \sin \theta_i \quad (59)$$

$$F_y^{(sp)} = \sum_i^{tn} -(f_{radial})_i \sin \theta_i + (f_{tangential})_i \cos \theta_i \quad (60)$$

$$F_z^{(sp)} = \sum_i^{tn} (f_{axial})_i \quad (61)$$

$$T^{(sp)} = \sum_i^{tn} R(f_{axial})_i$$

where i is the specific number of the teeth, tn is the total number of the teeth in the spindle motor, R is the radius of the motor, θ_i is the angle of the i^{th} tooth from the x-axis, and F_x , F_y and F_z are the spindle motor forces in the x, y and z directions respectively.

As for the VCM, the magnetic torque can be calculated with Lorentz's force (Jang et al., 2007).

$$T^{VCM} = l_c \int_A r_v J_c B_z^{VCM} dA \quad (62)$$

where l_c is the equivalent coil length, r_v is the radius from pivot point to magnetic field, J_c is the current density of coil and B_z^{VCM} is the axial magnetic flux density of a VCM.

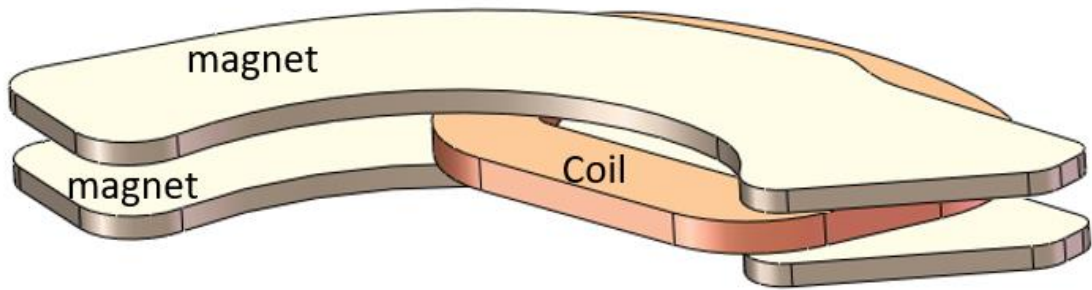


Figure 3-7 The VCM used in a 2.5" HDD

For harmonic response,

$$\mathbf{u}_s^{(s)}(t) = \mathbf{U}e^{i\omega t} \quad (63)$$

Where, \mathbf{U} is the complex and ω is the angular frequency which can be obtained by

$$\omega = 2\pi f$$

Hence,

$$\begin{aligned}\dot{\mathbf{u}}_S^{(S)}(t) &= i\omega \mathbf{U} e^{i\omega t} \\ \dot{\mathbf{u}}_S^{(S)}(t) &= i\omega \mathbf{u}_S^{(S)}(t)\end{aligned}\tag{64}$$

And

$$\ddot{\mathbf{u}}_S^{(S)}(t) = -\omega^2 \mathbf{u}_S^{(S)}(t)\tag{65}$$

Substitute (65) to (55) gives

$$\begin{aligned}\mathbf{M}_S^{(S)}(-\omega^2 \mathbf{u}_S^{(S)}) + \mathbf{K}_S^{(S)} \mathbf{u}_S^{(S)} &= \mathbf{F}_S^{(S)} \\ [-\omega^2 \mathbf{M}_S^{(S)} + \mathbf{K}_S^{(S)}] \mathbf{u}_S^{(S)} &= \mathbf{F}_S^{(S)} \\ \mathbf{u}_S^{(S)} &= [-\omega^2 \mathbf{M}_S^{(S)} + \mathbf{K}_S^{(S)}]^{-1} \mathbf{F}_S^{(S)}\end{aligned}\tag{66}$$

Recall equation (21)

$$\gamma = \nabla\phi \cdot \mathbf{n}$$

where γ is the acoustic particle velocity, which is normal to the acoustic domain surface. Nickolas (Nickolas Vlahopoulos et al., 1999) pointed out that the normal particle velocity can be equal to the surface velocity, which is normal to acoustical boundary surface. Hence,

$$\nabla\phi \cdot \mathbf{n} = \dot{\mathbf{u}}_S \cdot \mathbf{n}\tag{67}$$

Substitute equation (21) and (64) to (67)

$$\gamma = i\omega \mathbf{u}_S^{(S)} \cdot \mathbf{n}\tag{68}$$

Recall equation (29)

$$\mathbf{M}_a(-\omega^2 \phi_a) + \mathbf{K}_a \phi_a = \mathbf{f}_a + \mathbf{Q}_{\text{source}}$$

In this case, $\mathbf{Q}_{\text{source}} = \mathbf{0}$ as there isn't any acoustic source in this section. Moreover,

$$\mathbf{f}_a^{(S)} = \int_S \gamma N_n dA = \int_S i\omega \mathbf{u}_S^{(S)} \cdot \mathbf{n} \cdot N_n dA$$

As a result, equation (29) then become

$$\begin{aligned}
\mathbf{M}_a^{(S)}(-\omega^2\phi_a^{(S)}) + \mathbf{K}_a^{(S)}\phi_a^{(S)} &= \int_S i\omega\mathbf{u}_S^{(S)} \cdot \mathbf{n} \cdot N_n dA \\
[-\omega^2\mathbf{M}_a^{(S)} + \mathbf{K}_a^{(S)}]\phi_a^{(S)} &= \int_S i\omega\mathbf{u}_S^{(S)} \cdot \mathbf{n} \cdot N_n dA \\
\phi_a^{(S)} &= [-\omega^2\mathbf{M}_a^{(S)} + \mathbf{K}_a^{(S)}]^{-1} \int_S i\omega\mathbf{u}_S^{(S)} \cdot \mathbf{n} \cdot N_n dA
\end{aligned} \tag{69}$$

Equation (69) is used to compute the acoustic velocity potential for the vibration due to the force excited vibration of the HDD stationary parts.

3.4. Rotating disk

HDD rotating disk is one of major rotational parts in the HDD. Its sound radiation characteristics can be examined analytically (Nickolas Vlahopoulos et al., 1999). In 1997, Shen's group reported the dynamic formulation of the rotating disk (Shen and Ku, 1997). This has been followed by many other researchers, e.g., Jiang (Jiang et al., 2002), Jintanawa(Jintanawan et al., 2001) and Yang (Yang and Chen, 2002). The same method is adapted in this analysis.

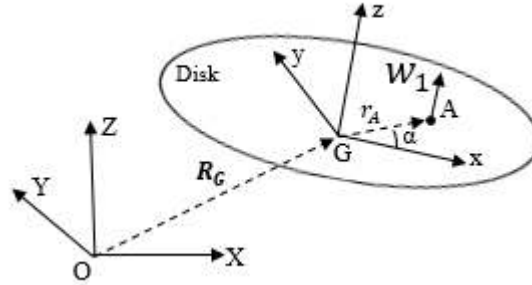


Figure 3-8 Model Disk spindle system

Let the fixed frame be XYZ and its unit vectors \hat{I}, \hat{J} and \hat{K} . The rocking frame on the disk spindle is the moving frame (xyz) and its unit vectors are \hat{i}, \hat{j} and \hat{k} . Point G is the CG point of the disk. Point A is any point on the disk. The displacement of point A during disk operation is $w_i \hat{k}$, where \hat{k} is the unit vector of the z axis. Hence, the equation of motion can be derived using Lagrange equation,

$$\mathbf{R}_{OA} = \mathbf{R}_G + \mathbf{r}_A + w_1 \hat{k}$$

in which \mathbf{R}_G can be written as

$$\mathbf{R}_G = R_X \hat{i} + R_Y \hat{j} + R_Z \hat{K}$$

and \mathbf{r}_A can be written as

$$\mathbf{r}_A = r_A \cos \alpha \hat{i} + r_A \sin \alpha \hat{j}$$

w_1 is the disk deformation, and it can be computed by the summation of a series of mode shapes

$$w_1 = \sum_{m=0}^{\infty} \sum_{n=-\infty}^{\infty} w_{mn}^{(D)}(r_A, \alpha) q_{mn}^{(D)}(t) \quad (70)$$

where, $w_{mn}^{(D)}(r_A, \alpha)$ is the disk mode shape with m is nodal circles and n is nodal diameter, and $w_{mn}^{(D)}(r_A, \alpha)$ can be computed by

$$w_{mn}^{(D)}(r_A, \alpha) = \begin{cases} R_{mn}^{(D)}(r) \cos(n\alpha), & n \geq 0 \\ R_{m,|n|}^{(D)}(r) \sin(|n|\alpha), & n < 0 \end{cases} \quad (71)$$

where, $R_{mn}^{(D)}$ is the complicated function in r .

The mode shape $w_{mn}^{(D)}(r_A, \alpha)$ are nominalized, thus

$$\int w_{mn}^{(D)}(r_A, \alpha) dm^{(D)} = \begin{cases} 0 & \text{if } n \neq 0 \\ I_1^{(D)} b_m^{(D)} & \text{if } n = 0 \end{cases} \quad (72)$$

where, $I_1^{(D)}$ is the mass moment of disk; and $b_m^{(D)}$ can be computer as

$$b_m^{(D)} = \frac{2\pi\rho^{(D)}h}{I_1^{(D)}} \int R_{m0}^{(D)}(r) dr$$

Here $\rho^{(D)}$ is the disk density, h is the thickness of the disk, and r is the radius of the disk.

Hence, the displacement of the point A on disk can be expressed as

$$\mathbf{R}^{(D)} = R_X \hat{i} + R_Y \hat{j} + R_Z \hat{K} + r_A \cos \alpha \hat{i} + r_A \sin \alpha \hat{j} + w_1 \hat{k} \quad (73)$$

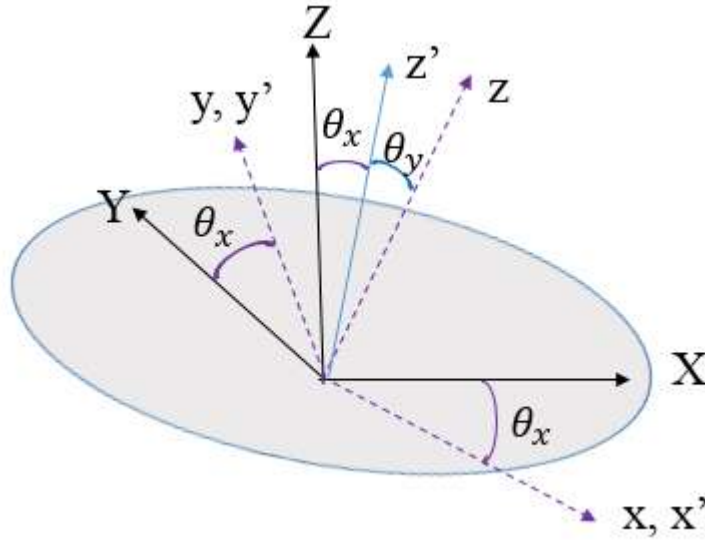


Figure 3-9 Rotation transformation between XYZ and xyz

The rotation matrix can be derived as

$$\begin{bmatrix} \hat{i} \\ \hat{j} \\ \hat{k} \end{bmatrix} = \begin{bmatrix} \cos \theta_y & -\sin \theta_x \sin \theta_y & \cos \theta_x \sin \theta_y \\ 0 & \cos \theta_x & \sin \theta_x \\ -\sin \theta_y & -\sin \theta_x \cos \theta_y & \cos \theta_x \cos \theta_y \end{bmatrix} \begin{bmatrix} \hat{I} \\ \hat{J} \\ \hat{K} \end{bmatrix}$$

In this thesis, HDD disk is made of glass. Therefore, θ_x and θ_y are very small, hence, the rotational matrix can be simplified as

$$\begin{bmatrix} \hat{i} \\ \hat{j} \\ \hat{k} \end{bmatrix} \approx \begin{bmatrix} 1 & 0 & \theta_y \\ 0 & 1 & \theta_x \\ -\theta_y & -\theta_x & 1 \end{bmatrix} \begin{bmatrix} \hat{I} \\ \hat{J} \\ \hat{K} \end{bmatrix} \quad (74)$$

Applying the rotational matrix to convert all parameters into the fixed frame gives

$$\begin{aligned} \mathbf{R}^{(D)} &= R_X \hat{I} + R_Y \hat{J} + R_Z \hat{K} + r_A \cos \alpha (\hat{I} + \theta_y \hat{K}) + r_A \sin \alpha (\hat{J} + \theta_x \hat{K}) + w_1 \hat{K} \\ \mathbf{R}^{(D)} &= (R_X + r_A \cos \alpha) \hat{I} + (R_Y + r_A \sin \alpha) \hat{J} + (R_Z + r_A \theta_y \cos \alpha + r_A \theta_x \sin \alpha + w_1) \hat{K} \end{aligned} \quad (75)$$

Hence, the equation (75) is the vector equation for the displacement when the disk is not rotating. For the HDD study in this analysis, the disk is rotating constantly with a speed of ω_3 .

As a result, the angular velocity $\omega^{(D)}$ of the rotating disk can be expressed as

$$\omega^{(D)} \approx \dot{\theta}_x \hat{i} + \dot{\theta}_y \hat{j} + \omega_3 \hat{k}$$

Hence, the rotating disk velocity can be written as

$$\dot{\mathbf{R}}^{(D)} = \dot{\mathbf{R}}_G + \omega^{(D)} \times \mathbf{r}_A + \dot{w}_1 \quad (76)$$

where,

$$\dot{\mathbf{R}}_G = \dot{R}_x \hat{i} + \dot{R}_y \hat{j} + \dot{R}_z \hat{k} \quad (77)$$

and

$$\omega^{(D)} \times \mathbf{r}_A = \begin{vmatrix} \hat{i} & \hat{j} & \hat{k} \\ \dot{\theta}_x & \dot{\theta}_y & \omega_3 \\ r_A \cos \alpha & r_A \sin \alpha & 0 \end{vmatrix} \quad (78)$$

$$\omega^{(D)} \times \mathbf{r}_A = -\omega_3 r_A \sin \alpha \hat{i} + \omega_3 r_A \cos \alpha \hat{j} + (\dot{\theta}_x r_A \sin \alpha - \dot{\theta}_y r_A \cos \alpha) \hat{k}$$

As the point A on the disk will rotate together in a speed of ω_3 , the angle α will be a function of time. Hence, the velocity of w_1 will consist of three parts, one is due to θ_x and θ_y , and the other is due to ω_3 and moreover due to the stationary disk deflection.

Thus

$$\dot{w}_1 = w_1(\dot{\theta}_y \hat{i} - \dot{\theta}_x \hat{j}) - n\omega_3 \sum_{m=0}^{\infty} \sum_{n=-\infty}^{\infty} w_{mn}^{(D)}(r_A, \alpha) q_{mn}^{(D)}(t) \hat{k} + \sum_{m=0}^{\infty} \sum_{n=-\infty}^{\infty} w_{mn}^{(D)}(r_A, \alpha) \dot{q}_{mn}^{(D)}(t) \hat{k} \quad (79)$$

$$\dot{w}_1 = w_1(\dot{\theta}_y \hat{i} - \dot{\theta}_x \hat{j}) + \sum_{m=0}^{\infty} \sum_{n=-\infty}^{\infty} w_{mn}^{(D)}(r_A, \alpha) [\dot{q}_{mn}^{(D)}(t) + n\omega_3 q_{m,-n}^{(D)}(t)] \hat{k}$$

Therefore, the kinetic energy of the rotating disk is

$$T^{(D)} = \frac{1}{2} \int \dot{\mathbf{R}}^{(D)} \cdot \dot{\mathbf{R}}^{(D)} dm^{(D)}$$

$$T^{(D)} = \frac{1}{2} \int (\dot{\mathbf{R}}_G + \omega^{(D)} \times \mathbf{r}_A + \dot{w}_1) \cdot (\dot{\mathbf{R}}_G + \omega^{(D)} \times \mathbf{r}_A + \dot{w}_1) dm^{(D)}$$

$$T^{(D)} = \frac{1}{2} \left[\int \dot{\mathbf{R}}_G \cdot \dot{\mathbf{R}}_G dm^{(D)} + \int (\omega^{(D)} \times \mathbf{r}_A) (\omega^{(D)} \times \mathbf{r}_A) dm^{(D)} + \int \dot{w}_1 \cdot \dot{w}_1 dm^{(D)} \right. \quad (80)$$

$$\left. + 2 \int \dot{\mathbf{R}}_G \cdot (\omega^{(D)} \times \mathbf{r}_A) dm^{(D)} + 2 \int \dot{\mathbf{R}}_G \cdot \dot{w}_1 dm^{(D)} + 2 \int \dot{w}_1 (\omega^{(D)} \times \mathbf{r}_A) dm^{(D)} \right]$$

The equation (80) is now simplified term by term:

First term:

$$\frac{1}{2} \int \dot{\mathbf{R}}_G \cdot \dot{\mathbf{R}}_G dm^{(D)} = \frac{1}{2} m^{(D)} (\dot{R}_x^2 + \dot{R}_y^2 + \dot{R}_z^2) \quad (81)$$

Second term:

$$\frac{1}{2} \int (\omega^{(D)} \times \mathbf{r}_A) (\omega^{(D)} \times \mathbf{r}_A) dm^{(D)} = \frac{1}{2} \omega^{(D)} \cdot I^{(D)} \cdot \omega^{(D)}$$

$$= \begin{bmatrix} \dot{\theta}_y \\ \dot{\theta}_x \\ \omega_3 \end{bmatrix} \begin{bmatrix} I_1^{(D)} & 0 & 0 \\ 0 & I_1^{(D)} & 0 \\ 0 & 0 & I_3^{(D)} \end{bmatrix} \begin{bmatrix} \dot{\theta}_y \\ \dot{\theta}_x \\ \omega_3 \end{bmatrix} = \frac{1}{2} I_1^{(D)} (\dot{\theta}_x^2 + \dot{\theta}_y^2) + \frac{1}{2} I_3^{(D)} \omega_3^2 \quad (82)$$

Where, $I_1^{(D)}$ and $I_3^{(D)}$ are the mass moment of inertial of the disk.

The third term:

$$\begin{aligned} & \frac{1}{2} \int \dot{\mathbf{w}}_1 \cdot \dot{\mathbf{w}}_1 dm^{(D)} \\ &= \frac{1}{2} \int \left\{ w_1 (\dot{\theta}_y \hat{i} - \dot{\theta}_x \hat{j}) \right. \\ &+ \sum_{m=0}^{\infty} \sum_{n=-\infty}^{\infty} w_{mn}^{(D)}(r_A, \alpha) \left[\dot{q}_{mn}^{(D)}(t) + n\omega_3 q_{m,-n}^{(D)}(t) \right] \hat{k} \left. \right\} \left\{ w_1 (\dot{\theta}_y \hat{i} - \dot{\theta}_x \hat{j}) \right. \\ &+ \sum_{m=0}^{\infty} \sum_{n=-\infty}^{\infty} w_{mn}^{(D)}(r_A, \alpha) \left[\dot{q}_{mn}^{(D)}(t) + n\omega_3 q_{m,-n}^{(D)}(t) \right] \hat{k} \left. \right\} dm^{(D)} \end{aligned}$$

For unit vector multiplication,

$$\hat{i}\hat{j} = \hat{j}\hat{k} = \hat{k}\hat{i} = 0 \text{ \& } \hat{i}\hat{i} = \hat{j}\hat{j} = \hat{k}\hat{k} = 1$$

Hence,

$$\begin{aligned} & \frac{1}{2} \int \dot{\mathbf{w}}_1 \cdot \dot{\mathbf{w}}_1 dm^{(D)} \\ &= \frac{1}{2} \int \left\{ w_1 \dot{\theta}_y^2 - w_1 \dot{\theta}_x^2 \right. \\ &+ \left. \left[\sum_{m=0}^{\infty} \sum_{n=-\infty}^{\infty} w_{mn}^{(D)}(r_A, \alpha) \left[\dot{q}_{mn}^{(D)}(t) + n\omega_3 q_{m,-n}^{(D)}(t) \right] \right]^2 \right\} dm^{(D)} \\ &= \frac{1}{2} \int w_1 (\dot{\theta}_y^2 - \dot{\theta}_x^2) dm^{(D)} \\ &+ \frac{1}{2} \int \sum_{m=0}^{\infty} \sum_{n=-\infty}^{\infty} w_{mn}^{(D)}(r_A, \alpha) \left[\dot{q}_{mn}^{(D)}(t) + n\omega_3 q_{m,-n}^{(D)}(t) \right] dm^{(D)} \\ &= \frac{1}{2} (\dot{\theta}_y^2 - \dot{\theta}_x^2) \int w_1 dm^{(D)} \\ &+ \frac{1}{2} \int \sum_{m=0}^{\infty} \sum_{n=-\infty}^{\infty} \left[w_{mn}^{(D)}(r_A, \alpha) \right]^2 \left[\dot{q}_{mn}^{(D)}(t) + n\omega_3 q_{m,-n}^{(D)}(t) \right]^2 dm^{(D)} \end{aligned}$$

As $w_{mn}^{(D)}(r_A, \alpha)$ satisfies orthogonality,

$$\int w_{mn}^{(D)}(r_A, \alpha) w_{pq}^{(D)}(r_A, \alpha) dm^{(D)} = I_1^{(D)} \delta_{mn} \delta_{pq}$$

Therefore,

$$\frac{1}{2} \int \dot{\mathbf{w}}_1 \cdot \dot{\mathbf{w}}_1 dm^{(D)} = \frac{1}{2} (\dot{\theta}_y^2 - \dot{\theta}_x^2) I_1^{(D)} b_m^{(D)} + \frac{1}{2} \sum_{m=0}^{\infty} \sum_{n=-\infty}^{\infty} I_1^{(D)} \left[\dot{q}_{mn}^{(D)}(t) + n\omega_3 q_{m,-n}^{(D)}(t) \right]^2 \quad (83)$$

The fourth term:

$$\begin{aligned} & \int \dot{\mathbf{R}}_G \cdot (\omega^{(D)} \times \mathbf{r}_A) dm^{(D)} \\ &= \int (\dot{R}_X \hat{I} + \dot{R}_Y \hat{J} + \dot{R}_Z \hat{K}) \\ & \quad \cdot [-\omega_3 r_A \sin \alpha \hat{i} + \omega_3 r_A \cos \alpha \hat{j} + (\dot{\theta}_x r_A \sin \alpha - \dot{\theta}_y r_A \cos \alpha) \hat{k}] dm^{(D)} \end{aligned}$$

Apply rotational matrix,

$$\begin{aligned} & \int \dot{\mathbf{R}}_G \cdot (\omega^{(D)} \times \mathbf{r}_A) dm^{(D)} \\ &= (\dot{R}_X \hat{I} + \dot{R}_Y \hat{J} + \dot{R}_Z \hat{K}) \\ & \quad \cdot \left[-\omega_3 r_A \sin \alpha (\hat{I} + \theta_y^{(A)} \hat{J}) + \omega_3 r_A \cos \alpha (\hat{J} + \theta_x^{(A)} \hat{K}) + (\dot{\theta}_x r_A \sin \alpha \right. \\ & \quad \left. - \dot{\theta}_y r_A \cos \alpha) (-\theta_y^{(A)} \hat{I} - \theta_x^{(A)} \hat{J} + \hat{K}) \right] \int dm^{(D)} \\ &= m^{(D)} (\dot{R}_X \hat{I} + \dot{R}_Y \hat{J} + \dot{R}_Z \hat{K}) \\ & \quad \cdot \left[-\omega_3 r_A \sin \alpha (\hat{I} + \theta_y^{(A)} \hat{J}) + \omega_3 r_A \cos \alpha (\hat{J} + \theta_x^{(A)} \hat{K}) + (\dot{\theta}_x r_A \sin \alpha \right. \\ & \quad \left. - \dot{\theta}_y r_A \cos \alpha) (-\theta_y^{(A)} \hat{I} - \theta_x^{(A)} \hat{J} + \hat{K}) \right] \end{aligned}$$

The result of term 4 will be higher 2nd order, hence, it was assumed to be zero.

$$\int \dot{\mathbf{R}}_G \cdot (\omega^{(D)} \times \mathbf{r}_A) dm^{(D)} = 0$$

The fifth term:

$$\begin{aligned} & \int \dot{\mathbf{R}}_G \cdot \dot{\mathbf{w}}_1 dm^{(D)} = (\dot{R}_X \hat{I} + \dot{R}_Y \hat{J} + \dot{R}_Z \hat{K}) \int \dot{\mathbf{w}}_1 dm^{(D)} \\ &= (\dot{R}_X \hat{I} + \dot{R}_Y \hat{J} + \dot{R}_Z \hat{K}) \int \left\{ w_1 (\dot{\theta}_y \hat{i} - \dot{\theta}_x \hat{j}) \right. \\ & \quad \left. + \sum_{m=0}^{\infty} \sum_{n=-\infty}^{\infty} w_{mn}^{(D)}(r_A, \alpha) \left[\dot{q}_{mn}^{(D)}(t) + n\omega_3 q_{m,-n}^{(D)}(t) \right] \hat{k} \right\} dm^{(D)} \\ &= (\dot{R}_X \hat{I} + \dot{R}_Y \hat{J} + \dot{R}_Z \hat{K}) \left\{ (\dot{\theta}_y \hat{i} - \dot{\theta}_x \hat{j}) \int w_1 dm^{(D)} \right. \\ & \quad \left. + \sum_{m=0}^{\infty} \sum_{n=-\infty}^{\infty} \left[\dot{q}_{mn}^{(D)}(t) + n\omega_3 q_{m,-n}^{(D)}(t) \right] \hat{k} \int w_{mn}^{(D)}(r_A, \alpha) dm^{(D)} \right\} \quad (84) \end{aligned}$$

Apply equation (70) and (72) to (84), and only Z direction vibration discussed in this, thus

$$\begin{aligned}
& \int \dot{\mathbf{R}}_G \cdot \dot{\mathbf{w}}_1 dm^{(D)} \\
&= (\dot{R}_X \hat{I} + \dot{R}_Y \hat{J} + \dot{R}_Z \hat{K}) \left\{ [\dot{\theta}_y (\hat{I} + \theta_y \hat{J}) - \dot{\theta}_x (\hat{J} + \theta_x \hat{K})] I_1^{(D)} b_m^{(D)} + (-\theta_y \hat{I} - \theta_x \hat{J} \right. \\
&\quad \left. + \hat{K}) \sum_{m=0}^{\infty} \sum_{n=-\infty}^{\infty} I_1^{(D)} b_m^{(D)} [\dot{q}_{mn}^{(D)}(t) + n\omega_3 q_{m,-n}^{(D)}(t)] \right\}
\end{aligned}$$

Further simplifying the term in the curly bracket, it becomes

$$\begin{aligned}
& [\dot{\theta}_y (\hat{I} + \theta_y \hat{J}) - \dot{\theta}_x (\hat{J} + \theta_x \hat{K})] I_1^{(D)} b_m^{(D)} \\
&\quad + (-\theta_y \hat{I} - \theta_x \hat{J} + \hat{K}) \sum_{m=0}^{\infty} I_1^{(D)} b_m^{(D)} [\dot{q}_{mn}^{(D)}(t) + n\omega_3 q_{m,-n}^{(D)}(t)] \\
&= \sum_{m=0}^{\infty} I_1^{(D)} b_m^{(D)} \left\{ \dot{\theta}_y \hat{I} + \theta_y \dot{\theta}_y \hat{J} - \dot{\theta}_x \hat{J} + \theta_x \dot{\theta}_x \hat{K} - \theta_y [\dot{q}_{mn}^{(D)}(t) + n\omega_3 q_{m,-n}^{(D)}(t)] \hat{I} \right. \\
&\quad \left. - \theta_x [\dot{q}_{mn}^{(D)}(t) + n\omega_3 q_{m,-n}^{(D)}(t)] \hat{J} + [\dot{q}_{mn}^{(D)}(t) + n\omega_3 q_{m,-n}^{(D)}(t)] \hat{K} \right\} \\
&= \sum_{m=0}^{\infty} I_1^{(D)} b_m^{(D)} \left\{ \left\{ \dot{\theta}_y - \theta_y [\dot{q}_{mn}^{(D)}(t) + n\omega_3 q_{m,-n}^{(D)}(t)] \right\} \hat{I} \right. \\
&\quad \left. + \left\{ \theta_y \dot{\theta}_y - \dot{\theta}_x - \theta_x [\dot{q}_{mn}^{(D)}(t) + n\omega_3 q_{m,-n}^{(D)}(t)] \right\} \hat{J} \right. \\
&\quad \left. + \left\{ \theta_x \dot{\theta}_x + [\dot{q}_{mn}^{(D)}(t) + n\omega_3 q_{m,-n}^{(D)}(t)] \right\} \hat{K} \right\}
\end{aligned}$$

Since, the unit vector multiplication has a property as

$$\hat{I}\hat{J} = \hat{J}\hat{K} = \hat{K}\hat{I} = 0 \text{ \& } \hat{I}\hat{I} = \hat{J}\hat{J} = \hat{K}\hat{K} = 1$$

as a result

$$\begin{aligned}
& \int \dot{\mathbf{R}}_G \cdot \dot{\mathbf{w}}_1 dm^{(D)} \\
&= (\dot{R}_X \hat{I} + \dot{R}_Y \hat{J} + \dot{R}_Z \hat{K}) \sum_{m=0}^{\infty} I_1^{(D)} b_m^{(D)} \left\{ \left\{ \dot{\theta}_y - \theta_y [\dot{q}_{mn}^{(D)}(t) + n\omega_3 q_{m,-n}^{(D)}(t)] \right\} \hat{I} \right. \\
&\quad \left. + \left\{ \theta_y \dot{\theta}_y - \dot{\theta}_x - \theta_x [\dot{q}_{mn}^{(D)}(t) + n\omega_3 q_{m,-n}^{(D)}(t)] \right\} \hat{J} \right. \\
&\quad \left. + \left\{ \theta_x \dot{\theta}_x + [\dot{q}_{mn}^{(D)}(t) + n\omega_3 q_{m,-n}^{(D)}(t)] \right\} \hat{K} \right\} \\
&= \sum_{m=0}^{\infty} I_1^{(D)} b_m^{(D)} \left\{ \left\{ \dot{\theta}_y - \theta_y [\dot{q}_{mn}^{(D)}(t) + n\omega_3 q_{m,-n}^{(D)}(t)] \right\} \dot{R}_X \right. \\
&\quad \left. + \left\{ \theta_y \dot{\theta}_y - \dot{\theta}_x - \theta_x [\dot{q}_{mn}^{(D)}(t) + n\omega_3 q_{m,-n}^{(D)}(t)] \right\} \dot{R}_Y \right. \\
&\quad \left. + \left\{ \theta_x \dot{\theta}_x + [\dot{q}_{mn}^{(D)}(t) + n\omega_3 q_{m,-n}^{(D)}(t)] \right\} \dot{R}_Z \right\}
\end{aligned}$$

To simplify further, the higher order (2nd order and above) will be dropped off. Hence,

$$\int \dot{\mathbf{R}}_G \cdot \dot{\mathbf{w}}_1 dm^{(D)} \approx \dot{R}_Z \sum_{m=0}^{\infty} I_1^{(D)} b_m^{(D)} \left[\dot{q}_{mn}^{(D)}(t) + n\omega_3 q_{m,-n}^{(D)}(t) \right] \quad (85)$$

The sixth term

$$\begin{aligned} & \int \dot{\mathbf{w}}_1 (\boldsymbol{\omega}^{(D)} \times \mathbf{r}_A) dm^{(D)} \\ &= \int \left[-\omega_3 r_A \sin \alpha \hat{i} + \omega_3 r_A \cos \alpha \hat{j} + (\dot{\theta}_x r_A \sin \alpha - \dot{\theta}_y r_A \cos \alpha) \hat{k} \right] \left\{ w_1 (\dot{\theta}_y \hat{i} \right. \\ & \quad \left. - \dot{\theta}_x \hat{j}) + \sum_{m=0}^{\infty} \sum_{n=-\infty}^{\infty} w_{mn}^{(D)}(r_A, \alpha) \left[\dot{q}_{mn}^{(D)}(t) + n\omega_3 q_{m,-n}^{(D)}(t) \right] \hat{k} \right\} dm^{(D)} \\ &= \int w_1 \dot{\theta}_y (-\omega_3 r_A \sin \alpha) dm^{(D)} + \int (-w_1 \dot{\theta}_x) (\omega_3 r_A \cos \alpha) dm^{(D)} \\ & \quad + \int \left\{ (\dot{\theta}_x r_A \sin \alpha \right. \\ & \quad \left. - \dot{\theta}_y r_A \cos \alpha) \sum_{m=0}^{\infty} \sum_{n=-\infty}^{\infty} w_{mn}^{(D)}(r_A, \alpha) \left[\dot{q}_{mn}^{(D)}(t) + n\omega_3 q_{m,-n}^{(D)}(t) \right] \right\} dm^{(D)} \end{aligned}$$

Since mass of the disk can be computed by

$$m^{(D)} = \rho^{(D)} (\text{Volume})^{(D)} = \rho^{(D)} \pi r^2 h^{(D)}$$

where $h^{(D)}$ is the disk thickness.

$$dm^{(D)} = \rho^{(D)} \pi h^{(D)} r_A dr d\alpha$$

As a result, the term $\int w_1 r_A \sin \alpha dm^{(D)}$ can be expressed as

$$\int w_1 r_A \sin \alpha dm^{(D)} = \int w_1 r_A \sin \alpha \rho^{(D)} \pi h^{(D)} r_A dr d\alpha \quad (86)$$

Substitute equation (68) and (69) into (84) and set $|n| = 1$

$$\int w_1 r_A \sin \alpha dm^{(D)} = \rho^{(D)} \pi h^{(D)} \int R_{m,1}^{(D)}(r) \sin \alpha r_A^2 dr d\alpha \quad (87)$$

Define $a_m^{(D)}$ in order to simplify the equation above.

$$a_m^{(D)} = \frac{\rho^{(D)} \pi h^{(D)}}{I_1^{(D)}} \int R_{m,1}^{(D)}(r) \sin \alpha r_A^2 dr d\alpha$$

Thus, equation (85) can be then simplified as

$$\int w_1 r_A \sin \alpha dm^{(D)} = I_1^{(D)} a_m^{(D)}$$

Hence, the sixth term can be expressed as

$$\begin{aligned} & \int \dot{\mathbf{w}}_1(\omega^{(D)} \times \mathbf{r}_A) dm^{(D)} \\ &= \sum_{m=0}^{\infty} \dot{\theta}_x I_1^{(D)} a_m^{(D)} \left[\dot{q}_{m,-1}^{(D)}(t) + n\omega_3 q_{m,1}^{(D)}(t) \right] \\ & - \sum_{m=0}^{\infty} \dot{\theta}_y I_1^{(D)} a_m^{(D)} \left[\dot{q}_{m,1}^{(D)}(t) + n\omega_3 q_{m,-1}^{(D)}(t) \right] - \omega_3 \sum_{m=0}^{\infty} \dot{\theta}_y I_1^{(D)} a_m^{(D)} \dot{q}_{m,-1}^{(D)}(t) \\ & - \omega_3 \sum_{m=0}^{\infty} \dot{\theta}_x I_1^{(D)} a_m^{(D)} \dot{q}_{m,1}^{(D)}(t) \end{aligned} \quad (88)$$

The potential energy of the rotating disk can be written as

$$V^{(D)} = \frac{1}{2} I x^2 = \frac{1}{2} I_1^{(D)} \sum_{m=0}^{\infty} \sum_{n=-\infty}^{\infty} \left[w_{mn}^{(D)}(r_A, \alpha) q_{mn}^{(D)}(t) \right]^2 \quad (89)$$

Recall question (46) & (47)

$$\frac{d}{dt} \left(\frac{\partial L}{\partial \dot{q}} \right) - \frac{\partial L}{\partial q} = Q \text{ and } L = T - V$$

Now, apply this to obtain equation of motion for the rotating disk. Using equation (81), (82), (83), (85), (88), (89) to form Langrage equation.

$$\begin{aligned} & L^{(D)} = T^{(D)} - V^{(D)} \\ & L^{(D)} = \frac{1}{2} m^{(D)} (\dot{R}_x^2 + \dot{R}_y^2 + \dot{R}_z^2) + \frac{1}{2} I_1^{(D)} (\dot{\theta}_x^2 + \dot{\theta}_y^2) + \frac{1}{2} I_3^{(D)} \omega_3^2 + \frac{1}{2} (\dot{\theta}_y^2 - \dot{\theta}_x^2) I_1^{(D)} b_m^{(D)} \\ & + \frac{1}{2} \sum_{m=0}^{\infty} \sum_{n=-\infty}^{\infty} I_1^{(D)} \left[\dot{q}_{mn}^{(D)}(t) + n\omega_3 q_{m,-n}^{(D)}(t) \right]^2 \\ & + \dot{R}_z \sum_{m=0}^{\infty} I_1^{(D)} b_m^{(D)} \left[\dot{q}_{m,0}^{(D)}(t) + n\omega_3 q_{m,0}^{(D)}(t) \right] \\ & + \sum_{m=0}^{\infty} \dot{\theta}_x I_1^{(D)} a_m^{(D)} \left[\dot{q}_{m,-1}^{(D)}(t) + n\omega_3 q_{m,1}^{(D)}(t) \right] \\ & - \sum_{m=0}^{\infty} \dot{\theta}_y I_1^{(D)} a_m^{(D)} \left[\dot{q}_{m,1}^{(D)}(t) + n\omega_3 q_{m,-1}^{(D)}(t) \right] - \omega_3 \sum_{m=0}^{\infty} \dot{\theta}_y I_1^{(D)} a_m^{(D)} \dot{q}_{m,-1}^{(D)}(t) \\ & - \omega_3 \sum_{m=0}^{\infty} \dot{\theta}_x I_1^{(D)} a_m^{(D)} \dot{q}_{m,1}^{(D)}(t) - \frac{1}{2} I_1^{(D)} \sum_{m=0}^{\infty} \sum_{n=-\infty}^{\infty} \left[w_{mn}^{(D)}(r_A, \alpha) q_{mn}^{(D)}(t) \right]^2 \end{aligned} \quad (90)$$

Hence,

$$\begin{aligned}
\frac{\partial L}{\partial \dot{q}} = & m^{(D)}(\dot{R}_X + \dot{R}_Y + \dot{R}_Z) + I_1^{(D)}(\dot{\theta}_x + \dot{\theta}_y) + (\dot{\theta}_y - \dot{\theta}_x)I_1^{(D)}b_m^{(D)} \\
& + \sum_{m=0}^{\infty} \sum_{n=-\infty}^{\infty} I_1^{(D)} [\dot{q}_{mn}^{(D)}(t) + n\omega_3 q_{m,-n}^{(D)}(t)] + \dot{R}_Z \sum_{m=0}^{\infty} I_1^{(D)} b_m^{(D)} \\
& + \sum_{m=0}^{\infty} I_1^{(D)} b_m^{(D)} [\dot{q}_{m,0}^{(D)}(t) + n\omega_3 q_{m,0}^{(D)}(t)] + \sum_{m=0}^{\infty} \dot{\theta}_x I_1^{(D)} a_m^{(D)} \\
& + \sum_{m=0}^{\infty} I_1^{(D)} a_m^{(D)} [\dot{q}_{m,-1}^{(D)}(t) + n\omega_3 q_{m,1}^{(D)}(t)] + \sum_{m=0}^{\infty} \dot{\theta}_y I_1^{(D)} a_m^{(D)} \\
& - \sum_{m=0}^{\infty} I_1^{(D)} a_m^{(D)} [\dot{q}_{m,1}^{(D)}(t) + n\omega_3 q_{m,-1}^{(D)}(t)] - \omega_3 \sum_{m=0}^{\infty} \dot{\theta}_y I_1^{(D)} a_m^{(D)} \\
& - \omega_3 \sum_{m=0}^{\infty} I_1^{(D)} a_m^{(D)} \dot{q}_{m,-1}^{(D)}(t) - \omega_3 \sum_{m=0}^{\infty} \dot{\theta}_x I_1^{(D)} a_m^{(D)} - \omega_3 \sum_{m=0}^{\infty} I_1^{(D)} a_m^{(D)} \dot{q}_{m,1}^{(D)}(t)
\end{aligned}$$

Thus

$$\begin{aligned}
\frac{d}{dt} \left(\frac{\partial L}{\partial \dot{q}} \right) = & m^{(D)}(\ddot{R}_X + \ddot{R}_Y + \ddot{R}_Z) + I_1^{(D)}(\ddot{\theta}_x + \ddot{\theta}_y) + (\ddot{\theta}_y - \ddot{\theta}_x)I_1^{(D)}b_m^{(D)} \\
& + \sum_{m=0}^{\infty} \sum_{n=-\infty}^{\infty} I_1^{(D)} [\ddot{q}_{mn}^{(D)}(t) + n\omega_3 \dot{q}_{m,-n}^{(D)}(t)] + \ddot{R}_Z \sum_{m=0}^{\infty} I_1^{(D)} b_m^{(D)} \\
& + \sum_{m=0}^{\infty} I_1^{(D)} b_m^{(D)} [\ddot{q}_{m,0}^{(D)}(t) + n\omega_3 \dot{q}_{m,0}^{(D)}(t)] + \sum_{m=0}^{\infty} \ddot{\theta}_x I_1^{(D)} a_m^{(D)} \\
& + \sum_{m=0}^{\infty} I_1^{(D)} a_m^{(D)} [\ddot{q}_{m,-1}^{(D)}(t) + n\omega_3 \dot{q}_{m,1}^{(D)}(t)] + \sum_{m=0}^{\infty} \ddot{\theta}_y I_1^{(D)} a_m^{(D)} \\
& - \sum_{m=0}^{\infty} I_1^{(D)} a_m^{(D)} [\ddot{q}_{m,1}^{(D)}(t) + n\omega_3 \dot{q}_{m,-1}^{(D)}(t)] - \omega_3 \sum_{m=0}^{\infty} \ddot{\theta}_y I_1^{(D)} a_m^{(D)} \\
& - \omega_3 \sum_{m=0}^{\infty} I_1^{(D)} a_m^{(D)} \ddot{q}_{m,-1}^{(D)}(t) - \omega_3 \sum_{m=0}^{\infty} \ddot{\theta}_x I_1^{(D)} a_m^{(D)} - \omega_3 \sum_{m=0}^{\infty} I_1^{(D)} a_m^{(D)} \ddot{q}_{m,1}^{(D)}(t)
\end{aligned} \tag{91}$$

And

$$\begin{aligned}
\frac{\partial L}{\partial q} = & \sum_{m=0}^{\infty} \sum_{n=-\infty}^{\infty} I_1^{(D)} [\dot{q}_{mn}^{(D)}(t) + n\omega_3 q_{m,-n}^{(D)}(t)] + \dot{R}_Z \sum_{m=0}^{\infty} I_1^{(D)} b_m^{(D)} + \sum_{m=0}^{\infty} \dot{\theta}_x I_1^{(D)} a_m^{(D)} \\
& - \sum_{m=0}^{\infty} \dot{\theta}_y I_1^{(D)} a_m^{(D)} - I_1^{(D)} \sum_{m=0}^{\infty} \sum_{n=-\infty}^{\infty} w_{mn}^{(D)}(r_A, \alpha) q_{mn}^{(D)}(t)
\end{aligned} \tag{92}$$

Therefore, the left side of the Langrage equation can be obtained by combining (91) and (92)

$$\begin{aligned}
\frac{d}{dt} \left(\frac{\partial L}{\partial \dot{q}} \right) - \frac{\partial L}{\partial q} &= m^{(D)} (\ddot{R}_X + \ddot{R}_Y + \ddot{R}_Z) + I_1^{(D)} (\ddot{\theta}_x + \ddot{\theta}_y) + (\dot{\theta}_y - \dot{\theta}_x) I_1^{(D)} b_m^{(D)} \\
&+ \sum_{m=0}^{\infty} \sum_{n=-\infty}^{\infty} I_1^{(D)} \left[\ddot{q}_{mn}^{(D)}(t) + n\omega_3 \dot{q}_{m,-n}^{(D)}(t) \right] + \ddot{R}_Z \sum_{m=0}^{\infty} I_1^{(D)} b_m^{(D)} \\
&+ \sum_{m=0}^{\infty} I_1^{(D)} b_m^{(D)} \left[\ddot{q}_{m,0}^{(D)}(t) + n\omega_3 \dot{q}_{m,0}^{(D)}(t) \right] + \sum_{m=0}^{\infty} \ddot{\theta}_x I_1^{(D)} a_m^{(D)} \\
&+ \sum_{m=0}^{\infty} I_1^{(D)} a_m^{(D)} \left[\ddot{q}_{m,-1}^{(D)}(t) + n\omega_3 \dot{q}_{m,1}^{(D)}(t) \right] + \sum_{m=0}^{\infty} \ddot{\theta}_y I_1^{(D)} a_m^{(D)} \\
&- \sum_{m=0}^{\infty} I_1^{(D)} a_m^{(D)} \left[\ddot{q}_{m,1}^{(D)}(t) + n\omega_3 \dot{q}_{m,-1}^{(D)}(t) \right] - \omega_3 \sum_{m=0}^{\infty} \ddot{\theta}_y I_1^{(D)} a_m^{(D)} \\
&- \omega_3 \sum_{m=0}^{\infty} I_1^{(D)} a_m^{(D)} \ddot{q}_{m,-1}^{(D)}(t) - \omega_3 \sum_{m=0}^{\infty} \ddot{\theta}_x I_1^{(D)} a_m^{(D)} - \omega_3 \sum_{m=0}^{\infty} I_1^{(D)} a_m^{(D)} \ddot{q}_{m,1}^{(D)}(t) \\
&- \sum_{m=0}^{\infty} \sum_{n=-\infty}^{\infty} I_1^{(D)} \left[\dot{q}_{mn}^{(D)}(t) + n\omega_3 q_{m,-n}^{(D)}(t) \right] - \dot{R}_Z \sum_{m=0}^{\infty} I_1^{(D)} b_m^{(D)} \\
&- \sum_{m=0}^{\infty} \dot{\theta}_x I_1^{(D)} a_m^{(D)} + \sum_{m=0}^{\infty} \dot{\theta}_y I_1^{(D)} a_m^{(D)} + I_1^{(D)} \sum_{m=0}^{\infty} \sum_{n=-\infty}^{\infty} w_{mn}^{(D)}(r_A, \alpha) q_{mn}^{(D)}(t)
\end{aligned}$$

Rearrange it gives

$$\begin{aligned}
\frac{d}{dt} \left(\frac{\partial L}{\partial \dot{q}} \right) - \frac{\partial L}{\partial q} = & \left\{ m^{(D)} \ddot{R}_x + m^{(D)} \ddot{R}_y + \left(m^{(D)} + \sum_{m=0}^{\infty} I_1^{(D)} b_m^{(D)} \right) \ddot{R}_z \right. \\
& + \left[I_1^{(D)} - I_1^{(D)} b_m^{(D)} + \sum_{m=0}^{\infty} \left(I_1^{(D)} a_m^{(D)} - \omega_3 I_1^{(D)} a_m^{(D)} \right) \right] \ddot{\theta}_x \\
& + \left[I_1^{(D)} + I_1^{(D)} b_m^{(D)} + \sum_{m=0}^{\infty} \left(I_1^{(D)} a_m^{(D)} - \omega_3 I_1^{(D)} a_m^{(D)} \right) \right] \ddot{\theta}_y \\
& + \left[\sum_{m=0}^{\infty} I_1^{(D)} a_m^{(D)} - \omega_3 \sum_{m=0}^{\infty} I_1^{(D)} a_m^{(D)} \right] \ddot{q}_{m,-1}(t) + \sum_{m=0}^{\infty} I_1^{(D)} b_m^{(D)} \ddot{q}_{m,0}(t) \\
& + \left[n\omega_3 \sum_{m=0}^{\infty} I_1^{(D)} a_m^{(D)} - \omega_3 \sum_{m=0}^{\infty} I_1^{(D)} a_m^{(D)} \right] \ddot{q}_{m,1}(t) + \sum_{m=0}^{\infty} \sum_{n=-\infty}^{\infty} I_1^{(D)} \ddot{q}_{mn}(t) \left. \right\} \quad (93) \\
& + \left\{ \left[\sum_{m=0}^{\infty} I_1^{(D)} b_m^{(D)} \right] \dot{R}_z + \left[- \sum_{m=0}^{\infty} I_1^{(D)} a_m^{(D)} \right] \dot{\theta}_x + \left[\sum_{m=0}^{\infty} I_1^{(D)} a_m^{(D)} \right] \dot{\theta}_y \right. \\
& + n\omega_3 \sum_{m=0}^{\infty} \sum_{n=-\infty}^{\infty} I_1^{(D)} \dot{q}_{m,-n}(t) - n\omega_3 \sum_{m=0}^{\infty} I_1^{(D)} a_m^{(D)} \dot{q}_{m,-1}(t) \\
& + n\omega_3 \sum_{m=0}^{\infty} I_1^{(D)} b_m^{(D)} \dot{q}_{m,0}(t) \\
& + n\omega_3 \sum_{m=0}^{\infty} I_1^{(D)} a_m^{(D)} \dot{q}_{m,1}(t) - \sum_{m=0}^{\infty} \sum_{n=-\infty}^{\infty} I_1^{(D)} \dot{q}_{mn}(t) \left. \right\} \\
& + \left\{ -n\omega_3 \sum_{m=0}^{\infty} \sum_{n=-\infty}^{\infty} I_1^{(D)} q_{m,-n}(t) + I_1^{(D)} \sum_{m=0}^{\infty} \sum_{n=-\infty}^{\infty} w_{mn}^{(D)}(r_A, \alpha) q_{mn}(t) \right\}
\end{aligned}$$

From the above equations, the general displacement and the corresponding general force can be identified as,

$$\mathbf{q}^{(D)} = \begin{bmatrix} R_x \\ R_y \\ R_z \\ \theta_x \\ \theta_y \\ q_{m,-n} \\ q_{m,-1} \\ q_{m,0} \\ q_{m,1} \\ q_{mn} \end{bmatrix} \text{ and } \mathbf{Q}^{(D)} = \begin{bmatrix} F_x \\ F_y \\ F_z \\ M_x \\ M_y \\ Q_{m,-n} \\ Q_{m,-1} \\ Q_{m,0} \\ Q_{m,1} \\ Q_{mn} \end{bmatrix}$$

Therefore, the motion of equation for the rotating disk can be formed as,

$$\mathbf{M}^{(D)} \ddot{\mathbf{q}}^{(D)} + \mathbf{C}^{(D)} \dot{\mathbf{q}}^{(D)} + \mathbf{K}^{(D)} \mathbf{q}^{(D)} = \mathbf{Q}^{(D)} \quad (94)$$

Where, $\mathbf{M}^{(D)}$ is mass matrix; $\mathbf{C}^{(D)}$ is damping matrix; $\mathbf{K}^{(D)}$ is stiffness matrix;

Apply the same procedure as in previous section i.e. equation (55) to (69), the term $\phi^{(D)}$ can be computed by

$$\phi_a^{(D)} = \left[-\omega^2 \mathbf{M}_a^{(D)} + \mathbf{K}_a^{(D)} \right]^{-1} \int_S i\omega \mathbf{q}_S^{(D)} \cdot \mathbf{n} \cdot N_n dA \quad (95)$$

where $\mathbf{q}_S^{(D)}$ can be calculated through

$$\mathbf{q}_S^{(D)} = \left[-\omega^2 \mathbf{M}_S^{(D)} + i\omega \mathbf{C}_S^{(D)} + \mathbf{K}_S^{(D)} \right]^{-1} \mathbf{Q}_S^{(D)} \quad (96)$$

where, $\mathbf{q}_S^{(D)} \equiv \mathbf{q}^{(D)}$ and $\mathbf{Q}_S^{(D)} \equiv \mathbf{Q}^{(D)}$ in equation (96)

3.5. HSA

Similar to the HDD rotating disk, the HDD actuator moves circularly. Unlike the disk that rotates in a constraint speed counter-clockwise, the speed of the actuator changes over time and its direct is not fixed. Moreover, its size and thickness are smaller compared to the disk. As the acoustic effect due to actuator vibration at only the Z direction is studied, to simplify the model, the effect due to the rotational actuator will not be discussed. The following equations have been used (Gao et al., 2005)

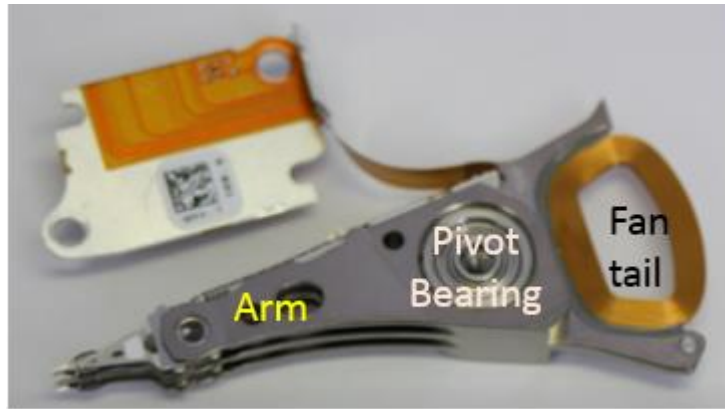


Figure 3-10 A typical example of HDD HSA

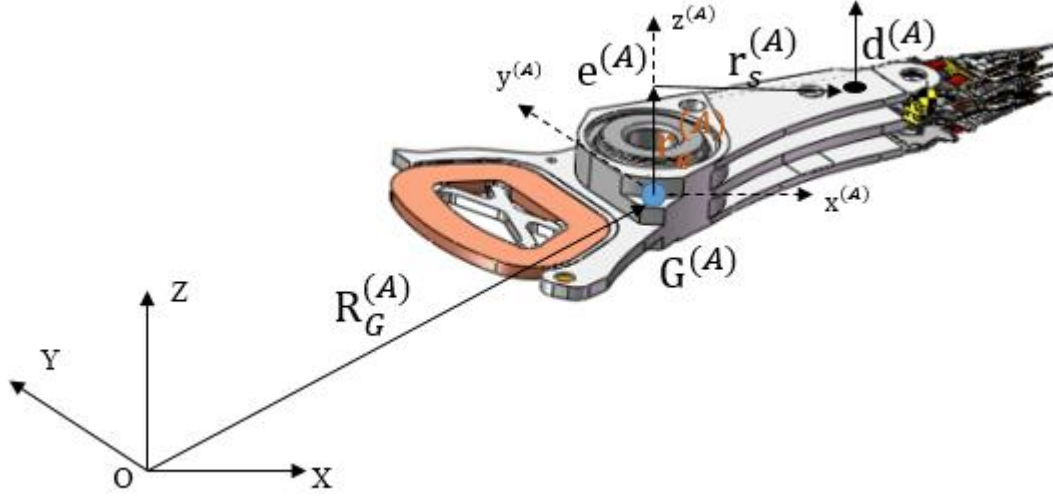


Figure 3-11 Reference frame for HDD HSA

As shown in Figure 3-11, point $G^{(A)}$ is the center of gravity for the actuator, $d^{(A)}$ is any point on the actuator, the superscript (A) represents the actuator assembly, $x^{(A)} y^{(A)} z^{(A)}$ is the actuator coordinating system, $\hat{a}\hat{b}\hat{c}$ are their corresponding unit vectors, and XYZ is the fixed frame coordinating system that is the same as that used in the rotating disk section. Applying the similar procedure showed for the rotating disk, the equations of motion can be derived as,

$$\begin{bmatrix} \hat{a} \\ \hat{b} \\ \hat{c} \end{bmatrix} \approx \begin{bmatrix} 1 & 0 & \theta_y^{(A)} \\ 0 & 1 & \theta_x^{(A)} \\ -\theta_y^{(A)} & -\theta_x^{(A)} & 1 \end{bmatrix} \begin{bmatrix} \hat{i} \\ \hat{j} \\ \hat{k} \end{bmatrix} \quad (97)$$

The position vector of point $d^{(A)}$ with respect to fix frame can be written as

$$\mathbf{R}_d^{(A)} = \mathbf{R}_G^{(A)} + \mathbf{r}_e^{(A)} + \mathbf{r}_s^{(A)} + \mathbf{d}^{(A)} \quad (98)$$

$\mathbf{R}_G^{(A)}$ can be represented as

$$\mathbf{R}_G^{(A)} = R_x^{(A)} \hat{i} + R_y^{(A)} \hat{j} + R_z^{(A)} \hat{k} \quad (99)$$

And

$$\mathbf{r}_s = r_s \cos \varepsilon \hat{a} + r_s \sin \varepsilon \hat{b} \quad (100)$$

where, ε is angle measured from $x^{(A)}$ to point $d^{(A)}$

Moreover.

$$\mathbf{r}_e^{(A)} = r_e^{(A)} \hat{c} \quad (101)$$

$d^{(A)}$ is the actuator displacement which can be calculated as a summation of a series of mode shapes

$$d^{(A)} = \sum_{m=0}^{\infty} \sum_{n=-\infty}^{\infty} w_{mn}^{(A)}(r_s, \varepsilon) q_{mn}^{(A)}(t)$$

Where $w_{mn}^{(A)}(r_s, \varepsilon)$ is the arm mode shape with m is nodal circles and n is nodal diameter

Hence,

$$\mathbf{R}_d^{(A)} = R_X^{(A)} \hat{i} + R_Y^{(A)} \hat{j} + R_Z^{(A)} \hat{K} + r_e^{(A)} \hat{c} + r_A \cos \varepsilon \hat{a} + r_A \sin \varepsilon \hat{b} + d^{(A)} \hat{c} \quad (102)$$

And the velocity of point $d^{(A)}$ can written as

$$\dot{\mathbf{R}}_d^{(A)} = \dot{\mathbf{R}}_G^{(A)} + \dot{\mathbf{r}}_e^{(A)} + \Omega \times \mathbf{r}_s^{(A)} + \dot{d}^{(A)} \quad (103)$$

where, $\dot{\mathbf{R}}_G^{(A)}$ can be written as

$$\dot{\mathbf{R}}_G^{(A)} = \dot{R}_X^{(A)} \hat{i} + \dot{R}_Y^{(A)} \hat{j} + \dot{R}_Z^{(A)} \hat{K} \quad (104)$$

And, $\dot{\mathbf{r}}_e^{(A)} + \Omega \times \mathbf{r}_s^{(A)}$ can be rearranged as

$$\dot{\mathbf{r}}_e^{(A)} + \Omega \times \mathbf{r}_s^{(A)} = \Omega \times (\mathbf{r}_e^{(A)} + \mathbf{r}_s^{(A)}) \quad (105)$$

In which, angular velocity Ω is represented by

$$\Omega \approx \dot{\theta}_x^{(A)} \hat{a} + \dot{\theta}_y^{(A)} \hat{b}$$

Hence, equation (104) can be expressed as

$$\begin{aligned} \dot{\mathbf{r}}_e^{(A)} + \Omega \times \mathbf{r}_s^{(A)} &= (\dot{\theta}_x^{(A)} \hat{a} + \dot{\theta}_y^{(A)} \hat{b}) \times (r_e^{(A)} \hat{c} + r_s \cos \varepsilon \hat{a} + r_s \sin \varepsilon \hat{b}) \\ &= \begin{vmatrix} \hat{a} & \hat{b} & \hat{c} \\ \dot{\theta}_x^{(A)} & \dot{\theta}_y^{(A)} & 0 \\ r_s \cos \varepsilon & r_s \sin \varepsilon & r_e^{(A)} \end{vmatrix} \\ &= r_e^{(A)} \dot{\theta}_y^{(A)} \hat{a} + \dot{\theta}_x^{(A)} r_s \sin \varepsilon \hat{c} - r_e^{(A)} \dot{\theta}_x^{(A)} \hat{b} - \dot{\theta}_y^{(A)} r_s \cos \varepsilon \hat{c} \\ &= r_e^{(A)} \dot{\theta}_y^{(A)} \hat{a} - r_e^{(A)} \dot{\theta}_x^{(A)} \hat{b} + (\dot{\theta}_x^{(A)} r_s \sin \varepsilon - \dot{\theta}_y^{(A)} r_s \cos \varepsilon) \hat{c} \end{aligned} \quad (106)$$

Lastly, $\dot{d}^{(A)}$ can be computed by

$$\dot{d}^{(A)} = \dot{d}^{(A)} \hat{c} + d^{(A)} \frac{d\hat{c}}{dt}$$

in which,

$$\frac{d\hat{c}}{dt} = \Omega \times \hat{c} = (\dot{\theta}_x^{(A)} \hat{a} + \dot{\theta}_y^{(A)} \hat{b}) \times \hat{c} = -\dot{\theta}_x^{(A)} \hat{b} + \dot{\theta}_y^{(A)} \hat{a} = \dot{\theta}_y^{(A)} \hat{a} - \dot{\theta}_x^{(A)} \hat{b}$$

Hence,

$$\dot{\mathbf{d}}^{(A)} = (\dot{\theta}_y^{(A)} \hat{a} - \dot{\theta}_x^{(A)} \hat{b}) \left[\sum_{m=0}^{\infty} \sum_{n=-\infty}^{\infty} w_{mn}^{(A)}(r_s, \varepsilon) q_{mn}^{(A)}(t) \right] + \left[\sum_{m=0}^{\infty} \sum_{n=-\infty}^{\infty} w_{mn}^{(A)}(r_s, \varepsilon) \dot{q}_{mn}^{(A)}(t) \right] \hat{c} \quad (107)$$

Therefore, the kinetically energy, $T^{(A)}$ can be written as

$$\begin{aligned} T^{(A)} &= \frac{1}{2} \int \dot{\mathbf{R}}_d^{(A)} \cdot \dot{\mathbf{R}}_d^{(A)} dm^{(A)} \\ &= \frac{1}{2} \int \left[\dot{\mathbf{R}}_G^{(A)} + (\dot{\mathbf{r}}_e^{(A)} + \Omega \times \mathbf{r}_s^{(A)}) + \dot{\mathbf{d}}^{(A)} \right] \\ &\quad \cdot \left[\dot{\mathbf{R}}_G^{(A)} + (\dot{\mathbf{r}}_e^{(A)} + \Omega \times \mathbf{r}_s^{(A)}) + \dot{\mathbf{d}}^{(A)} \right] dm^{(A)} \\ &= \frac{1}{2} \int \dot{\mathbf{R}}_G^{(A)} \cdot \dot{\mathbf{R}}_G^{(A)} dm^{(A)} + \frac{1}{2} \int (\dot{\mathbf{r}}_e^{(A)} + \Omega \times \mathbf{r}_s^{(A)})^2 dm^{(A)} \\ &\quad + \frac{1}{2} \int (\dot{\mathbf{d}}^{(A)})^2 dm^{(A)} + \int \dot{\mathbf{R}}_G^{(A)} \cdot (\dot{\mathbf{r}}_e^{(A)} + \Omega \times \mathbf{r}_s^{(A)}) dm^{(A)} \\ &\quad + \int \dot{\mathbf{R}}_G^{(A)} \cdot \dot{\mathbf{d}}^{(A)} dm^{(A)} + \int \dot{\mathbf{d}}^{(A)} \cdot (\dot{\mathbf{r}}_e^{(A)} + \Omega \times \mathbf{r}_s^{(A)}) dm^{(A)} \end{aligned} \quad (108)$$

Similar as pervious section, above equation can be simplified term by term. Term 1,

$$\frac{1}{2} \int \dot{\mathbf{R}}_G^{(A)} \cdot \dot{\mathbf{R}}_G^{(A)} dm^{(A)} = \frac{1}{2} m^{(A)} \left[(\dot{R}_X^{(A)})^2 + (\dot{R}_Y^{(A)})^2 + (\dot{R}_Z^{(A)})^2 \right] \quad (109)$$

Term 2,

$$\begin{aligned} \frac{1}{2} \int (\dot{\mathbf{r}}_e^{(A)} + \Omega \times \mathbf{r}_s^{(A)})^2 dm^{(A)} &= \frac{1}{2} \int \Omega \times (\mathbf{r}_e^{(A)} + \mathbf{r}_s^{(A)}) \cdot \Omega \times (\mathbf{r}_e^{(A)} + \mathbf{r}_s^{(A)}) dm^{(A)} \\ &= \frac{1}{2} \Omega \cdot I_1^{(A)} \cdot \Omega = \frac{1}{2} \begin{bmatrix} \dot{\theta}_x^{(A)} \\ \dot{\theta}_y^{(A)} \\ 0 \end{bmatrix} \begin{bmatrix} I_1^{(A)} & 0 & 0 \\ 0 & I_1^{(A)} & 0 \\ 0 & 0 & 0 \end{bmatrix} \begin{bmatrix} \dot{\theta}_x^{(A)} \\ \dot{\theta}_y^{(A)} \\ 0 \end{bmatrix} \\ &= \frac{1}{2} I_1^{(A)} \left[(\dot{\theta}_x^{(A)})^2 + (\dot{\theta}_y^{(A)})^2 \right] \end{aligned} \quad (110)$$

Term 3,

$$\begin{aligned}
& \frac{1}{2} \int (\dot{\mathbf{d}}^{(A)})^2 dm^{(A)} \\
&= \frac{1}{2} \int \left\{ \left(\dot{\theta}_y^{(A)} \hat{\mathbf{a}} - \dot{\theta}_x^{(A)} \hat{\mathbf{b}} \right) \left[\sum_{m=0}^{\infty} \sum_{n=-\infty}^{\infty} w_{mn}^{(A)}(r_s, \varepsilon) q_{mn}^{(A)}(t) \right] + \left[\sum_{m=0}^{\infty} \sum_{n=-\infty}^{\infty} w_{mn}^{(A)}(r_s, \varepsilon) \dot{q}_{mn}^{(A)}(t) \right] \hat{\mathbf{c}} \right\} \\
&\cdot \left\{ \left(\dot{\theta}_y^{(A)} \hat{\mathbf{a}} - \dot{\theta}_x^{(A)} \hat{\mathbf{b}} \right) \left[\sum_{m=0}^{\infty} \sum_{n=-\infty}^{\infty} w_{mn}^{(A)}(r_s, \varepsilon) q_{mn}^{(A)}(t) \right] + \left[\sum_{m=0}^{\infty} \sum_{n=-\infty}^{\infty} w_{mn}^{(A)}(r_s, \varepsilon) \dot{q}_{mn}^{(A)}(t) \right] \hat{\mathbf{c}} \right\} dm^{(A)} \\
&= \frac{1}{2} \int \left\{ \left(\dot{\theta}_y^{(A)} \right)^2 \left[\sum_{m=0}^{\infty} \sum_{n=-\infty}^{\infty} w_{mn}^{(A)}(r_s, \varepsilon) q_{mn}^{(A)}(t) \right]^2 + \left(\dot{\theta}_x^{(A)} \right)^2 \left[\sum_{m=0}^{\infty} \sum_{n=-\infty}^{\infty} w_{mn}^{(A)}(r_s, \varepsilon) q_{mn}^{(A)}(t) \right]^2 \right. \\
&+ \left. \left[\sum_{m=0}^{\infty} \sum_{n=-\infty}^{\infty} w_{mn}^{(A)}(r_s, \varepsilon) \dot{q}_{mn}^{(A)}(t) \right]^2 \right\} dm^{(A)} \\
&= \frac{1}{2} \int \left[\left(\dot{\theta}_y^{(A)} \right)^2 + \left(\dot{\theta}_x^{(A)} \right)^2 \right]^2 \left[\sum_{m=0}^{\infty} \sum_{n=-\infty}^{\infty} w_{mn}^{(A)}(r_s, \varepsilon) q_{mn}^{(A)}(t) \right]^2 dm^{(A)} \\
&+ \frac{1}{2} \int \left[\sum_{m=0}^{\infty} \sum_{n=-\infty}^{\infty} w_{mn}^{(A)}(r_s, \varepsilon) \dot{q}_{mn}^{(A)}(t) \right]^2 dm^{(A)} \\
&= \frac{1}{2} \left[\left(\dot{\theta}_y^{(A)} \right)^2 + \left(\dot{\theta}_x^{(A)} \right)^2 \right]^2 \sum_{m=0}^{\infty} \sum_{n=-\infty}^{\infty} \left[q_{mn}^{(A)}(t) \right]^2 \int \left(w_{mn}^{(A)}(r_s, \varepsilon) \right) \left(w_{mn}^{(A)}(r_s, \varepsilon) \right) dm^{(A)} \\
&+ \frac{1}{2} \sum_{m=0}^{\infty} \sum_{n=-\infty}^{\infty} \left[\dot{q}_{mn}^{(A)}(t) \right]^2 \int \left(w_{mn}^{(A)}(r_s, \varepsilon) \right) \left(w_{mn}^{(A)}(r_s, \varepsilon) \right) dm^{(A)} \\
&= \frac{1}{2} I_1^{(A)} \left[\left(\dot{\theta}_y^{(A)} \right)^2 + \left(\dot{\theta}_x^{(A)} \right)^2 \right]^2 \sum_{m=0}^{\infty} \sum_{n=-\infty}^{\infty} \left[q_{mn}^{(A)}(t) \right]^2 + \frac{1}{2} I_1^{(A)} \sum_{m=0}^{\infty} \sum_{n=-\infty}^{\infty} \left[\dot{q}_{mn}^{(A)}(t) \right]^2
\end{aligned} \tag{111}$$

Term 4,

$$\begin{aligned}
& \int \dot{\mathbf{R}}_G^{(A)} \cdot \left(\dot{\mathbf{r}}_e^{(A)} + \Omega \times \mathbf{r}_s^{(A)} \right) dm^{(A)} = \int \dot{\mathbf{R}}_G^{(A)} \cdot \Omega \times \left(\mathbf{r}_e^{(A)} + \mathbf{r}_s^{(A)} \right) dm^{(A)} \\
&= \int \left(\dot{R}_X^{(A)} \hat{\mathbf{I}} + \dot{R}_Y^{(A)} \hat{\mathbf{J}} + \dot{R}_Z^{(A)} \hat{\mathbf{K}} \right) \left[r_e^{(A)} \dot{\theta}_y^{(A)} \hat{\mathbf{a}} - r_e^{(A)} \dot{\theta}_x^{(A)} \hat{\mathbf{b}} \right. \\
&\quad \left. + \left(\dot{\theta}_x^{(A)} r_s \sin \varepsilon - \dot{\theta}_y^{(A)} r_s \cos \varepsilon \right) \hat{\mathbf{c}} \right] dm^{(A)}
\end{aligned} \tag{112}$$

Apply rotational matrix to above equation,

$$\begin{aligned}
& \int \dot{\mathbf{R}}_G^{(A)} \cdot \left(\dot{\mathbf{r}}_e^{(A)} + \Omega \times \mathbf{r}_s^{(A)} \right) dm^{(A)} \\
&= \int \left(\dot{R}_X^{(A)} \hat{\mathbf{I}} + \dot{R}_Y^{(A)} \hat{\mathbf{J}} + \dot{R}_Z^{(A)} \hat{\mathbf{K}} \right) \left[r_e^{(A)} \dot{\theta}_y^{(A)} (\hat{\mathbf{I}} + \theta_y^{(A)} \hat{\mathbf{J}}) - r_e^{(A)} \dot{\theta}_x^{(A)} (\hat{\mathbf{J}} + \theta_x^{(A)} \hat{\mathbf{K}}) \right. \\
&\quad \left. + \left(\dot{\theta}_x^{(A)} r_s \sin \varepsilon - \dot{\theta}_y^{(A)} r_s \cos \varepsilon \right) (-\theta_y^{(A)} \hat{\mathbf{I}} - \theta_x^{(A)} \hat{\mathbf{J}} + \hat{\mathbf{K}}) \right] dm^{(A)}
\end{aligned}$$

All the terms in above equation is more than 2nd order, hence, the term 4 dropped off from further analysis.

$$\int \dot{\mathbf{R}}_G^{(A)} \cdot (\dot{\mathbf{r}}_e^{(A)} + \Omega \times \mathbf{r}_s^{(A)}) dm^{(A)} \approx 0$$

Term 5,

$$\begin{aligned} & \int \dot{\mathbf{R}}_G^{(A)} \cdot \dot{\mathbf{d}}^{(A)} dm^{(A)} \\ &= (\dot{R}_X^{(A)} \hat{i} + \dot{R}_Y^{(A)} \hat{j} \\ &+ \dot{R}_Z^{(A)} \hat{K}) \int \left\{ (\dot{\theta}_y^{(A)} \hat{a} - \dot{\theta}_x^{(A)} \hat{b}) \left[\sum_{m=0}^{\infty} \sum_{n=-\infty}^{\infty} w_{mn}^{(A)}(r_s, \varepsilon) q_{mn}^{(A)}(t) \right] \right. \\ &+ \left. \left[\sum_{m=0}^{\infty} \sum_{n=-\infty}^{\infty} w_{mn}^{(A)}(r_s, \varepsilon) \dot{q}_{mn}^{(A)}(t) \right] \hat{c} \right\} dm^{(A)} \\ &= (\dot{R}_X^{(A)} \hat{i} + \dot{R}_Y^{(A)} \hat{j} \\ &+ \dot{R}_Z^{(A)} \hat{K}) \left\{ (\dot{\theta}_y^{(A)} \hat{a} - \dot{\theta}_x^{(A)} \hat{b}) \sum_{m=0}^{\infty} \sum_{n=-\infty}^{\infty} q_{mn}^{(A)}(t) \int w_{mn}^{(A)}(r_s, \varepsilon) dm^{(A)} \right. \\ &+ \left. \left[\sum_{m=0}^{\infty} \sum_{n=-\infty}^{\infty} \dot{q}_{mn}^{(A)}(t) \right] \hat{c} \int w_{mn}^{(A)}(r_s, \varepsilon) dm^{(A)} \right\} \end{aligned}$$

Define, a constant $b_{mn}^{(A)}$

$$b^{(A)} = \int w_{mn}^{(A)}(r_s, \varepsilon) dm^{(A)}$$

Hence,

$$\begin{aligned} & \int \dot{\mathbf{R}}_G^{(A)} \cdot \dot{\mathbf{d}}^{(A)} dm^{(A)} \\ &= b_{mn}^{(A)} (\dot{R}_X^{(A)} \hat{i} + \dot{R}_Y^{(A)} \hat{j} + \dot{R}_Z^{(A)} \hat{K}) \left\{ (\dot{\theta}_y^{(A)} \hat{a} - \dot{\theta}_x^{(A)} \hat{b}) \sum_{m=0}^{\infty} \sum_{n=-\infty}^{\infty} q_{mn}^{(A)}(t) \right. \\ &+ \left. \left[\sum_{m=0}^{\infty} \sum_{n=-\infty}^{\infty} \dot{q}_{mn}^{(A)}(t) \right] \hat{c} \right\} \end{aligned}$$

As mentioned previously, the analysis in this chapter only consider the event related to z direction hence,

$$\int \dot{\mathbf{R}}_G^{(A)} \cdot \dot{\mathbf{d}}^{(A)} dm^{(A)} = b_{mn}^{(A)} \dot{R}_Z^{(A)} \left[\sum_{m=0}^{\infty} \sum_{n=-\infty}^{\infty} \dot{q}_{mn}^{(A)}(t) \right] \quad (113)$$

Term 6,

$$\begin{aligned}
& \int \dot{\mathbf{d}}^{(A)} \cdot \left(\dot{\mathbf{r}}_e^{(A)} + \Omega \times \mathbf{r}_s^{(A)} \right) dm^{(A)} \\
&= \int \left\{ \left(\dot{\theta}_y^{(A)} \hat{a} - \dot{\theta}_x^{(A)} \hat{b} \right) \left[\sum_{m=0}^{\infty} \sum_{n=-\infty}^{\infty} w_{mn}^{(A)}(r_s, \varepsilon) q_{mn}^{(A)}(t) \right] \right. \\
&+ \left. \left[\sum_{m=0}^{\infty} \sum_{n=-\infty}^{\infty} w_{mn}^{(A)}(r_s, \varepsilon) \dot{q}_{mn}^{(A)}(t) \right] \hat{c} \right\} \\
&\cdot \left[r_e^{(A)} \dot{\theta}_y^{(A)} \hat{a} - r_e^{(A)} \dot{\theta}_x^{(A)} \hat{b} + \left(\dot{\theta}_x^{(A)} r_s \sin \varepsilon - \dot{\theta}_y^{(A)} r_s \cos \varepsilon \right) \hat{c} \right] dm^{(A)} \\
&= \left[r_e^{(A)} \left(\dot{\theta}_y^{(A)} \right)^2 + r_e^{(A)} \left(\dot{\theta}_x^{(A)} \right)^2 \right] \left[\sum_{m=0}^{\infty} \sum_{n=-\infty}^{\infty} q_{mn}^{(A)}(t) \right] \int w_{mn}^{(A)}(r_s, \varepsilon) dm^{(A)} \\
&+ \left(\dot{\theta}_x^{(A)} r_s \sin \varepsilon - \dot{\theta}_y^{(A)} r_s \cos \varepsilon \right) \left[\sum_{m=0}^{\infty} \sum_{n=-\infty}^{\infty} \dot{q}_{mn}^{(A)}(t) \right] \int w_{mn}^{(A)}(r_s, \varepsilon) dm^{(A)} \\
&= \left[r_e^{(A)} \left(\dot{\theta}_y^{(A)} \right)^2 + r_e^{(A)} \left(\dot{\theta}_x^{(A)} \right)^2 \right] \left[\sum_{m=0}^{\infty} \sum_{n=-\infty}^{\infty} b_{mn}^{(A)} q_{mn}^{(A)}(t) \right] \\
&+ \left(\dot{\theta}_x^{(A)} r_s \sin \varepsilon - \dot{\theta}_y^{(A)} r_s \cos \varepsilon \right) \left[\sum_{m=0}^{\infty} \sum_{n=-\infty}^{\infty} b_{mn}^{(A)} \dot{q}_{mn}^{(A)}(t) \right]
\end{aligned} \tag{114}$$

The potential energy $V^{(A)}$

$$V^{(A)} = \frac{1}{2} I x^2 = \frac{1}{2} I_1^{(A)} \sum_{m=0}^{\infty} \sum_{n=-\infty}^{\infty} \left[w_{mn}^{(A)}(r_s, \varepsilon) q_{mn}^{(A)}(t) \right]^2$$

The langrage equation can be formed

$$\begin{aligned}
L^{(A)} &= T^{(A)} - V^{(A)} \\
&= \frac{1}{2} m^{(A)} \left[\left(\dot{R}_x^{(A)} \right)^2 + \left(\dot{R}_y^{(A)} \right)^2 + \left(\dot{R}_z^{(A)} \right)^2 \right] + \frac{1}{2} I_1^{(A)} \left[\left(\dot{\theta}_x^{(A)} \right)^2 + \left(\dot{\theta}_y^{(A)} \right)^2 \right] \\
&+ \frac{1}{2} I_1^{(A)} \left[\left(\dot{\theta}_y^{(A)} \right)^2 + \left(\dot{\theta}_x^{(A)} \right)^2 \right]^2 \sum_{m=0}^{\infty} \sum_{n=-\infty}^{\infty} \left[q_{mn}^{(A)}(t) \right]^2 \\
&+ \frac{1}{2} I_1^{(A)} \sum_{m=0}^{\infty} \sum_{n=-\infty}^{\infty} \left[\dot{q}_{mn}^{(A)}(t) \right]^2 + b_{mn}^{(A)} \dot{R}_z^{(A)} \left[\sum_{m=0}^{\infty} \sum_{n=-\infty}^{\infty} \dot{q}_{mn}^{(A)}(t) \right] \\
&+ \left[r_e^{(A)} \left(\dot{\theta}_y^{(A)} \right)^2 + r_e^{(A)} \left(\dot{\theta}_x^{(A)} \right)^2 \right] \left[\sum_{m=0}^{\infty} \sum_{n=-\infty}^{\infty} b_{mn}^{(A)} q_{mn}^{(A)}(t) \right] \\
&+ \left(\dot{\theta}_x^{(A)} r_s \sin \varepsilon - \dot{\theta}_y^{(A)} r_s \cos \varepsilon \right) \left[\sum_{m=0}^{\infty} \sum_{n=-\infty}^{\infty} b_{mn}^{(A)} \dot{q}_{mn}^{(A)}(t) \right] \\
&- \frac{1}{2} I_1^{(A)} \sum_{m=0}^{\infty} \sum_{n=-\infty}^{\infty} \left[w_{mn}^{(A)}(r_s, \varepsilon) q_{mn}^{(A)}(t) \right]^2
\end{aligned} \tag{115}$$

Hence,

$$\begin{aligned}
\frac{\partial L^{(A)}}{\partial \dot{q}^{(A)}} &= m^{(A)} \left[\dot{R}_X^{(A)} + \dot{R}_Y^{(A)} + \dot{R}_Z^{(A)} \right] + I_1^{(A)} \left[\dot{\theta}_x^{(A)} + \dot{\theta}_y^{(A)} \right] \\
&\quad + 2I_1^{(A)} \left(\dot{\theta}_y^{(A)} + \dot{\theta}_x^{(A)} \right) \left[\left(\dot{\theta}_y^{(A)} \right)^2 + \left(\dot{\theta}_x^{(A)} \right)^2 \right] \sum_{m=0}^{\infty} \sum_{n=-\infty}^{\infty} \left[q_{mn}^{(A)}(t) \right]^2 \\
&\quad + I_1^{(A)} \sum_{m=0}^{\infty} \sum_{n=-\infty}^{\infty} \dot{q}_{mn}^{(A)}(t) + b_{mn}^{(A)} \left[\sum_{m=0}^{\infty} \sum_{n=-\infty}^{\infty} \dot{q}_{mn}^{(A)}(t) \right] + b_{mn}^{(A)} \dot{R}_Z^{(A)} \\
&\quad + \left[2r_e^{(A)} \dot{\theta}_y^{(A)} + 2r_e^{(A)} \dot{\theta}_x^{(A)} \right] \left[\sum_{m=0}^{\infty} \sum_{n=-\infty}^{\infty} b_{mn}^{(A)} q_{mn}^{(A)}(t) \right] \\
&\quad + (r_s \sin \varepsilon - r_s \cos \varepsilon) \left[\sum_{m=0}^{\infty} \sum_{n=-\infty}^{\infty} b_{mn}^{(A)} \dot{q}_{mn}^{(A)}(t) \right] \\
&\quad + \left(\dot{\theta}_x^{(A)} r_s \sin \varepsilon - \dot{\theta}_y^{(A)} r_s \cos \varepsilon \right) \left[\sum_{m=0}^{\infty} \sum_{n=-\infty}^{\infty} b_{mn}^{(A)} \right]
\end{aligned} \tag{116}$$

Thus,

$$\begin{aligned}
\frac{d}{dt} \left(\frac{\partial L^{(A)}}{\partial \dot{q}^{(A)}} \right) &= m^{(A)} \left[\ddot{R}_X^{(A)} + \ddot{R}_Y^{(A)} + \ddot{R}_Z^{(A)} \right] + I_1^{(A)} \left[\ddot{\theta}_x^{(A)} + \ddot{\theta}_y^{(A)} \right] \\
&\quad + 2I_1^{(A)} \left(\ddot{\theta}_y^{(A)} + \ddot{\theta}_x^{(A)} \right) \left[\left(\ddot{\theta}_y^{(A)} \right)^2 + \left(\ddot{\theta}_x^{(A)} \right)^2 \right] \sum_{m=0}^{\infty} \sum_{n=-\infty}^{\infty} \left[\dot{q}_{mn}^{(A)}(t) \right]^2 \\
&\quad + I_1^{(A)} \sum_{m=0}^{\infty} \sum_{n=-\infty}^{\infty} \ddot{q}_{mn}^{(A)}(t) + b_{mn}^{(A)} \left[\sum_{m=0}^{\infty} \sum_{n=-\infty}^{\infty} \ddot{q}_{mn}^{(A)}(t) \right] + b_{mn}^{(A)} \ddot{R}_Z^{(A)} \\
&\quad + \left[2r_e^{(A)} \ddot{\theta}_y^{(A)} + 2r_e^{(A)} \ddot{\theta}_x^{(A)} \right] \left[\sum_{m=0}^{\infty} \sum_{n=-\infty}^{\infty} b_{mn}^{(A)} \dot{q}_{mn}^{(A)}(t) \right] \\
&\quad + (r_s \sin \varepsilon - r_s \cos \varepsilon) \left[\sum_{m=0}^{\infty} \sum_{n=-\infty}^{\infty} b_{mn}^{(A)} \ddot{q}_{mn}^{(A)}(t) \right] \\
&\quad + \left(\ddot{\theta}_x^{(A)} r_s \sin \varepsilon - \ddot{\theta}_y^{(A)} r_s \cos \varepsilon \right) \left[\sum_{m=0}^{\infty} \sum_{n=-\infty}^{\infty} b_{mn}^{(A)} \right]
\end{aligned}$$

Terms higher than 2nd order are removed and the above equation can then be simplified as

$$\begin{aligned}
\frac{d}{dt} \left(\frac{\partial L^{(A)}}{\partial \dot{q}^{(A)}} \right) &= m^{(A)} \left[\ddot{R}_X^{(A)} + \ddot{R}_Y^{(A)} + \ddot{R}_Z^{(A)} \right] + I_1^{(A)} \left[\ddot{\theta}_x^{(A)} + \ddot{\theta}_y^{(A)} \right] + I_1^{(A)} \sum_{m=0}^{\infty} \sum_{n=-\infty}^{\infty} \ddot{q}_{mn}^{(A)}(t) \\
&\quad + b_{mn}^{(A)} \left[\sum_{m=0}^{\infty} \sum_{n=-\infty}^{\infty} \ddot{q}_{mn}^{(A)}(t) \right] + b_{mn}^{(A)} \ddot{R}_Z^{(A)} \\
&\quad + (r_s \sin \varepsilon - r_s \cos \varepsilon) \left[\sum_{m=0}^{\infty} \sum_{n=-\infty}^{\infty} b_{mn}^{(A)} \ddot{q}_{mn}^{(A)}(t) \right] \\
&\quad + \left(\ddot{\theta}_x^{(A)} r_s \sin \varepsilon - \ddot{\theta}_y^{(A)} r_s \cos \varepsilon \right) \left[\sum_{m=0}^{\infty} \sum_{n=-\infty}^{\infty} b_{mn}^{(A)} \right]
\end{aligned} \tag{117}$$

From langrage equation, $\frac{\partial L^{(A)}}{\partial q^{(A)}}$ can be derived as

$$\begin{aligned} \frac{\partial L^{(A)}}{\partial q^{(A)}} = & I_1^{(A)} \left[\left(\dot{\theta}_y^{(A)} \right)^2 + \left(\dot{\theta}_x^{(A)} \right)^2 \right]^2 \sum_{m=0}^{\infty} \sum_{n=-\infty}^{\infty} q_{mn}^{(A)}(t) \\ & + \left[r_e^{(A)} \left(\dot{\theta}_y^{(A)} \right)^2 + r_e^{(A)} \left(\dot{\theta}_x^{(A)} \right)^2 \right] \left[\sum_{m=0}^{\infty} \sum_{n=-\infty}^{\infty} b_{mn}^{(A)} \right] \\ & - I_1^{(A)} \sum_{m=0}^{\infty} \sum_{n=-\infty}^{\infty} \left[w_{mn}^{(A)}(r_s, \varepsilon) q_{mn}^{(A)}(t) \right] \end{aligned}$$

Dropping the higher order term gives

$$\frac{\partial L^{(A)}}{\partial q^{(A)}} = -I_1^{(A)} \sum_{m=0}^{\infty} \sum_{n=-\infty}^{\infty} \left[w_{mn}^{(A)}(r_s, \varepsilon) q_{mn}^{(A)}(t) \right] \quad (118)$$

Therefore,

$$\begin{aligned} \frac{d}{dt} \left(\frac{\partial L^{(A)}}{\partial \dot{q}^{(A)}} \right) - \frac{\partial L^{(A)}}{\partial q^{(A)}} & = m^{(A)} \left[\ddot{R}_X^{(A)} + \ddot{R}_Y^{(A)} + \ddot{R}_Z^{(A)} \right] + I_1^{(A)} \left[\ddot{\theta}_x^{(A)} + \ddot{\theta}_y^{(A)} \right] + I_1^{(A)} \sum_{m=0}^{\infty} \sum_{n=-\infty}^{\infty} \ddot{q}_{mn}^{(A)}(t) \\ & + b_{mn}^{(A)} \left[\sum_{m=0}^{\infty} \sum_{n=-\infty}^{\infty} \ddot{q}_{mn}^{(A)}(t) \right] + b_{mn}^{(A)} \ddot{R}_Z^{(A)} \\ & + (r_s \sin \varepsilon - r_s \cos \varepsilon) \left[\sum_{m=0}^{\infty} \sum_{n=-\infty}^{\infty} b_{mn}^{(A)} \ddot{q}_{mn}^{(A)}(t) \right] \\ & + \left(\ddot{\theta}_x^{(A)} r_s \sin \varepsilon - \ddot{\theta}_y^{(A)} r_s \cos \varepsilon \right) \left[\sum_{m=0}^{\infty} \sum_{n=-\infty}^{\infty} b_{mn}^{(A)} \right] \\ & + I_1^{(A)} \sum_{m=0}^{\infty} \sum_{n=-\infty}^{\infty} \left[w_{mn}^{(A)}(r_s, \varepsilon) q_{mn}^{(A)}(t) \right] \\ & = m^{(A)} \ddot{R}_X^{(A)} + m^{(A)} \ddot{R}_Y^{(A)} + \left(m^{(A)} + b_{mn}^{(A)} \right) \ddot{R}_Z^{(A)} \\ & + \left[I_1^{(A)} + r_s \sin \varepsilon \sum_{m=0}^{\infty} \sum_{n=-\infty}^{\infty} b_{mn}^{(A)} \right] \ddot{\theta}_x^{(A)} + \left[I_1^{(A)} - r_s \cos \varepsilon \sum_{m=0}^{\infty} \sum_{n=-\infty}^{\infty} b_{mn}^{(A)} \right] \ddot{\theta}_y^{(A)} \\ & + \sum_{m=0}^{\infty} \sum_{n=-\infty}^{\infty} \left[I_1^{(A)} + b_{mn}^{(A)} \left(\ddot{\theta}_x^{(A)} r_s \sin \varepsilon - \ddot{\theta}_y^{(A)} r_s \cos \varepsilon \right) \right] \ddot{q}_{mn}^{(A)}(t) \\ & + \sum_{m=0}^{\infty} \sum_{n=-\infty}^{\infty} I_1^{(A)} w_{mn}^{(A)}(r_s, \varepsilon) q_{mn}^{(A)}(t) \end{aligned} \quad (119)$$

From the above equation, the general displacement and the corresponding general force can be identified as,

$$\mathbf{q}^{(A)} = \begin{bmatrix} R_X^{(A)} \\ R_Y^{(A)} \\ R_Z^{(A)} \\ \theta_x^{(A)} \\ \theta_y^{(A)} \\ q_{mn}^{(A)}(t) \end{bmatrix} \text{ and } \mathbf{Q}^{(A)} = \begin{bmatrix} F_X^{(A)} \\ F_Y^{(A)} \\ F_Z^{(A)} \\ M_x^{(A)} \\ M_y^{(A)} \\ Q_{mn}^{(A)}(t) \end{bmatrix}$$

Hence, the equation motion can be formulated as

$$\mathbf{M}^{(A)} \ddot{\mathbf{q}}^{(A)} + \mathbf{K}^{(A)} \mathbf{q}^{(A)} = \mathbf{Q}^{(A)} \quad (120)$$

where, $\mathbf{M}^{(A)}$ is mass matrix; $\mathbf{K}^{(A)}$ is stiffness matrix;

Applying the same procedure as in the previous section i.e. equation (55) to (69), the term $\phi^{(A)}$ can be computed by

$$\phi_a^{(A)} = \left[-\omega^2 \mathbf{M}_a^{(A)} + \mathbf{K}_a^{(A)} \right]^{-1} \int_S i\omega \mathbf{q}_S^{(A)} \cdot \mathbf{n} \cdot N_n dA \quad (121)$$

where $\mathbf{q}_S^{(A)}$ can be calculated through

$$\mathbf{q}_S^{(A)} = \left[-\omega^2 \mathbf{M}_S^{(A)} + \mathbf{K}_S^{(A)} \right]^{-1} \mathbf{Q}_S^{(A)} \quad (122)$$

where, $\mathbf{q}_S^{(A)} \equiv \mathbf{q}^{(A)}$ and $\mathbf{Q}_S^{(A)} \equiv \mathbf{Q}^{(A)}$

3.6. Summary

In this chapter, a detailed and step-by-step theoretical formulation is presented. It starts with an assumption that the total velocity potential of the 2.5" HDD (ϕ_{total}) could be approximated as the sum of the individual velocity potential of the four components, i.e. two point sources ($\phi_{point\ sources}$), the rotating disk ($\phi^{(D)}$), the HSA ($\phi^{(A)}$) and the stationary parts ($\phi^{(S)}$).

In section 3.2, the velocity potential of a point source was expressed as equation (34) shown below. This equation could be used to identify the effect of the two point sources acting on the viewing plate at the near field with finite element analysis (FEA).

$$\phi_{point\ source} = (-k^2 \mathbf{M}_a + \mathbf{K}_a)^{-1} (\mathbf{f}_a + \mathbf{Q}_{source}) \quad (123)$$

where

$$\mathbf{K}_a = \int_V \nabla N_m \nabla N_n dV$$

$$\mathbf{M}_a = \frac{1}{c^2} \int_V N_m N_n dV$$

$$\mathbf{f}_a = \int_S \gamma N_n dA$$

$$\begin{aligned} \mathbf{Q}_{source} = j\omega\rho_0 [& q^{(A)} \cos \frac{a\pi x^{(A)}}{80} \cos \frac{b\pi y^{(A)}}{65} \cos \frac{c\pi z^{(A)}}{5} \\ & + q^{(S)} \cos \frac{a\pi x^{(S)}}{80} \cos \frac{b\pi y^{(S)}}{65} \cos \frac{c\pi z^{(S)}}{5}] \end{aligned}$$

In the above equation, the excitation source is two acoustical point sources. However, for the rest of components, the major excitation source is the motor forces. There are two motors in the HDD, i.e. the spindle motor and voice coil motor (VCM). To compute the spindle motor force, the total z-directional force can be obtained by summation of all the axial forces (f_{axial}) of each tooth.

$$F_z^{(sp)} = \sum_i^{tn} (f_{axial})_i$$

The axial force at each tooth can be calculated from the equation below.

$$f_{axial}^{(sp)} = \int_S f_z dS$$

where the term f_z can be computed as follows.

$$f_z = \frac{B_n B_z}{\mu_0}$$

where B_n is the normal flux density, B_z is axial flux density, μ_0 is the permeability of air, and f_z is the axial force density.

As for the VCM force, the torque can be calculated as

$$T^{VCM} = l_c \int_A r_v J_c B_z^{VCM} dA$$

where l_c is the equivalent coil length, r_v is the radius from the pivot point to the magnetic field, J_c is the current density of coil and B_z^{VCM} is the axial magnetic flux density of a VCM.

With excitation forces identification, the acoustical response of all the other components can then be expressed as follows.

For the HDD stationary parts, the velocity potential is

$$\phi_a^{(S)} = \left[-\omega^2 \mathbf{M}_a^{(S)} + \mathbf{K}_a^{(S)} \right]^{-1} \int_S i\omega \mathbf{u}_s^{(S)} \cdot \mathbf{n} \cdot N_n dA$$

Since the acoustical response is due to the structural vibration, the term $\mathbf{u}_s^{(S)}$ is the displacement of the surfaces of the stationary parts and it can be computed using the formula below.

$$\mathbf{u}_s^{(S)} = \left[-\omega^2 \mathbf{M}_s^{(S)} + \mathbf{K}_s^{(S)} \right]^{-1} \mathbf{F}_s^{(S)}$$

where $\mathbf{M}_s^{(S)} = \text{diag}\{[I^{(C)}, I^{(B)}, I^{(P)}]\}$, and $I^{(C)}$, $I^{(B)}$ and $I^{(P)}$ are the identical matrix for the cover, base and pole plates respectively.

$\mathbf{K}_s^{(S)} = \text{diag}\{[\omega_n^{(C)}, \omega_n^{(B)}, \omega_n^{(P)}]\}$, where $\omega_n^{(C)}$, $\omega_n^{(B)}$ and $\omega_n^{(P)}$ are the natural frequencies for the cover, base and pole plates respectively.

$$\mathbf{F}_s^{(S)} = \begin{bmatrix} Q_n^{(C)} \\ Q_n^{(B)} \\ Q_n^{(P)} \end{bmatrix}$$

where $Q_n^{(C)}$, $Q_n^{(B)}$ and $Q_n^{(P)}$ are the generalized force vendors for the cover, base and pole plates respectively.

$$\mathbf{u}_S^{(S)} = \begin{bmatrix} q_n^{(C)} \\ q_n^{(B)} \\ q_n^{(P)} \end{bmatrix}$$

where $q_n^{(C)}$, $q_n^{(B)}$, $q_n^{(P)}$ are generalized displacement vectors for the cover, base and pole plates.

For rotating disk, the acoustical velocity potential can be obtained through the equation below.

$$\phi_a^{(D)} = \left[-\omega^2 \mathbf{M}_a^{(D)} + \mathbf{K}_a^{(D)} \right]^{-1} \int_S i\omega \mathbf{q}_S^{(D)} \cdot \mathbf{n} \cdot N_n dA$$

where $\mathbf{q}_S^{(D)}$ is the general displacement of the disk and can be calculated using

$$\mathbf{q}_S^{(D)} = \left[-\omega^2 \mathbf{M}_S^{(D)} + i\omega \mathbf{C}_S^{(D)} + \mathbf{K}_S^{(D)} \right]^{-1} \mathbf{Q}_S^{(D)}$$

Similarly, for the HSA, the acoustical velocity potential is

$$\phi_a^{(A)} = \left[-\omega^2 \mathbf{M}_a^{(A)} + \mathbf{K}_a^{(A)} \right]^{-1} \int_S i\omega \mathbf{q}_S^{(A)} \cdot \mathbf{n} \cdot N_n dA$$

where $\mathbf{q}_S^{(A)}$ can be calculated using

$$\mathbf{q}_S^{(A)} = \left[-\omega^2 \mathbf{M}_S^{(A)} + \mathbf{K}_S^{(A)} \right]^{-1} \mathbf{Q}_S^{(A)}$$

Chapter 4. Validation study

There are two main hypotheses in this thesis:

1. Equation (7) can be used to estimate the near field acoustic pressure and velocity at the source plane.
2. Equation (4) can be used to estimate the far field acoustic pressure at the receiver end. The psychoacoustic parameter can then be computed using this far field acoustic pressure.

In this chapter, both hypotheses will be validated by laboratory measurement and numerical solutions.

The 2.5" HDD that was used to produce the sound sample #7 in Jury Test 2 was used in this study. Unlike the binaural recording setup in Jury Test 2, a single microphone was used to measure the acoustic pressures in the far field, and a microphone array was used to measure them in the near field (Section 4.1). After the measurements, the Finite Element Method (FEM) model was built to calculate the acoustic pressures at the near field, which is then used to predict the far field values (Section 4.2). Finally, the calculated result is compared with the measurement data, and the similarity and the differences are discussed in Section 4.3.

Part of Sections 4.1 and 4.2 used the materials from the following papers published during the PhD. candidature. (Ma et al., 2017)

MA, Y., CHIN, C. S. & WOO, W. L. 2017. Evaluating 2.5" Hard Disk Drive Noise Source Identification. INTER-NOISE and NOISE-CON Congress and Conference Proceedings, 255, 1782-1787.

4.1. Experimental measurement

The acoustic measurements at the far field and the near field were conducted in an anechoic chamber in the Seagate Singapore Design Center. Figure 4-1 shows the background noise of

the chamber. The measurement condition was created as described in ISO 7779. The chamber temperature was kept at $23\pm 1^{\circ}\text{C}$, the humidity level at $50\pm 5\%$, and the atmospheric pressure at 1 atmospheric pressure throughout the measurements (Ma et al., 2017).

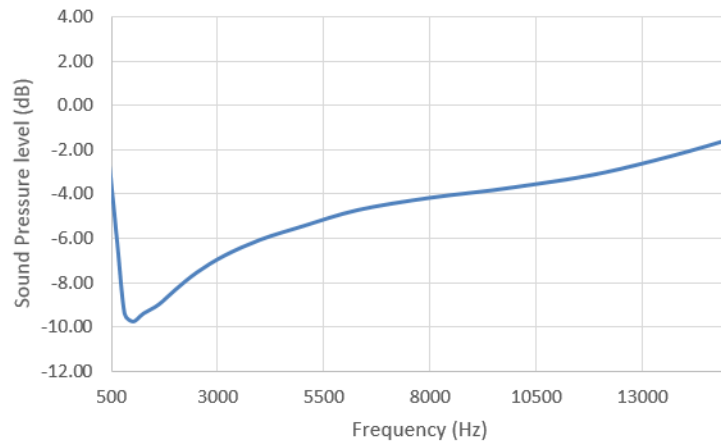


Figure 4-1 Background noise of the anechoic chamber measured by B&K 4955 microphone

4.1.1. At far field (Receiver end)

At the receiver end, the acoustic pressure is a critical data point in this thesis. It not only provides a validation for the prediction based on equation (4), but also can be used for psychoacoustic parameter calculation.

In this section, the acoustic pressure measurement at the receiver end mainly serves as a validation for the prediction based on equation (4) at end of this Chapter.

Figure 4-2 shows the difference of using a single microphone and a binaural head to measure a far field sound event. When using a binaural head, some of the sound energy will be reflected away because of the head dimension and by the skin material (Figure 4-2 Left). This effect will not be significant when using a single microphone (Figure 4-2 Right). For this reason, a microphone replaces the binaural head in this study.

The setup for the far field measurement is shown in Figure 4.3. The HDD was placed on the table with four EAR ISO dampers, each under one of the four corners of the HDD. The microphone was placed 1.2 m above the ground and has a horizontal distance of 25 cm from

the edge of the HDD. This setup was developed based on ISO 7779 (ISO7779, 2010). The HDD was operated in the random write/read mode for this measurement.

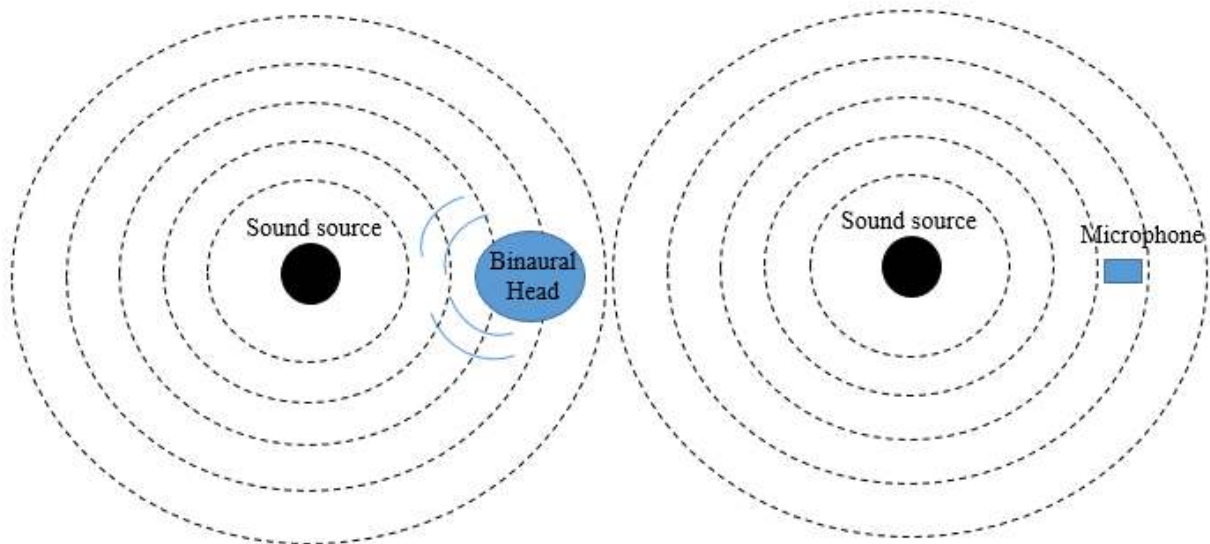


Figure 4-2 Far field sound measurement using binaural head (Left); sound measurement using microphone (Right)

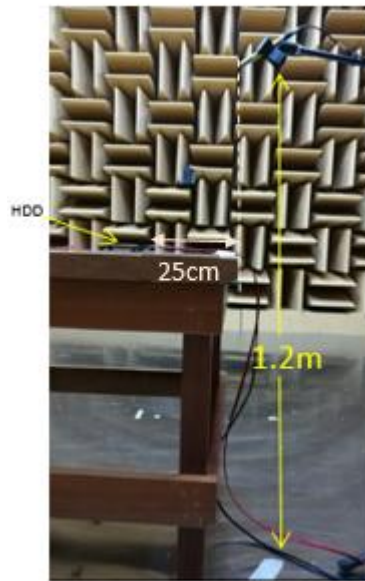


Figure 4-3 Far field measurement setup

The Fast Fourier Transform (FFT) results are presented in Figure 4-4. A highest sound energy signal was found at 3384 Hz, with a few other high tones at 2164 Hz, 2268 Hz, 3244 Hz and 4868 Hz. Near field measurements were carried out subsequently to determine the origins of these signals.

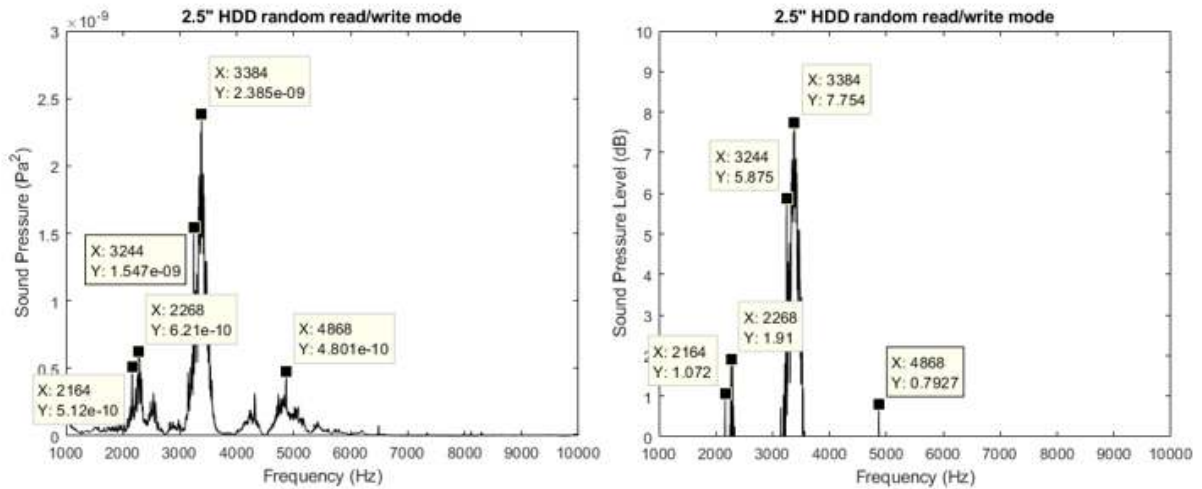


Figure 4-4 HDD far field FFT results: sound pressure in Pa² (Left) and SPL in dB (Right)

4.1.2. Near field measurements (source plane)

The main purpose for conducting the near field measurement is to identify the arbitrary weighting functions A, B, C and D that are used in equation (7).

Figure 4-5 shows the microphone used in this test. Figure 4-6 shows the design of the aluminum fixture used. The top surface of the fixture is about 20 mm thick. This is to ensure that the microphone can be held firmly in place without tilting.

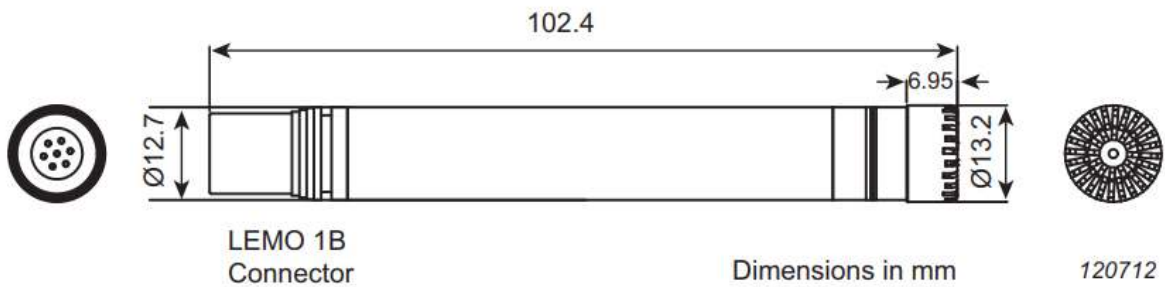


Figure 4-5 Dimensions of microphone 4955

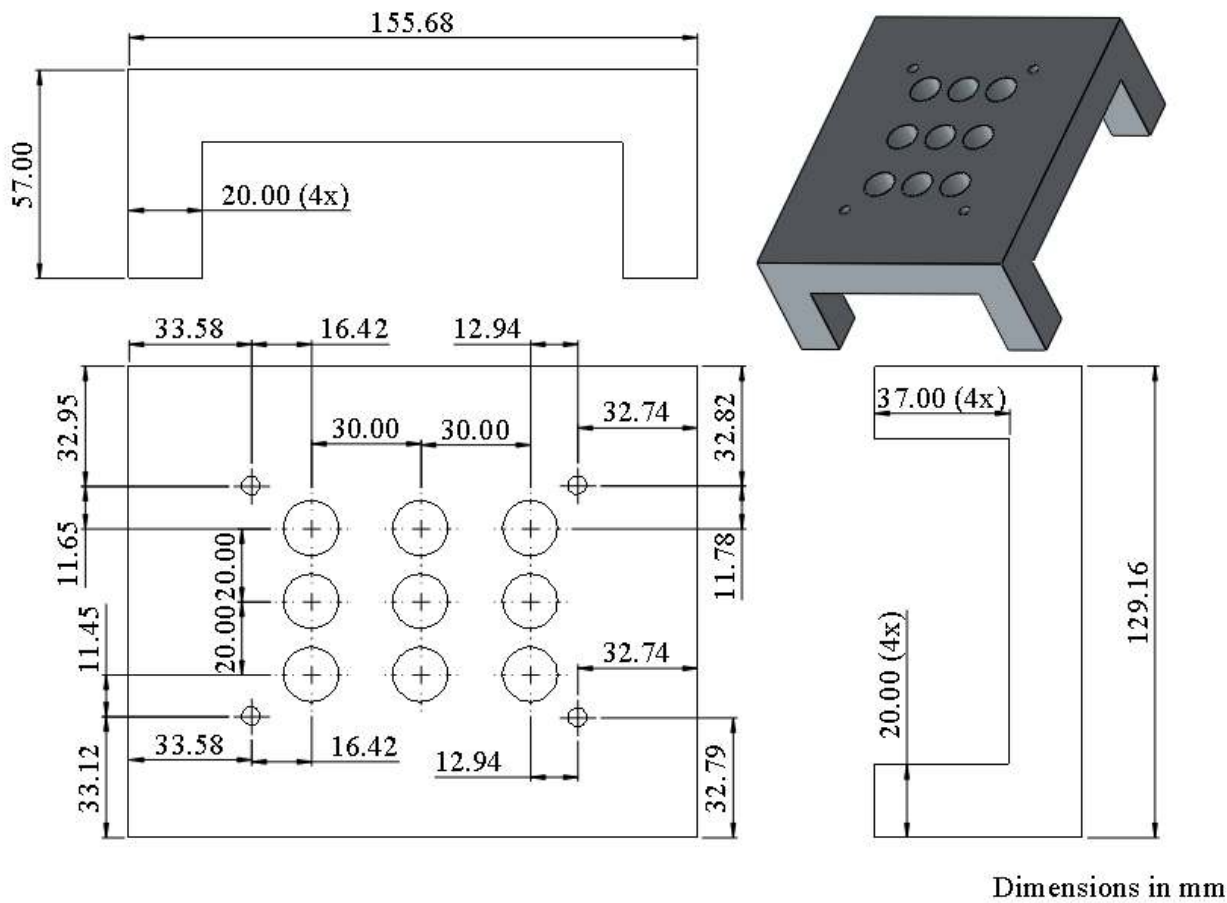
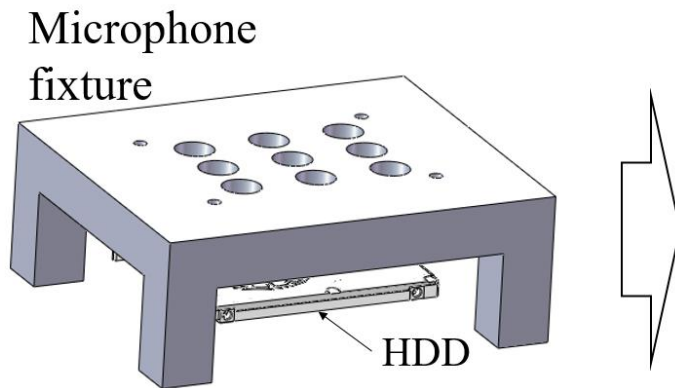


Figure 4-6 The design of the aluminum fixture

Figure 4-7 shows the microphone array setup of the near field measurement. The 2.5" HDD was placed onto four EAR ISO dampers as before. A total of nine B&K 4955 low noise microphones were placed at the specified locations in an aluminum fixture. The microphones were held at a close distance of 1 cm above the surface of the HDD in order to minimize the sound reflections that might be caused by the aluminum block, which can cause error during the measurement.

Design



Actual setup

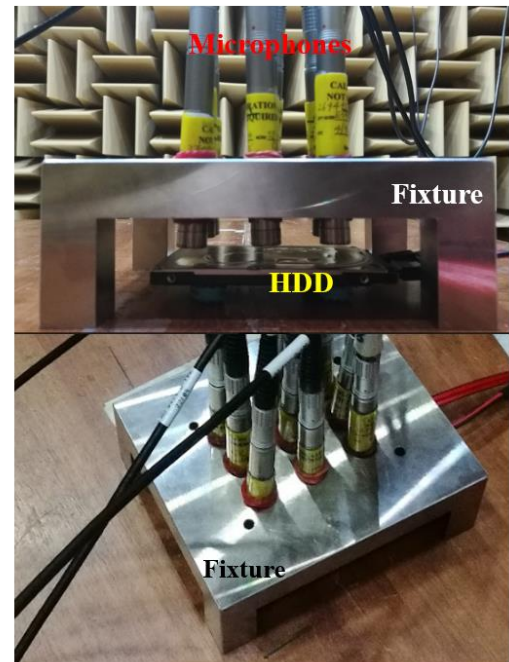


Figure 4-7 Setup of the near-field acoustic measurement

The measurement was conducted in the following steps:

- First, the background noise was measured without the HDD.
- Then, the HDD was put in place and the noise emitted from it was measured.

The measured results were processed using the MATLAB™ software. All the results including the background noise were processed as frequency, and the background noise was deducted from the HDD measurement to obtain the near field data. Since nine microphones were used, the linear interpolation was applied to obtain the data between microphones. Figure 4-8 shows the near-field acoustical holographs (NAH) at the frequencies of interest. Based on the location where the strongest sound pressures were detected, the noise of 2164 Hz was attributed mainly to the pivot bearing. The noise at 2268 Hz appeared to be from the pivot and the actuator arm that swings across the disk. Those at 3244 Hz and 3384 have similar patterns and were likely due to the disk and VCM. Lastly, the noise at 4868 Hz appeared in the ramp region and the disk edge near SATA.

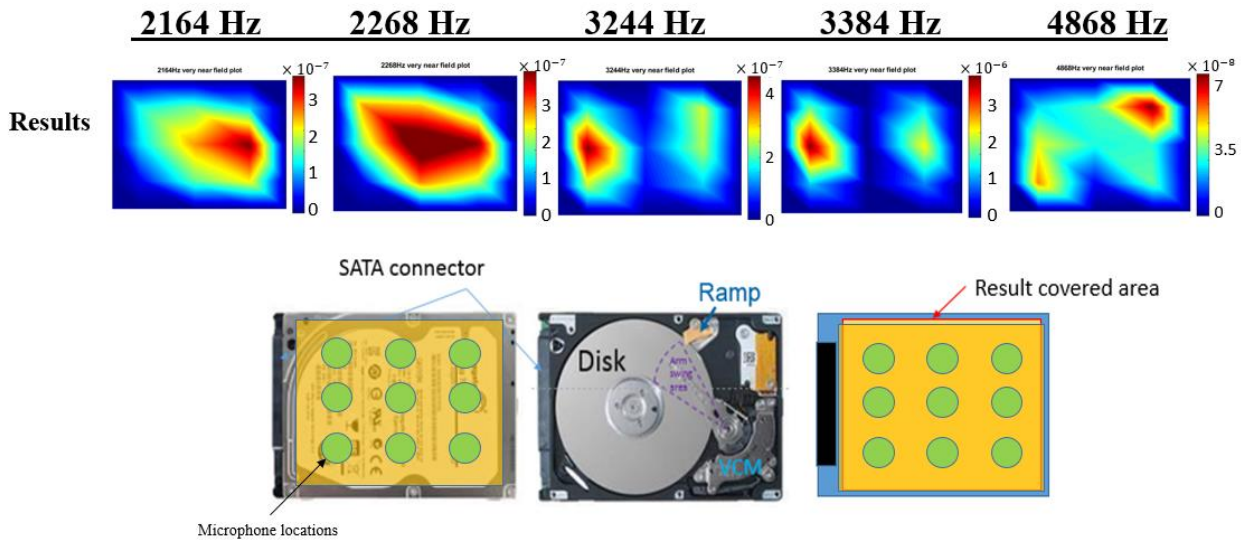


Figure 4-8 Results of 2.5" HDD acoustic measurement at near field

4.2. Numerical solution of Vibro-acoustic Transfer Function

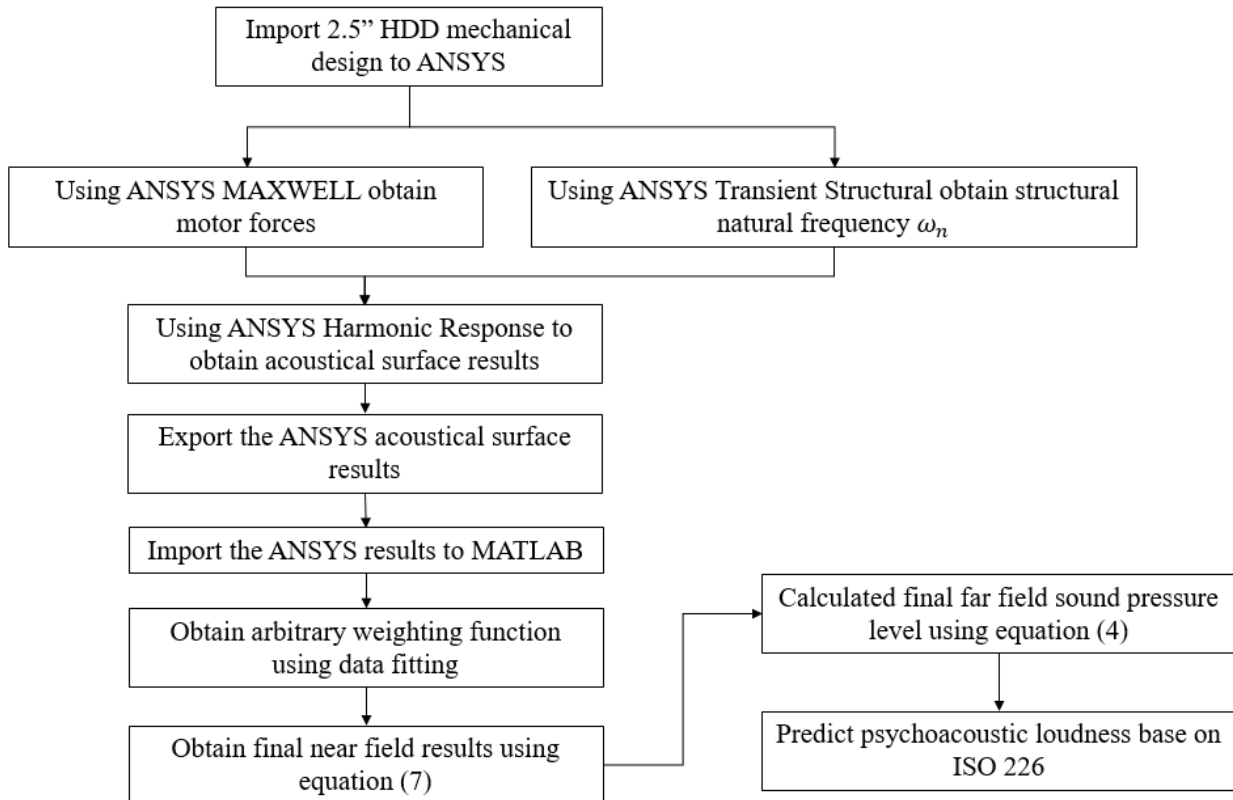


Figure 4-9 Flowchart of the psychoacoustic loudness computation for HDD random write/read via VaTF

Figure 4-9 shows the flow of this section. It starts with Near field simulation.

4.2.1. Near field simulation

The finite element analysis (FEA) is the standard method used for HDD vibration (Jang et al., 2006, Lim et al., 2014). This study adopted the same method.

In the FEA simulation used in this thesis, a 10-node tetrahedral acoustic element was used (Figure 4-10).

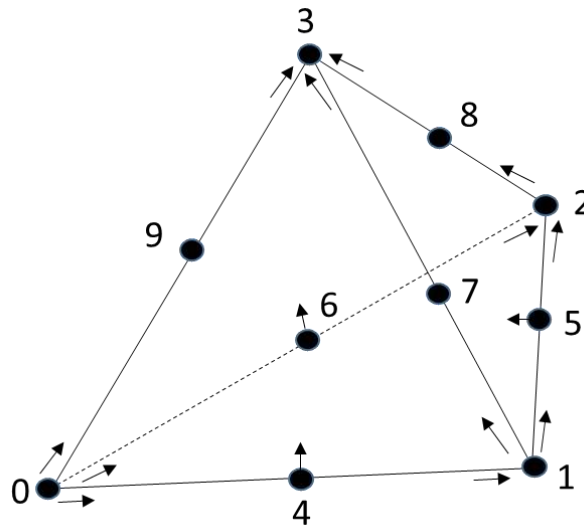


Figure 4-10 Schematic of a 10-node tetrahedral acoustic element

The FEM model of the HDD VCM and the spindle motor were constructed based on equation (61) and (62) using ANSYS Maxell.

Table 4-1 and Table 4-2 presents the magnetic and material properties used in the 2.5” HDD simulation.

Table 4-1 Magnetic properties used in simulation for motor force calculation

<i>Item</i>		<i>Magnetic property</i>
<i>Residual induction Br(G)</i>		<i>13200~13700</i>
<i>Coercive Force</i>	<i>bHc (Oe)</i>	<i>12550</i>
	<i>IHc (Oe)</i>	<i>16000</i>
<i>Maximum Energy Product (BH)max(MGOe)</i>		<i>41.5~46</i>
<i>Recoil Permeability (μr)</i>		<i>1.05</i>
<i>Magnetizing Field (Oe)</i>		<i>>25000</i>

Table 4-2 the material properties of the component for the HDD simulation

<i>Component</i>	<i>Material</i>	<i>Young's modulus (GPa)</i>
<i>Base</i>	<i>Aluminum alloy</i>	<i>71</i>
<i>Cover</i>	<i>Stainless steel</i>	<i>193</i>
<i>HSA</i>	<i>Stainless steel</i>	<i>193</i>
<i>Stator</i>	<i>Stainless steel</i>	<i>193</i>
<i>VCM poles</i>	<i>Magnetism material</i>	<i>150</i>
<i>Disk</i>	<i>Glass</i>	<i>83</i>

The design of the 2.5" HDD spindle motor and VCM were imported to ANSYS Maxwell (as shown in Figure 4-11 and Figure 4-12).

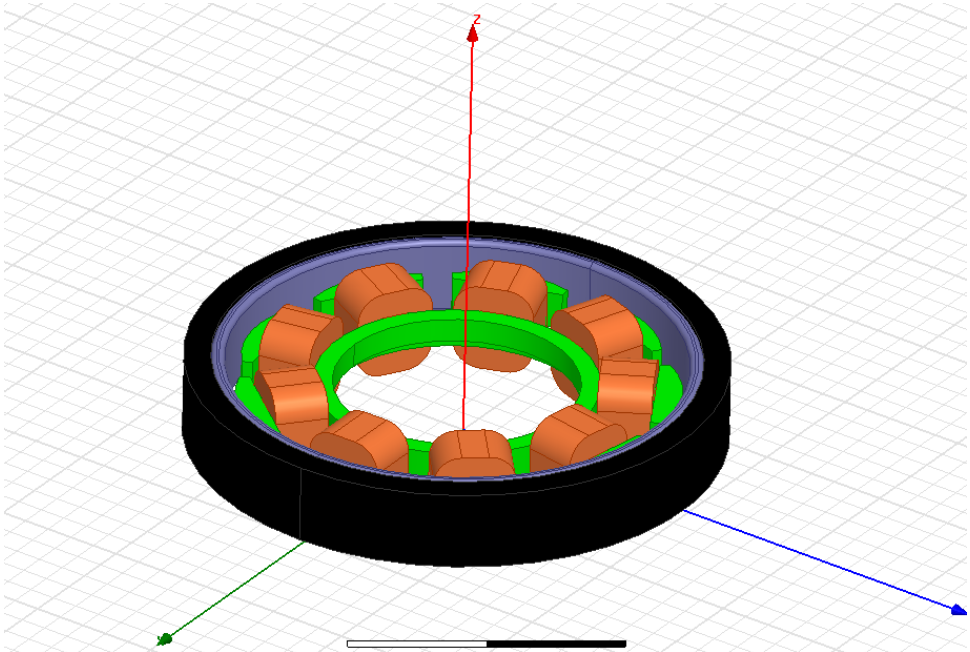


Figure 4-11 ANSYS Maxwell for the 2.5" HDD spindle motor

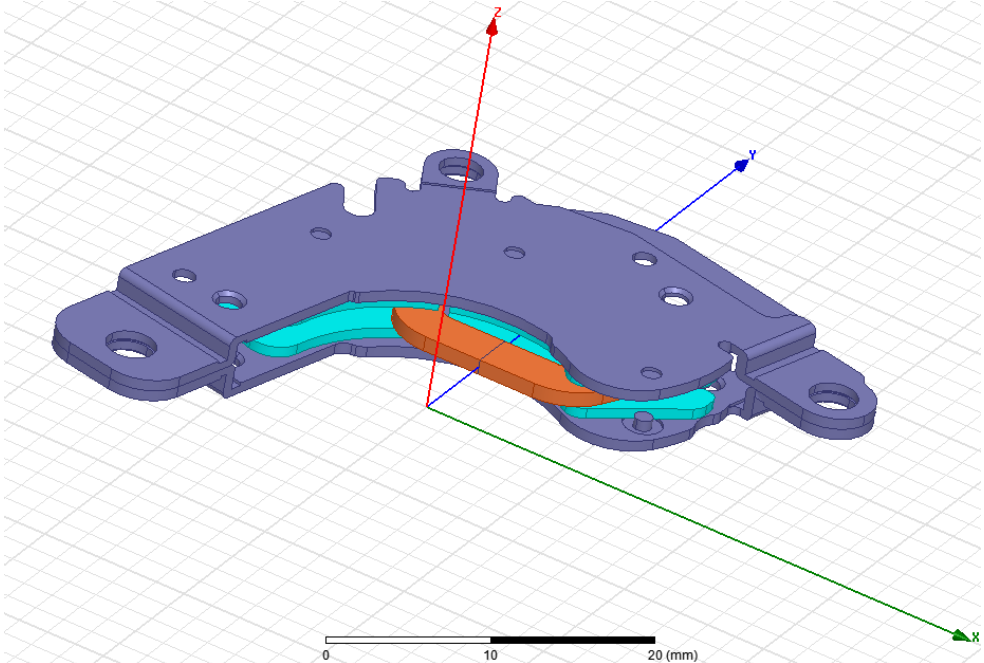


Figure 4-12 ANSYS Maxwell for the 2.5" HDD VCM

After input with magnet and material property, the forces have been calculated for the VCM and the spindle motor and the values are showed in Table 4-3. The spindle motor force at 3244 Hz is similar to the result obtained by Park’s team without eccentricity (Park et al., 2013). As for 2164 Hz, 2268 Hz, 3384 Hz and 4868 Hz, the spindle motor forces were negligible.

Table 4-3 HDD spindle forces at different frequencies in the z-direction.

	<i>Spindle motor</i>	<i>VCM</i>
<i>Frequency. (Hz)</i>	<i>Fz (mN)</i>	<i>Fz (mN)</i>
<i>2164</i>	<i>5.30×10^{-20}</i>	<i>-48.4</i>
<i>2268</i>	<i>2.60×10^{-18}</i>	<i>-48.4</i>
<i>3244</i>	<i>0.05951</i>	<i>-48.4</i>
<i>3384</i>	<i>1.30×10^{-10}</i>	<i>-48.4</i>
<i>4868</i>	<i>3.30×10^{-15}</i>	<i>-48.4</i>

A 3D structural FEM model was built to compute the natural frequency (ω_n) for all the components of an HDD, which are shown in Figure 4-13 to Figure 15.

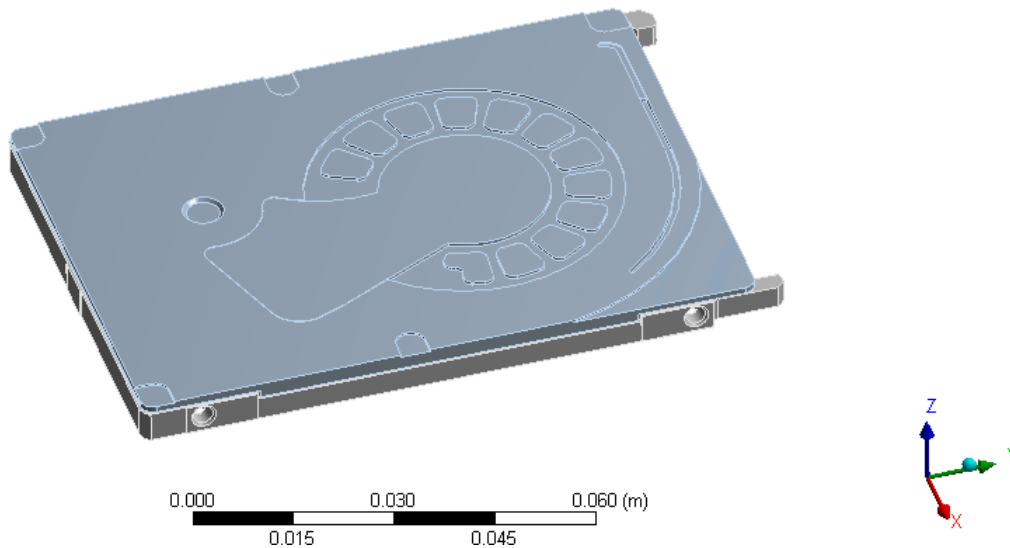


Figure 4-13 ANSYS Transient Structural for 2.5" HDD component - Stationary parts

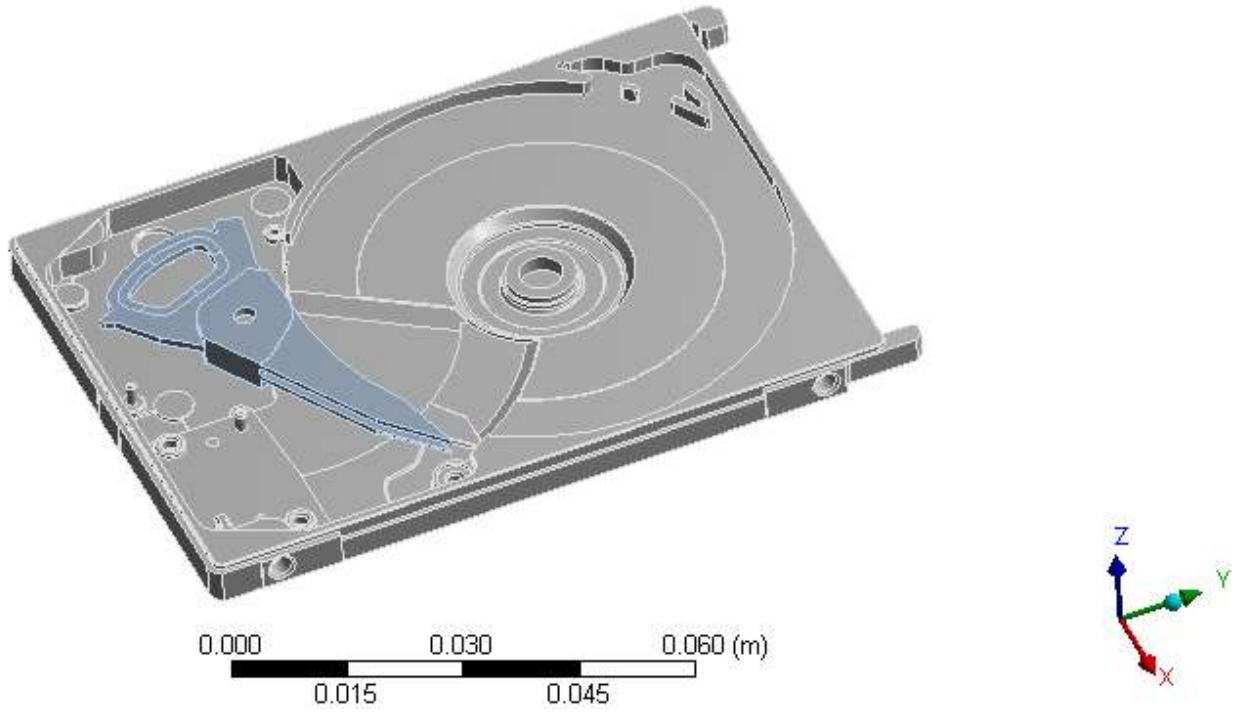


Figure 4-14 ANSYS Transient Structural for 2.5" HDD component - HSA

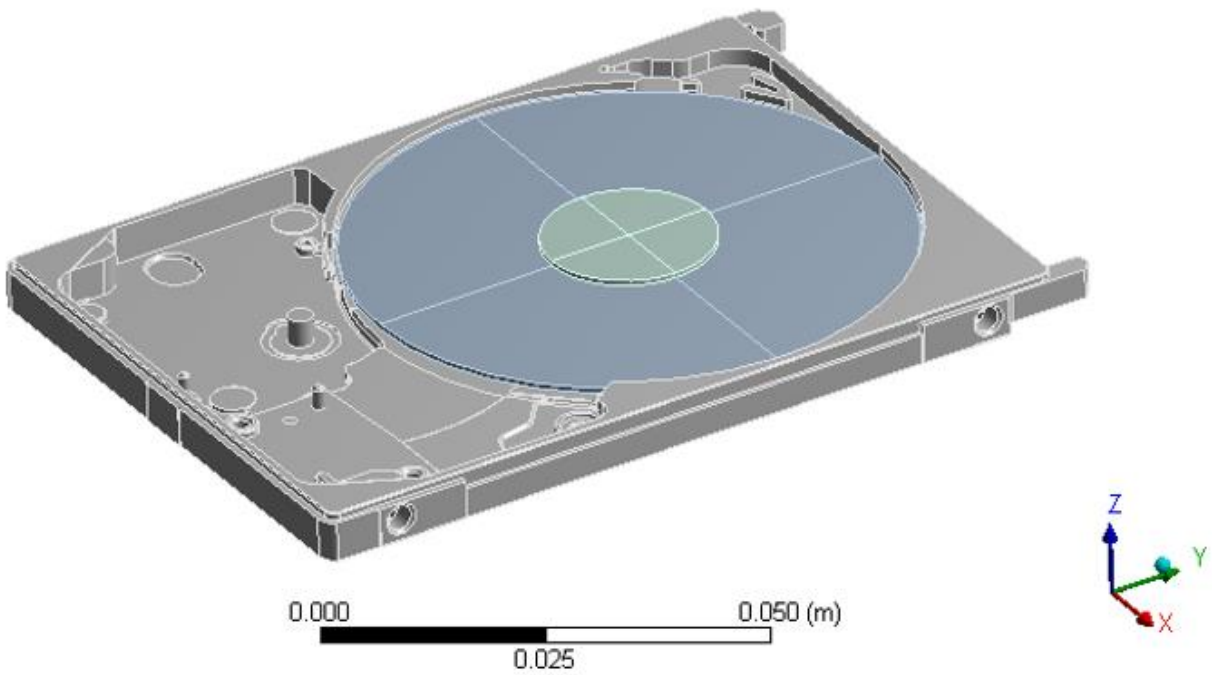


Figure 4-15 ANSYS Transient Structural for 2.5" HDD component - Rotating Disk

To set the boundary conditions closest to the experiment, four fixed supporters were added below the base of the HDD at the same locations of the four dampers used in the experiment (see arrows in Figure 4-16). The HSA and the rotating disk were mounted onto the base, and their modes were computed by individual simulations without including the base. The modes of the other stationary parts were then computed in another simulation. The calculated structural mode frequencies of the corresponding mode shapes are shown in Table 4-4.

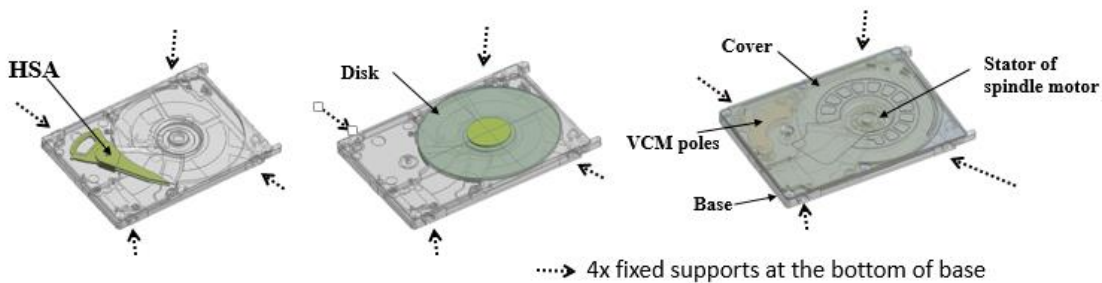


Figure 4-16 The boundary condition of the components used in simulation

Table 4-4 FEM calculated natural frequency with respect to its corresponding model shape

	Mode	Frequency (Hz)
Rotating Disk at 5400 rpm	Disk [0,2] BPM*	1232
	Disk [0,2] FPM*	1592
	Disk [0,3] BPM*	1971
	Disk [0,3] FPM*	2551
	Disk [0,4] BPM*	3246
Stationary parts	1st mode (Base)	865
	2nd mode (Cover)	1225
	Spindle rocking	780
	Base bending	873
	Base bending Spindle side	1533
	Base 2nd bending	2143
Head Stack Actuator (HSA)	HSA Rocking	1425
	Arm bending	1945

*BPM: backward propagation mode; FPM: forward propagation mode

The acoustic pressure p within one finite element can be expressed as

$$p = \sum_{i=1}^m N_i p_i$$

where N_i is a set of linear shape functions, p_i is the acoustic nodal pressure at node i and m is the number of nodes forming the element.

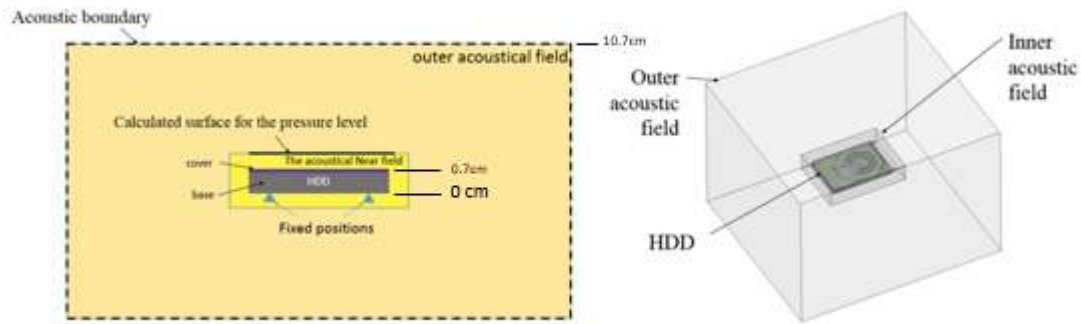


Figure 4-17 A Schematic diagram of the FEM setup

The HDD was surrounded by a 1-cm layer of air, which served as the inner acoustical field. The surface for which the sound pressure was calculated was therefore 1 cm above the HDD surface. An outer acoustic boundary was set such that the sound energy from the sound source would not be reflected. A few trial studies were conducted using different outer field sizes, but the results showed no significant difference except that the computing time was longer if a larger outer field was used. Hence, in order to minimize the computing resource, the edges of the outer acoustic field were set at 10 cm away from those of the inner field. The final FEM model consists of 65902 nodes and 49503 elements.

At the fixed points, there is zero displacement. At the acoustic boundary, the particular velocity and acoustic pressure are zero. In other words, the boundary conditions are:

$$\begin{aligned} w|_{z=0} &= 0 \\ p|_{z=10.7cm} &= 0 \\ \dot{w}|_{z=10.7cm} &= 0 \end{aligned}$$

Based on the results in Table 4-3, values in Table 4-5 were used as the force input for the ANSYS Harmonic Response simulation on different parts of the HDD, i.e. HSA, Rotating disk and Stationary parts.

Table 4-5 The force input used in the near field simulation

	HSA @ fantail	Rotating disk @ rotor	Stationary parts @ pivot	Stationary parts @ stator
Frequency. (Hz)	Fz (mN)	Fz (mN)	Fz (mN)	Fz (mN)
2164	-48.4	0	48.4	0
2268	-48.4	0	48.4	0
3244	-48.4	0.05951	48.4	-0.05951
3384	-48.4	0	48.4	0
4868	-48.4	0	48.4	0

Figure 4-18 to Figure 4-20 showed locations at which the Z-directional forces were applied to different HDD components at the location specified in Table 4-5.

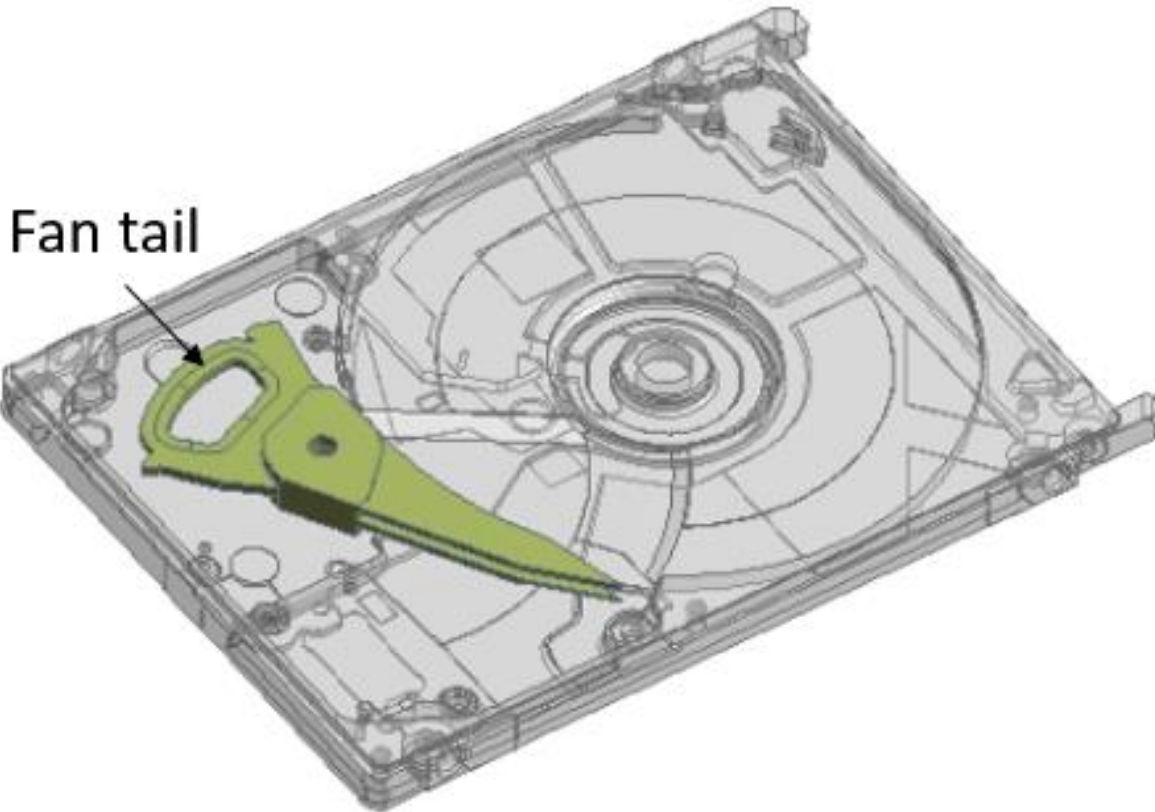


Figure 4-18 Z-directional forces location for 2.5" HDD HSA

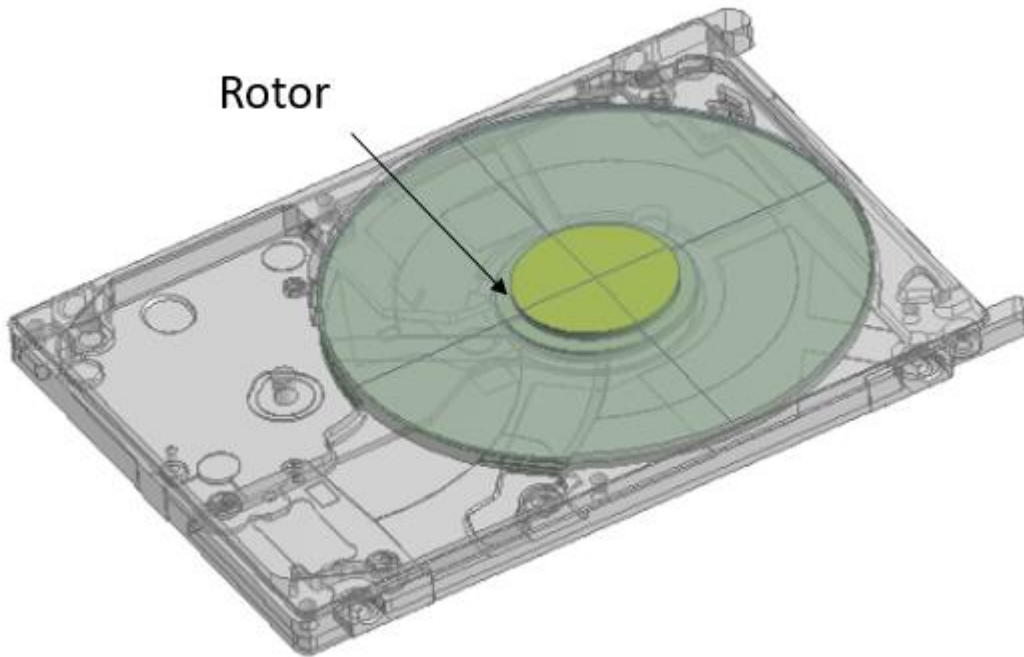


Figure 4-19 Z-directional forces location for 2.5" HDD Rotating Disk

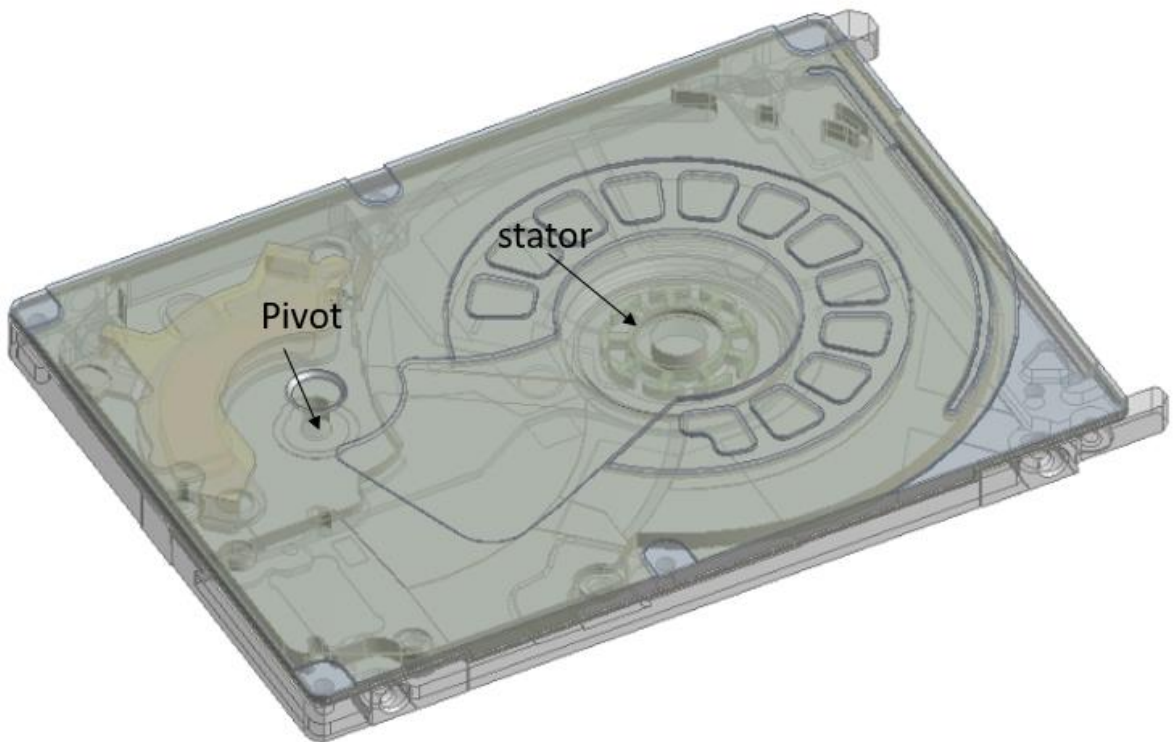


Figure 4-20 Z-directional forces location for 2.5" HDD Stationary Parts

With the forces applied to the components, the ANSYS Harmonic Response simulations were then setup (showed in Figure 4-21 to figure 4-24).

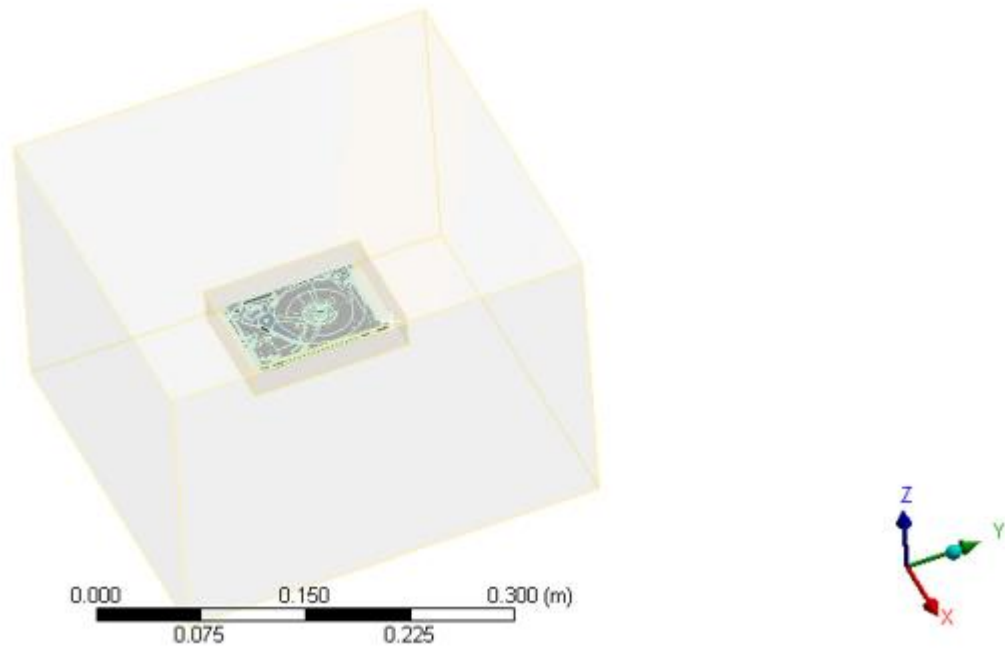


Figure 4-21 ANSYS Harmonic Response simulation for 2.5" HDD HSA

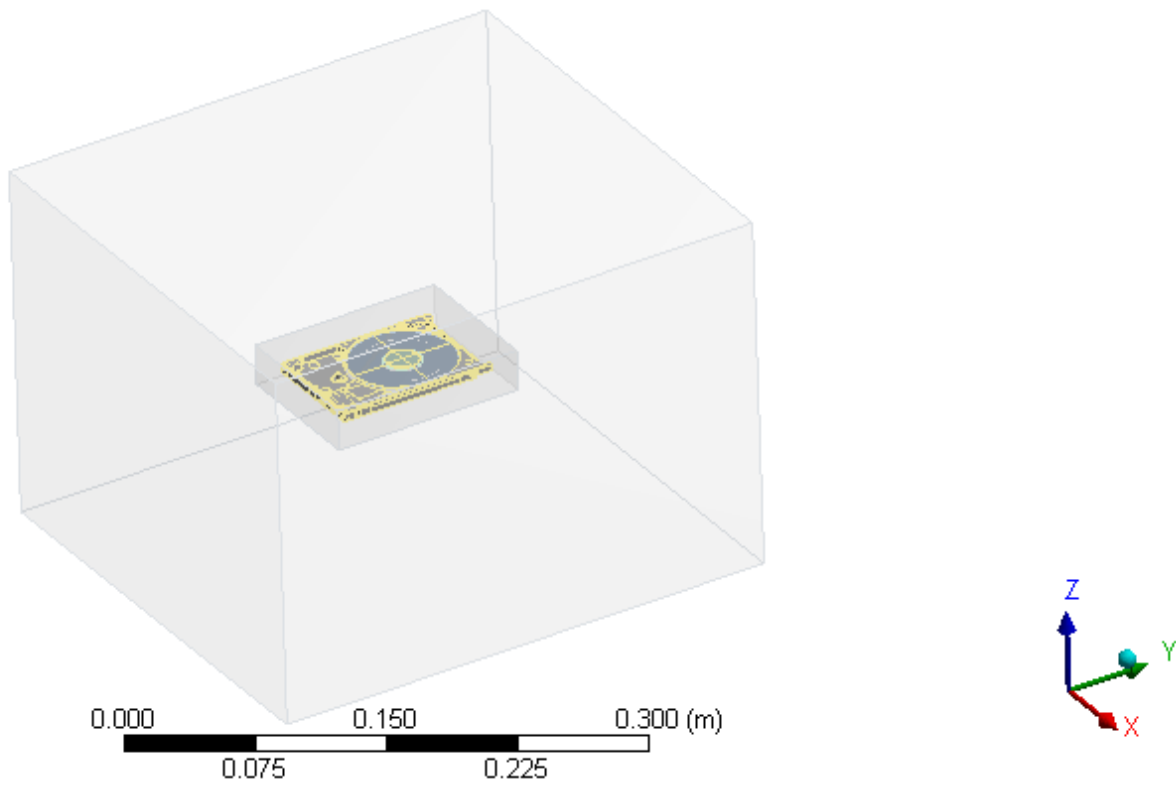


Figure 4-22 ANSYS Harmonic Response simulation for 2.5" HDD Rotating disk

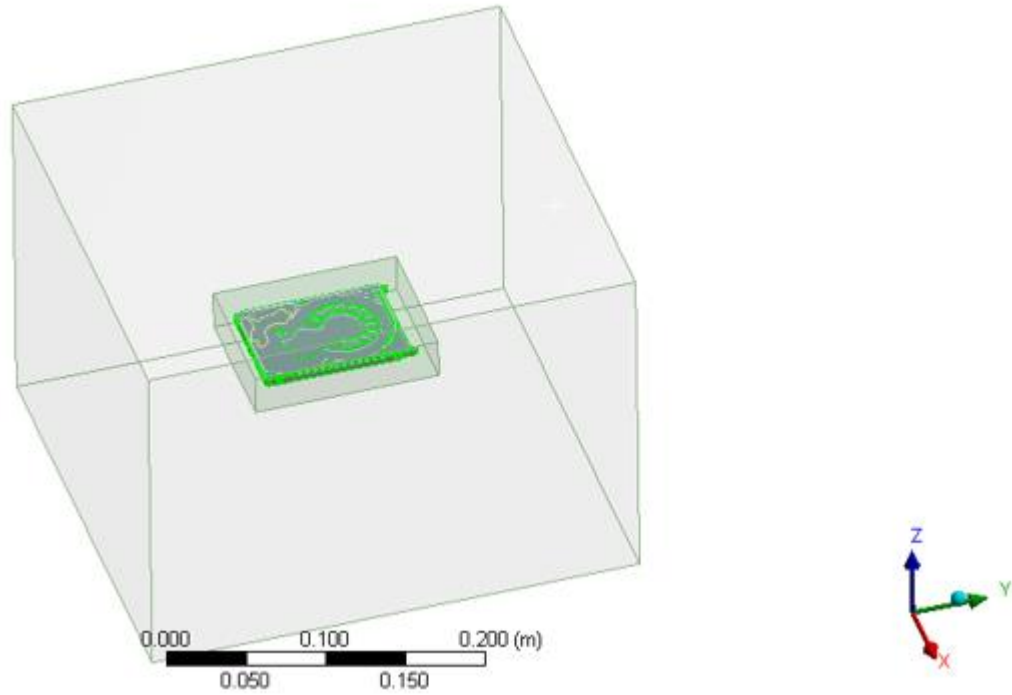


Figure 4-23 ANSYS Harmonic Response simulation for 2.5" HDD Stationary Parts

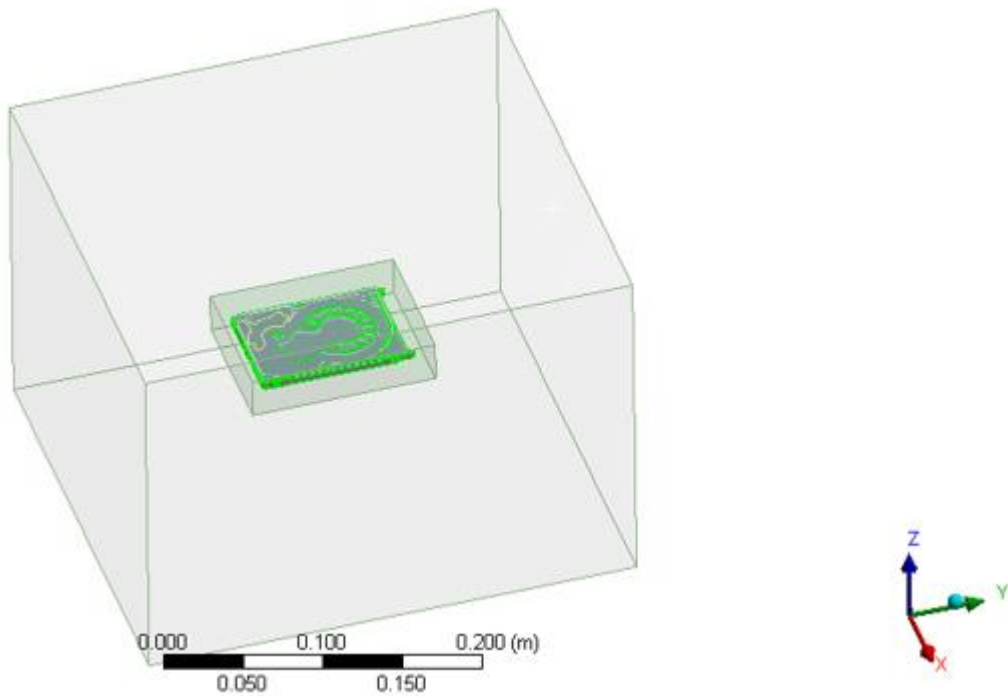


Figure 4-24 ANSYS Harmonic Response simulation for 2.5" HDD Two Point Sources

Figure 4-25 to Figure 4-28 shows the typical results of the near field acoustic behaviours of each component.

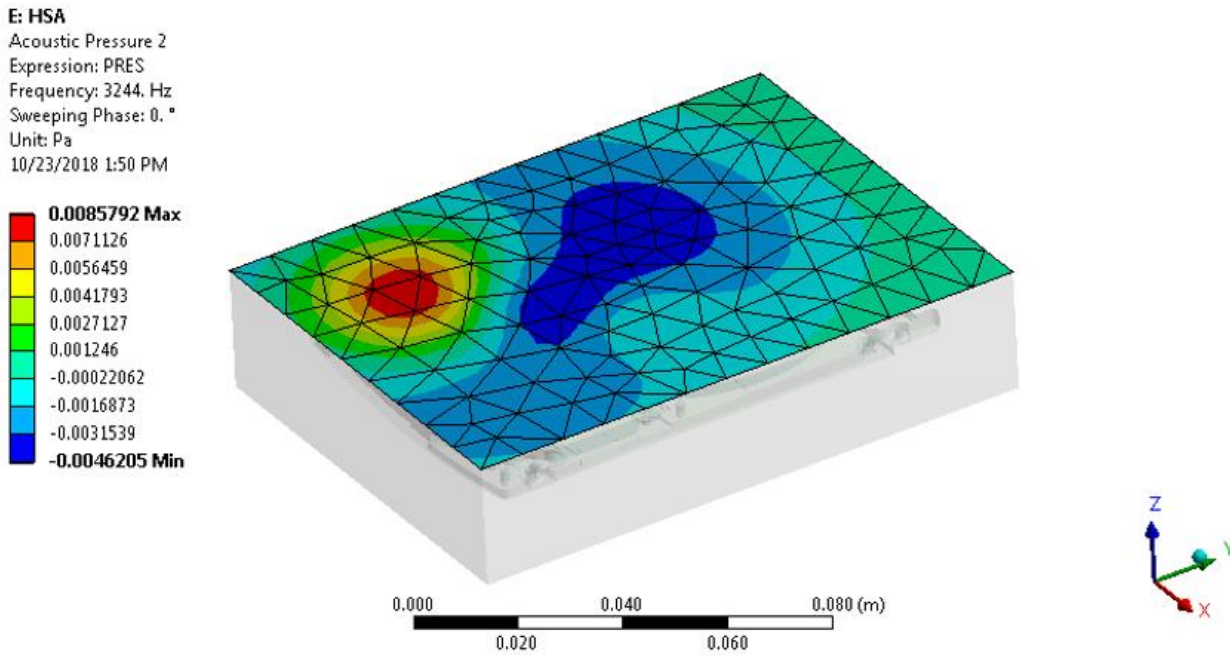


Figure 4-25 Typical examples of Sound pressure at near field for difference 2.5" HDD HSA

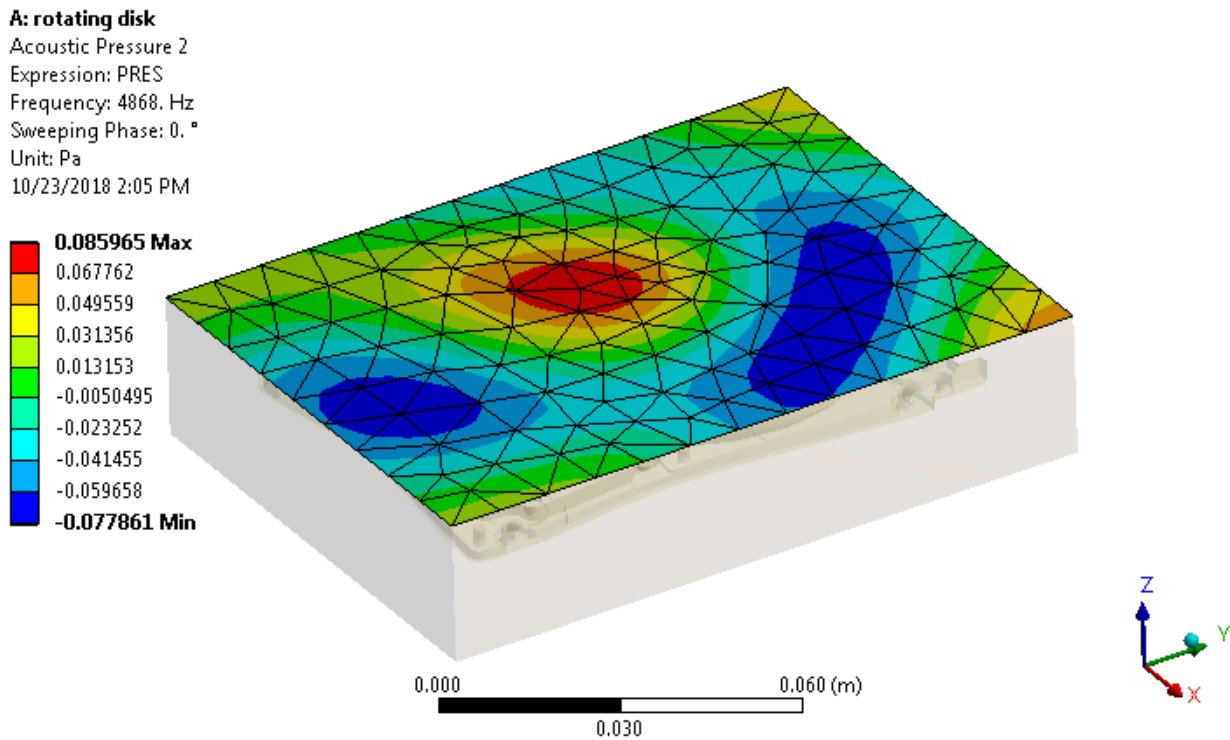


Figure 4-26 Typical examples of Sound pressure at near field for difference 2.5" HDD Rotating disk

B: Stationary parts
 Acoustic Pressure 5
 Expression: PRES
 Frequency: 4868. Hz
 Sweeping Phase: 0. °
 Unit: Pa
 10/23/2018 3:08 PM

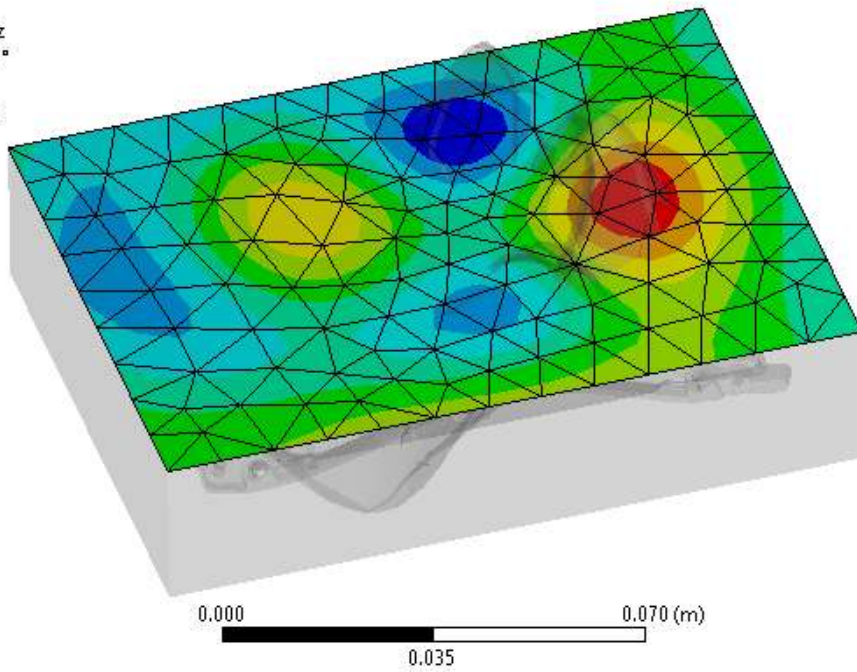
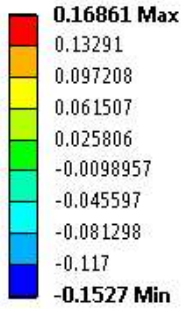


Figure 4-27 Typical examples of Sound pressure at near field for difference 2.5" HDD Stationary Parts

K: two point sources
 Acoustic Pressure 2
 Expression: PRES
 Frequency: 3244. Hz
 Sweeping Phase: 0. °
 Unit: Pa
 10/23/2018 2:13 PM

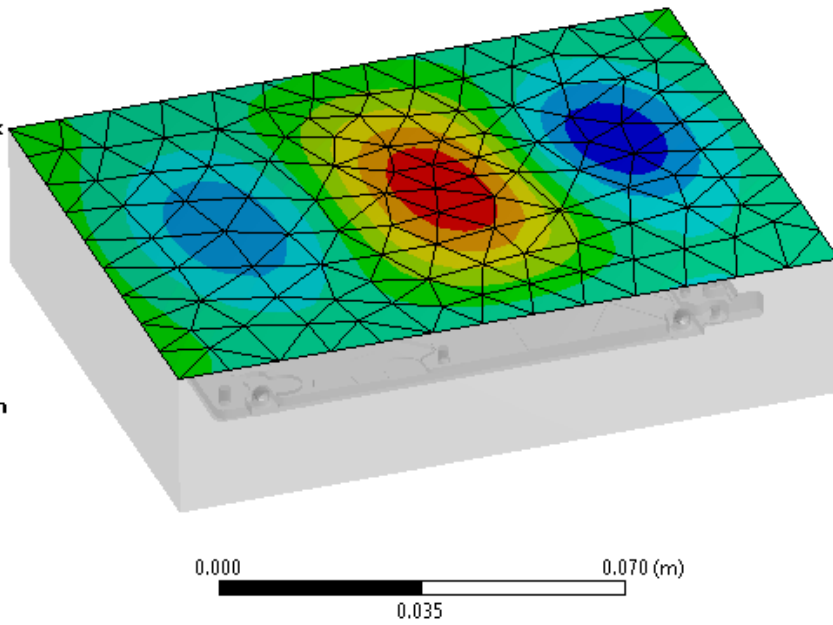
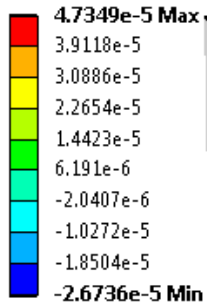


Figure 4-28 Typical examples of Sound pressure at near field for difference 2.5" HDD Two Point Sources

As shown in Figure 4-22 to 4-25, the calculated plate is bigger than the size of a 2.5” HDD, making the direct comparison to the experimental results difficult. Hence, the simulation results were exported from ANSYS and imported to MATLAB. A data fitting process was then carried out by comparing the simulation result with the experimental results (Figure 4-8) to determine the value of the arbitrary weighting function. The arbitrary weighting function values are summarized in Table 4-6. As shown in Table 4-6, the value of A, B, C and D are frequency dependent. Hence, the arbitrary weighting functions are frequency dependent polynomial.

Table 4-6 Arbitrary weighting function value for A, B, C and D

	A	B	C	D
2164 Hz	3.61×10^3	7.10×10^{-7}	N.A	3.33×10^{-6}
2268 Hz	2.44×10^4	4.84×10^{-6}	N.A	2.93×10^{-6}
3244 Hz	6.39×10^2	2.74×10^{-7}	5.33×10^{-4}	7.62×10^{-4}
3384 Hz	1	9.43×10^{-5}	N.A	1.00×10^{-5}
4868 Hz	22.8	5.65×10^{-6}	N.A	2.52×10^{-5}

From the values displayed in Table 4-6, a fourth order frequency dependent polynomial was obtained using curve fitting; Figure 4-29 shows the curve fitting for the arbitrary weighting function, A

$$A = -7 \times 10^{-8}f^4 + 0.001f^3 - 4.8221f^2 + 10419f - 8 \times 10^6$$

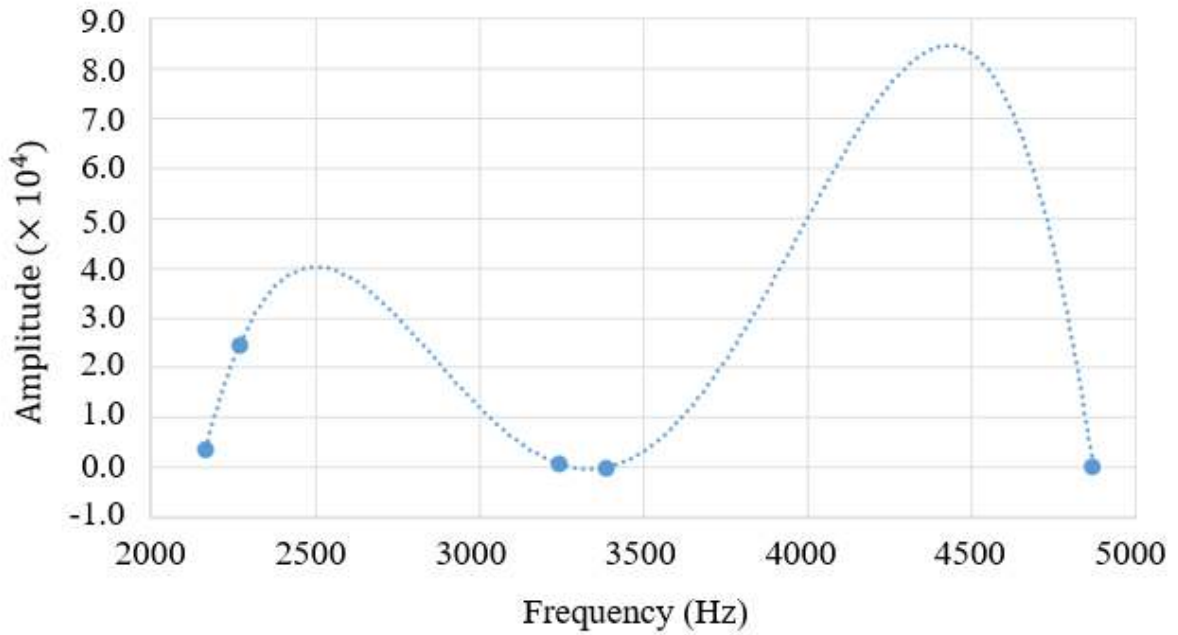
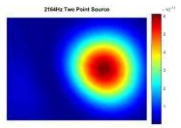
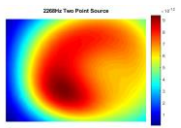
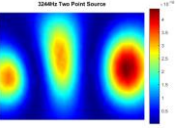
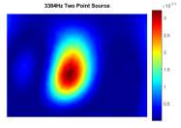
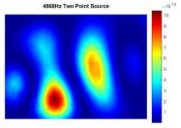
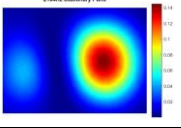
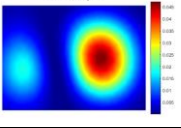
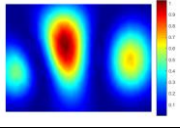
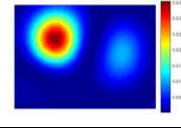
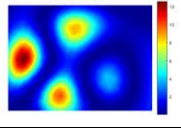

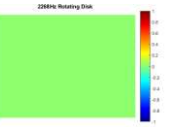
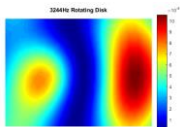

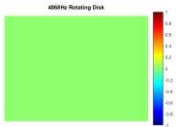
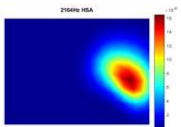
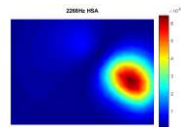
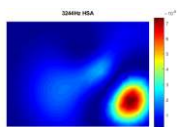
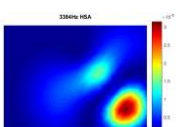
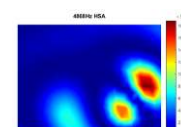
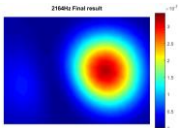
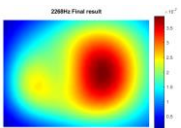
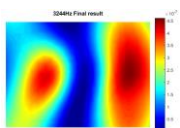
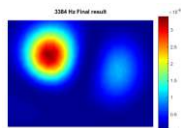
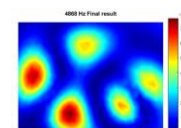


Figure 4-29 Identification of arbitrary weight function, A using curve fitting method

Similarly, all other arbitrary weighting functions can be obtained using this approach. However, these arbitrary weighting functions will be incomplete based on the current data and they will not cover the whole measured frequency range, which is from 1000 Hz to 10 KHz.

Hence, the total sound pressure was calculated using equation (7). The results are shown in Table 4-7.

Table 4-7 FEM results component level and final results

	2164 Hz	2268 Hz	3244 Hz	3368 Hz	4868 Hz
Two point sources					
Stationary parts					
Rotating disk					
HSA					
Final results					

4.2.2. Far field sound pressure prediction

Recall Equation (4) for the far field sound pressure calculation:

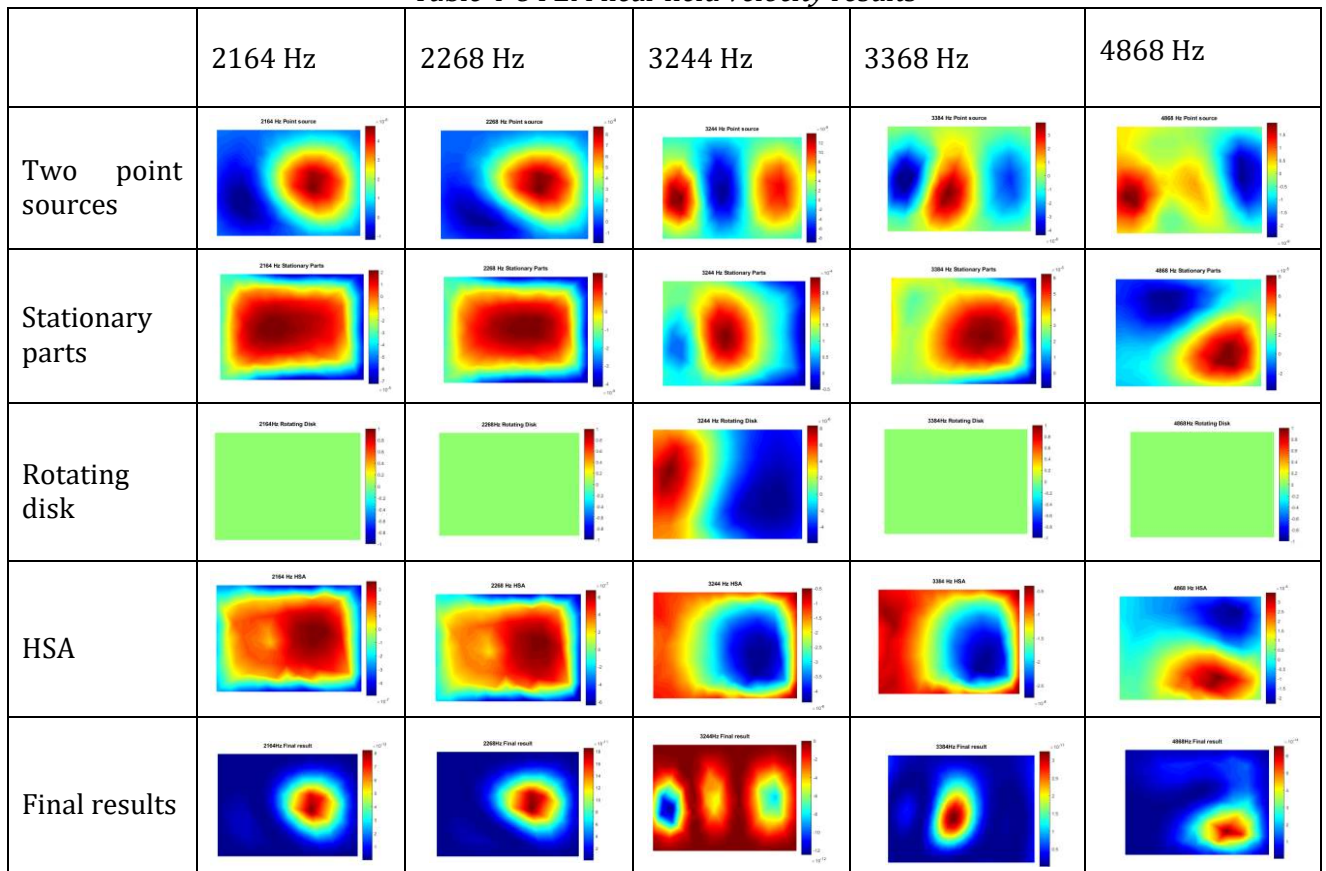
$$p(x, y, z) = \frac{j\rho ck}{2\pi} \int_S v_p(x, y) \frac{e^{-jkR}}{R} dS$$

Base on the far field measurement conditions and setup, the parameters in the above equation were identified as $\rho = 1.1839 \text{ kg/m}^3$ and $c = 346.13 \text{ m/s}$.

In the above equation, $v_p(x, y)$ is the normal velocity of a vibrating plate. In this simulation, this value was approximated to be the total near field normal velocity of the calculated surface (Figure 4-9). Using the FEM modal and procedure similar to Section 4.2.1, the normal velocities of each component at different frequencies were calculated. The value arbitrary

weighting functions (showed in Table 4-6) were then used to calculate the total near field normal velocities. The results are shown in Table 4-8.

Table 4-8 FEM near field velocity results



Finally, the far field sound pressures at each frequency were calculated using Equation (4). The results are shown in Table 4-9

Table 4-9 Computed far field sound pressure level computation results base on velocity data

Frequency (Hz)	Sound Pressure (Pa ²)	SPL (dB)
2164	9.19×10^{-10}	3.63
2268	6.85×10^{-10}	2.36
3244	1.76×10^{-9}	6.45
3384	3.23×10^{-9}	9.10
4868	5.83×10^{-10}	1.66

4.2.3. Far field psychoacoustic loudness prediction

The psychoacoustic loudness at far field based on the far field sound pressure (Table 4-9) could be calculated using the formula from ISO 226 (ISO 226:2003).

$$L_N = (40 \cdot \lg B_f)_{phon} + 94_{phon} \quad (124)$$

where

$$B_f = \left[0.4 \times 10^{\left(\frac{L_P - L_U}{10} - 9\right)} \right]^{\alpha_f} - \left[0.4 \times 10^{\left(\frac{T_f - L_U}{10} - 9\right)} \right]^{\alpha_f} + 0.005135,$$

T_f is the threshold of hearing, α_f is the exponent for loudness perception, and L_U is a magnitude of the linear transfer function normalized at 1000 Hz.

Since 2164 Hz and 2268 Hz are close in frequency, they are perceived to be within the same bandwidth. Similarly, 3244 Hz and 3384 Hz are perceived within another same bandwidth. The highest sound pressure level was used for each bandwidth. As a result, the total loudness level was computed as 0.441 Sone.

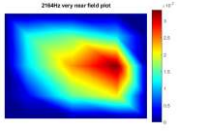
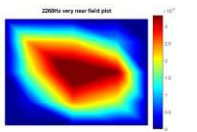
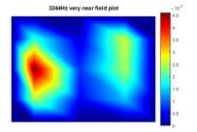
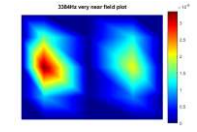
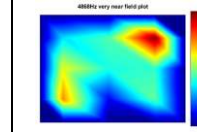
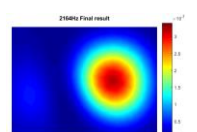
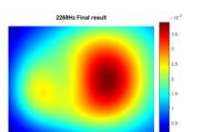
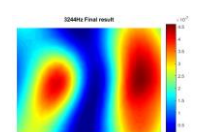
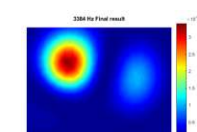
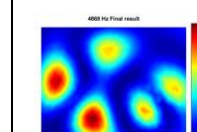
4.3. Result and discussion

4.3.1. At the source

As in Table 4-10, similarities were found between the results obtained from the near field experimental measurements and the FEM simulation. Comparison was done by computing the similarity index of the two sets of images using MATLAB. For 2164 Hz and 3368 Hz, the similarity is as high as 57%, and for 2268 Hz and 4868 Hz, the similarity is greater than 45%. The difference, however, was likely to be caused by the spatial separation between the microphones. Nine ½" microphones were used in this measurement, resulting in certain space in between. Smaller microphones could have been used (such as ¼" microphones) to reduce the separation, but they tend to have undesirable higher self-noise. On the other hand, the 2.5" HDD has an overall size of 10 cm by 7 cm. The currently used microphone array was regarded the best arrangement to cover all the moving and flexible parts in the HDD (Figure

4-30). At the receiver end, the main aim of measuring the acoustic pressure at the source plane is to identify the arbitrary weighting functions used in equation (7) and subsequently use equation (7) for the far field acoustic pressure computation. In this sense, the FEM simulation presented here can provide a relative good prediction to the actual near-field acoustic behavior of HDD at the early design stage.

Table 4-10 FEM vs. measurement results

	2164 Hz	2268 Hz	3244 Hz	3368 Hz	4868 Hz
Measurement result					
FEM result					

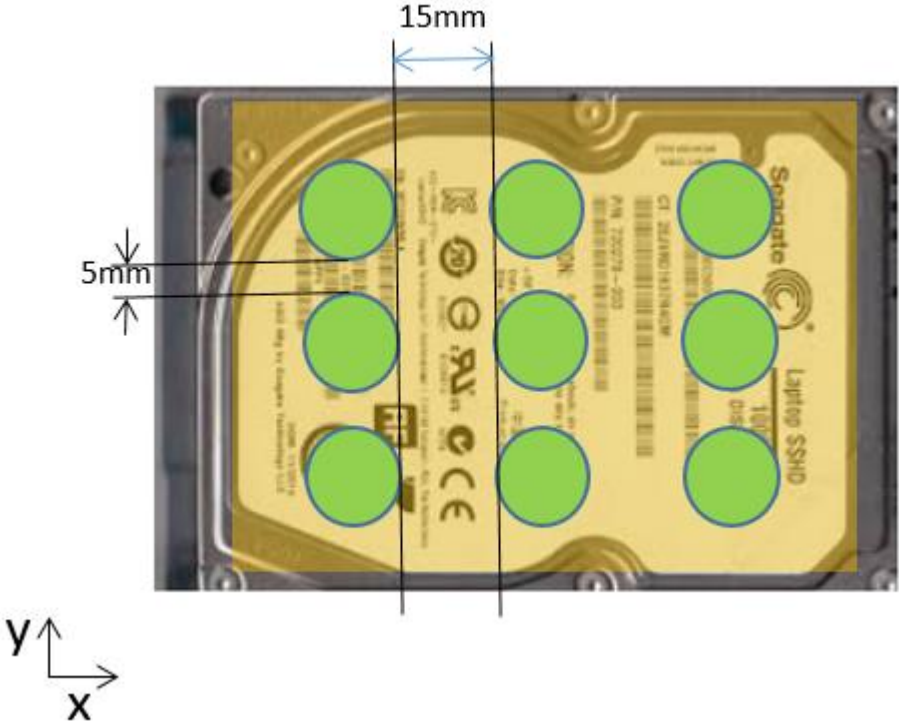


Figure 4-30. Microphone locations on top of the HDD measured

4.3.2. At the receiver

Table 4-11 shows the comparison between sound pressures obtained from the far field measurement and the FEM predictions. The difference in SPL was less than 3 dB for all frequencies. Figure 4-31 shows the fitting to the linear correlation, which has R^2 of 92.6%. This indicates that the setup and procedure used in the near field measurement was sufficiently good to identify the correct A, B, C and D as the arbitrary weighting functions for equation (7).

Table 4-11 Result comparison: far field measurement vs. FEM result

Frequency (Hz)	Sound Pressure (Pa^2)		SPL (dB)	
	Measured result	FEM result	Measured result	FEM result
2164	5.12×10^{-10}	9.19×10^{-10}	1.1	3.63
2268	6.21×10^{-10}	6.85×10^{-10}	1.9	2.36
3244	1.55×10^{-9}	1.76×10^{-9}	5.9	6.45
3384	2.39×10^{-9}	3.23×10^{-9}	7.8	9.10
4868	4.80×10^{-10}	5.83×10^{-10}	0.8	1.66

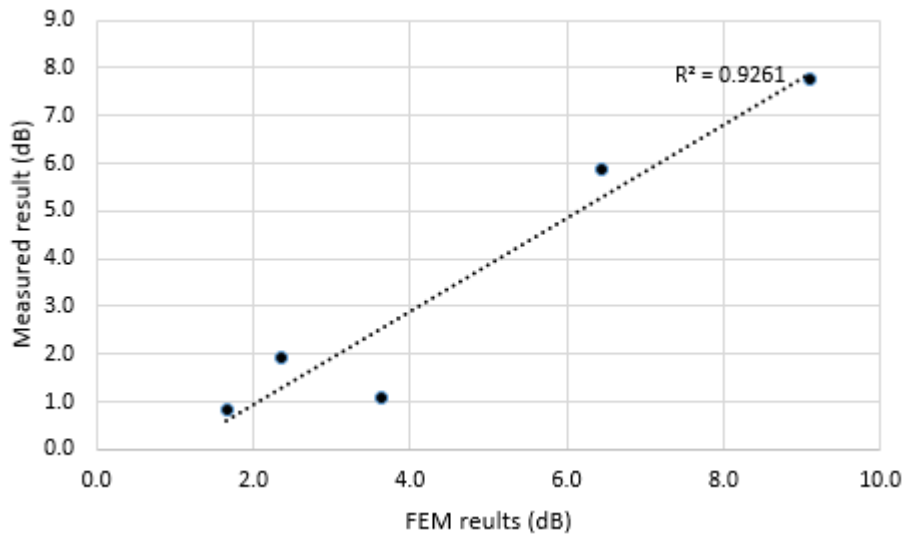


Figure 4-31 Linear correlation study between FEM results and Measured results at the far field

Moreover, with the validation of the far-field acoustic pressure, the hypothesis in this thesis has been tested and confirmed. The total loudness level was computed as 0.441 Sone based on five highest tones, accurately matched the total loudness of 0.41 Sone measured with the binaural head (Sound #7 in Table 2-4). The difference of 0.029 Sone was mainly caused by

other minor tones shown in Figure 4-4. This difference may be reduced by calculation of more tones.

Furthermore, if one wants to design an HDD with a desirable loudness level, the following steps may be taken to achieve the target.

- 1) Using the equation from ISO 226 (ISO 226:2003) to obtain the target sound pressure level at the receiver end from the desired loudness level.

$$L_p = \left(\frac{10}{\alpha_f} \cdot \lg A_f \right) dB - L_U + 94dB$$

where

$$A_f = 4.47 \times 10^{-3} \times (10^{0.025L_N} - 1.15) + \left[0.4 \times 10^{\left(\frac{T_f + L_U}{10} - 9 \right)} \right]^{\alpha_f},$$

T_f is the threshold of hearing, α_f is the exponent for loudness perception, and L_U is a magnitude of the linear transfer function normalized at 1000 Hz.

- 2) Study the mechanical design of the HDD to understand the mechanical design constraint.
- 3) Redesign the HDD components that have lower or no design constraint and use the FEM simulation at near field and Rayleigh's integral to calculate the far field pressure.
- 4) Run a few iterations until the target sound pressure level at receiver end is met.

Chapter 5. Conclusions and Future Work

This chapter summarized the major contributions in this thesis and suggests some future works.

5.1. Conclusions and contributions

This thesis presents a systemic solution for establishing the relationship between human annoyance perception and the 2.5" HDD structural vibration. To achieve this, two complementary objectives have been achieved: 1) to examine the relationship between psychoacoustic metrics and the annoyance perception, and 2) to predict the far field sound pressure level from the 2.5" HDD vibrating body. This approach can be applied not only to 2.5" HDD but also to any household and office electrical and mechanical products, such as gaming consoles, air-conditions, washing machines, and personal computers. The potential contributions are the following:

1. Provided a complete derivation of the VaTF formulation for the 2.5" HDD dynamics, near field acoustics and far field predictions (Chapter 3). Numerical solutions to the VaTF of the HDD random write/read operations was obtained by FEM simulation using ANSYS (Chapter 4). The numerical results showed promising level of correlation (of ~ 60% similarity index) with the experimental results at the near field. It shows that the analytical model of near-field acoustics can be used to determine the acoustic pressure of the HDD. Through near field normal velocity, the far field sound pressures can be predicted. A good correlation with the measurement results was obtained. This proves the validity of the assumptions stated in Section 3.1: a complex system like a 2.5" HDD can be split into different components, and the analysis can be done using the wave superposition method. Moreover, only the relatively large components (e.g. the disk, cover, base and HSA) need to be considered. Other factors such as air flow in the HDD due to disk rotation, or small components like ramp and print circuit board, are insignificant in affecting the acoustic performance at near field and far field.

- 2. Develop a comprehensive model to predict human perception from the 2.5" HDD vibrations (Chapter 2).** The findings can benefit the HDD industry and manufacturers to understand the noise control of 2.5" HDDs. The results indicated when the noise level is lower than 30 dB(A) the relationship between psychoacoustic metrics and noise annoyance is non-linear. Neural network model was developed to predict the noise annoyance, which showed good agreement between the predict values and the jury test results. On the other hand, using the simulation developed in Chapter 4, 2.5" HDD dynamics can be used to calculate the far field sound pressure data. Using such data, one can then compute the psychoacoustic metrics and use these values to predict the human acoustic perception of the HDD noise.
- 3. Provided a potential tool to identify the noise source in the 2.5" HDDs (Ma et al., 2017).** When the size of a very complex device gets smaller, such as in the case of a 2.5" HDD, identifying the source of its noise becomes difficult. This is a challenging problem for acoustic engineers in HDD noise treatment. The near field acoustic measurement setup described in this thesis provided a good solution. It allows the plotting of a graphical distribution of noise using measurement data. With such direct visualization, acoustic engineers can easily diagnose and treat noise failures in HDDs. One key element in the NAH measurement is the aluminum fixture, which is rigid and has fixed positions for the microphones. It also has an aligning mechanism that ensures the HDD is always putting at the same orientation. Both features are crucial for consistent measurement and good reproducibility. Although the simulated results and the measured results are not matching perfectly, the observed differences are mainly due to the resolution of the images. To improve this, using a larger number of smaller-sized probes may help.

5.2. Future work

The following future work is recommended:

1. **Continue to work on the emotional state change caused by 2.5" HDD noise.** In Jury Test 2, an emotion change was observed. Other than feeling annoyed, various emotional states were reported by the participants when they listened to low level noise. One interesting observation was also made in Jury Test 2: some participants who felt depressed initially gradually felt better after listening to the low level noise. This indicates that focusing on listening to the low level noise may help people recover from negative feelings. Further investigation will help to better understand this. Furthermore, some psychological treatments using low level noise may be developed to treat human psychological problems.
2. **Further improve the model and establish a single platform solution.** In this thesis, several tools and software (i.e. ANSYS, Excel and MATLAB) were used to show the validity of the FEM simulation. It was however time consuming and less efficient. It will be desirable to use only one platform, such as MATLAB, to achieve this. MATLAB is a preferred platform because it is often used as a servo controller design tool. Integrating the noise simulation into MATLAB will make the noise improvement of HDD design more efficient.
3. **Establish a standard near-field measuring methodology for more efficient and accurate acoustic testing that can be used for factory quality control of HDD noise.** In today's factory quality control of HDD noise, most measurements of sound pressure level are done at the far field. In order to minimize the interference caused by the high background noise in a factory setting, the anechoic chamber often needs to be placed away from the factory site, costing time and money to transport and measure the HDDs. This can be resolved by using the method presented in this thesis, in which the far field signals were estimated with the near field sound pressure level. Any far field noise requirement can now be back extrapolated to a certain near field noise level, which can be used as the quality control standard. Because the sound pressure level of HDD is much higher at the near field than at the far field, the factory background noise will not affect the measurement of the near field signal as much. In addition, the setup can also be assembled into an acoustic box, which reduces the space

requirement for an anechoic chamber. An acoustic box with dimensions of 30 cm × 30 cm × 30 cm will be sufficient for a HDD near field measurement. Moreover, the resolution of the NAH can be further improved by using smaller-sized microphones, or using acoustical sensors such as particle velocity sensors. All these improvements will reduce cost, time and manpower, making the HDD acoustic testing more efficient.

4. **Extend the investigation to lower frequency noise.** The measurements in Chapter 4 made use of sound frequencies higher than 2000 Hz. Based on the dimensions of the setup in Chapter 4 and the definition of far field in Chapter 1, any frequency less than 1372 Hz is within the near field range for the current setup. Further work is needed to validate whether the current method can be used for sound level predication at lower frequency.
5. **Complete the arbitrary weighting functions.** In this thesis, the arbitrary weighting functions have been derived based on data of five frequencies. As a result, we observed a difference of 0.029 Sone between the computational results and the experiment results. To derive a complete arbitrary weighting function, data of more drives and more tones are needed.

5.3. Publications

Published:

MA, Y. C., CHIN, C. S., WOO, W. L. & GAO, B. 2016. An Acoustic Annoyance Study of Hard Disk Drive for Laptop. IEEE Transactions on Magnetics, 52, 1-9.

MA, Y. C., CHIN, C. S. & WOO, W. L. 2015. Neural Networks-Based Acoustic Annoyance Model for Laptop Hard Disk Drive. International Journal of Electrical, Computer, Energetic, Electronic and Communication Engineering, 9.

MA, Y., CHIN, C. S. & WOO, W. L. 2017. Evaluating 2.5" Hard Disk Drive Noise Source Identification. INTER-NOISE and NOISE-CON Congress and Conference Proceedings, 255, 1782-1787.

Submitted:

MA, Y. C., CHIN, C. S., Predicting 2.5" Hard Disk Drive Noise Annoyance using Psychoacoustic Metrics and Subjective Sound Paired-Comparison, International Journal of Product Sound Quality, submitted first revision on Oct 2017.

MA, Y. C., CHIN, C. S., Near-Field Vibro-Acoustic Transfer Function Prediction of Small Close Fit Enclosure with Multiple Rotating Components, Applied Acoustics, submitted in Jan 2018.

Reference

- (WHO), W. H. O. & COPENHAGEN, D. 2009. *Night noise guide lines for Europe* [Online]. [Accessed May 4 2016].
- ANSI-S3.4 2007. Procedure for the Computation of Loudness of Steady Sounds.
- ASTLEY, R. J. & EVERSMA, W. 1978. A Finite Element Method for Transmission in Non-uniform Ducts Without Flow Comparison with the method of Weighted Residuals. *Journal of Sound and Vibration*, 57, 367-388.
- ASUTAY, E., VÄSTFJÄLL, D., TAJADURA-JIMÉNEZ, A. & VÄSTFJÄLL, D. 2012. A study of the psychoacoustical and psychological dimensions of emotional sound design. *J. Audio Eng. Soc.*, 60, 21-28.
- AURES, W. 1985. Method for Calculating Auditory Roughness. *Acustica*, 58, 268-281.
- BABISCH, W., HOUTHUIJS, D., PERSHAGEN, G., CADUM, E., KATSOUYANNI, K., VELONAKIS, M., DUDLEY, M. L., MAROHN, H. D., SWART, W., BREUGELMANS, O., BLUHM, G., SELANDER, J., VIGNA-TAGLIANTI, F., PISANI, S., HARALABIDIS, A., DIMAKOPOULOU, K., ZACHOS, I., JARUP, L. & CONSORTIUM, H. 2009. Annoyance due to aircraft noise has increased over the years--results of the HYENA study. *Environ Int*, 35, 1169-76.
- BAEK, J. P. S. J. E. K. H. 1999. Analysis of Low Frequency Acoustic Response in a Damped Rectangular Enclosure. *J. Sound Vib.*, 543-566.
- BAI, M. R. 1992. Application of BEM (boundary element method) - based acoustic holography to radiation analysis of sound sources with arbitrarily shaped geometries. *The Journal of the Acoustical Society of America*, 92, 533-549.
- BASNER, M., BABISCH, W., DAVIS, A., BRINK, M., CLARK, C., JANSSEN, S. & STANSFELD, S. 2014. Auditory and non-auditory effects of noise on health. *The Lancet*, 383, 1325-1332.
- BASNER, M., SAMEL, A. & ISERMANN, U. 2006. Aircraft noise effects on sleep: Application of the results of a large polysomnographic field study. *The Journal of the Acoustical Society of America*, 119, 2772-2784.
- BRADLEY, M. 1999. *The International affective digitized sounds (IADS): stimuli, instruction manual and affective ratings*, NIMH Center for the Study of Emotion and Attention.
- BRADLEY, R. A. & TERRY, M. E. 1952. Rank Analysis of Incomplete Block Designs: I. The Method of Paired Comparisons. *Biometrika*, 39, 324-345.
- BROADBENT, D. E. 1980. Noise in relation to annoyance, performance, and mental health. *The Journal of the Acoustical Society of America*, 68, 15-17.
- BROCOLINIA, L., LAVANDIERA, C., MARQUIS-FAVREB, C., QUOYC, M. & LAVANDIERB, M. 2012. Prediction and explanation of sound quality indicators by multiple linear regressions and artificial neural networks. *Proceedings of the Acoustics 2012 Nantes Conference*. Nantes, France.
- CHO, Y. T., BOLTON, J. S. & HALD, J. 2005. Source visualization by using statistically optimized near-field acoustical holography in cylindrical coordinates. *The Journal of the Acoustical Society of America*, 118, 2355-2364.
- CHOI, S., MOON, W., GANG, S. & HWANG, T. 2004. Human-based evaluation of sound from hard disk drives for noise control. *Microsystem Technologies*, 10, 640-648.
- D. J. OLDHAM, H. N. H. 1991. The acoustical performance of small close fitting enclosures, part 1: Theoretical Models. *J. Sound Vib.*, 150, 261-281.

- DANG-VU, T. T., MCKINNEY, S. M., BUXTON, O. M., SOLET, J. M. & ELLENBOGEN, J. M. 2010. Spontaneous brain rhythms predict sleep stability in the face of noise. *Curr Biol*, 20, R626-7.
- DI, G.-Q., ZHOU, X.-X. & CHEN, X.-W. 2015. Annoyance response to low frequency noise with tonal components: A case study on transformer noise. *Applied Acoustics*, 91, 40-46.
- DIN45631 1990. Berechnung des Lautstarkepegels and der Lautheit aus dem Gerduschspektrum. Verfahrennach.
- DIN45631/A1 2008. Berechnung des Lautstärkepegels und der Lautheit aus dem Geräuschspektrum –Verfahren nach.
- EGAB, L. & WANG, X. 2016. Objective evaluation of interior trim effects on sound quality and noise reduction of a coupled plate cavity system. *Mechanical Systems and Signal Processing*, 70-71, 919-931.
- ELLERMEIERA, W., ZEITLERA, A. & FASTLB, H. 2004. Predicting annoyance judgments from psychoacoustic metrics: Identifiable versus neutralized sounds. *Inter-noise 2004*.
- ELMENDORST, E. M., QUEHL, J., MULLER, U. & BASNER, M. 2014. Nocturnal air, road, and rail traffic noise and daytime cognitive performance and annoyance. *J Acoust Soc Am*, 135, 213-22.
- FASTL, H. 2010. Alternatives to A-wieghting: Psychoacoustic background. *J Acoust Soc Am*, 128.
- FASTL, H. & ZWICKER, E. 2007. Psychoacoustics Facts and Models. *Springer Berlin Heidelberg*.
- FIELDS, J. M., DE JONG, R. G., GJESTLAND, T., FLINDELL, I. H., JOB, R. F. S., KURRA, S., LERCHER, P., VALLET, M., YANO, T., GUSKI, R., FELSCHER-SUHR, U. & SCHUMER, R. 2001. Standardized General-Purpose Noise Reaction Questions for Community Noise Surveys: Research and a Recommendation. *Journal of Sound and Vibration*, 242, 641-679.
- FILIPPI, P. 1983. *Theoretical Acoustics and Numerical Techniques*, Springer-Verlag Wien GmbH.
- GAO, F., YAN, Y. & YAP, F. F. 2003. Vibro-acoustic interaction of components in Hard Disk Drive. *Microsystem Technologies*, 9, 496-500.
- GAO, F., YAP, F. F. & YAN, Y. 2005. Modeling of Hard Disk Drives for Vibration Analysis Using a Flexible Multibody Dynamics Formulation. *IEEE TRANSACTIONS ON MAGNETICS*, 41, 717-734.
- GAUTHIER, P.-A., SCULLION, W. & BERRY, A. 2017. Sound quality prediction based on systematic metric selection and shrinkage: Comparison of stepwise, lasso, and elastic-net algorithms and clustering preprocessing. *Journal of Sound and Vibration*, 400, 134-153.
- GOCKEL, H. E., FAROOQ, R., MUHAMMED, L., PLACK, C. J. & CARLYON, R. P. 2012. Differences between psychoacoustic and frequency following response measures of distortion tone level and masking. *J Acoust Soc Am*, 132, 2524-35.
- GORANSSON, P. 1995. A Weighted Residual Formulation of the Acoustic Wave Propagation Throught a Flexible Porous Material and a Comparison With a Limp Material Model. *Journal of Sound and Vibration*, 182, 479-494.
- GUIDATI, S. 2008. Auralisation and psychoacoustic evaluation of traffic noise scenaios. *J Acoust Soc Am*, 123, 3027.
- HALD, J. 2009. Basic theory and properties of statistically optimized near-field acoustical holography. *J Acoust Soc Am*, 125, 2105-20.
- HELLMAN, R. P. 1985. Perceived magnitude of two-tone-noise complexes: Loudness, annoyance, and noisiness. *J. Acoust. Soc. Am.*, 77, 1497-1504.
- HOU, J., JIANG, W. & LU, W. 2011. Application of a near-field acoustic holography-based diagnosis technique in gearbox fault diagnosis. *Journal of Vibration and Control*, 19, 3-13.

- HUANG, F., HE, Z., & PENG, W. 2006. An efficient prediction method for the Two-Dimensional coupled structural-acoustic analysis. *Acta Mechanica Solida Sinica*, 19, 327-333.
- IEC60050 1994. International Electrotechnical Vocabulary. *Electropedia*. British.
- ISO 226:2003. Acoustic -- Normal equal-loudness-level contours.
- ISO532B 1975. Acoustics-method for calculating loudness level.
- ISO7779, B. E. 2010. 7779:2010 - Acoustics. Measurement of airborne noise emitted by information technology and telecommunications equipment. BSI.
- ISO/TS15666 2003. Acoustics -- Assessment of noise annoyance by means of social and socio-acoustic surveys.
- JULIAN, S., LESTER, D. R. JR., MILTON, K. A. & TSAI W, JOYCE, N. 1998. *Classical Electrodynamics*, Reading, Mass. : Perseus Books.
- JANG, G. H., LEE, S. H. & JUNG, M. S. 2002. Free Vibration Analysis of a Spinning Flexible Disk–Spindle System Supported by Ball Bearing and Flexible Shaft Using the Finite Element Method and Substructure Synthesis. *Journal of Sound and Vibration*, 251, 59-78.
- JANG, G. H., SEO, C. H. & LEE, H. S. 2006. Finite element modal analysis of an HDD considering the flexibility of spinning disk–spindle, head–suspension–actuator and supporting structure. *Microsystem Technologies*, 13, 837-847.
- JANG, G. H., PARK, S. J., KIM, C. S., HAN, J. H. 2007. Investigation of the electromechanical variables of the spindle motor and the actuator of a HDD due to positioning and free fall. *Microsystem Technologies*, 13, 797-809.
- JIANG, J., CHEN, S., ZHANG, Q. & LIU, Z. 2002. Transient dynamic analysis of ferro-fluid bearing spindle motor. *Microsystem Technologies*, 8, 282-288.
- JINTANAWAN, T., SHEN, I. Y. & TANAKA, K. 2001. Vibration Analysis of Fluid Dynamic Bearing Spindles with Rotating–Shaft Design. *IEEE TRANSACTIONS ON MAGNETICS*, 37, 799-804.
- JUNYI, L. & BALINT, D. S. 2015. An inverse method to determine the dispersion curves of periodic structures based on wave superposition. *Journal of Sound and Vibration*, 350, 41-72.
- JUNYI, L., RUFFINI, V. & BALINT, D. 2016. Measuring the band structures of periodic beams using the wave superposition method. *Journal of Sound and Vibration*, 382, 158-178.
- KANE, P. V. & ANDHARE, A. B. 2016. Application of psychoacoustics for gear fault diagnosis using artificial neural network. *Journal of Low Frequency Noise, Vibration and Active Control*, 35, 207-220.
- KIM, G. T. & LEE, B. H. 1990. 3-D sound source reconstruction and field reproduction using the Helmholtz integral equation. *Journal of Sound and Vibration*, 136, 245-261.
- KNUDSEN, V. O. 1932. *Architectural acoustics*, J. Wiley & sons, inc.,.
- KOOPMANN, G. H., SONG, L. & FAHNLIN, J. B. 1989. A method for computing acoustic fields based on the principle of wave superposition. *The Journal of the Acoustical Society of America*, 86, 2433-2438.
- KROESEN, M., MOLIN, E. J. & VAN WEE, B. 2013. Measuring subjective response to aircraft noise: the effects of survey context. *J Acoust Soc Am*, 133, 238-46.
- LEE, J.-S., GOLDMANN, L. & EBRAHIMI, T. 2013. Paired comparison-based subjective quality assessment of stereoscopic images. *Multimedia Tools and Applications*, 67, 31-48.
- LI, D., CHENG, L., YU, G. H. & VIPPERMAN, J. S. 2007. Noise control in enclosures: modeling and experiments with T-shaped acoustic resonators. *J Acoust Soc Am*, 122, 2615-25.
- LIM, G., KIM, S., PARK, N.-C., PARK, K.-S., LEE, H.-C. & KIM, J.-H. 2014. Design Modifications to Improve the Antishock Performance of a Stamped Base for a 2.5-in HDD. *IEEE TRANSACTIONS ON MAGNETICS*, 50, 1-4.

- LUCE, R. D. 1959. *Individual choice behaviour: A theoretical analysis*, New York, Wiley.
- LYON, R. H. 1963. Noise Reduction of Small Enclosures. *The Journal of the Acoustical Society of America*, 35, 785-786.
- LYON, R. H. 2000a. *Designing for product sound quality*, Marcel Dekker, Inc.
- LYON, R. H. 2000b. Engineered sound quality coupling subjective reactions to engineering choices. *IEEE Ind. Appl. Mag.*
- MA, Y., CHIN, C. S. & WOO, W. L. 2017. Evaluating 2.5" Hard Disk Drive Noise Source Identification. *INTER-NOISE and NOISE-CON Congress and Conference Proceedings*, 255, 1782-1787.
- MA, Y. C., CHIN, C. S. & WOO, W. L. 2015. Neural Networks-Based Acoustic Annoyance Model for Laptop Hard Disk Drive. *International Journal of Electrical, Computer, Energetic, Electronic and Communication Engineering*, 9.
- MA, Y. C., CHIN, C. S., WOO, W. L. & GAO, B. 2016. An Acoustic Annoyance Study of Hard Disk Drive for Laptop. *IEEE Transactions on Magnetics*, 52, 1-9.
- MAIDANIK, G. 1962. Response of Ribbed Panels to Reverberant Acoustic Fields. *The Journal of the Acoustical Society of America*, 34, 809-826.
- Mats E. Nillson. 2007 A-weighted Sound Pressure Level as an Indicator of Short-term Loudness or annoyance of Road-traffic Sound. *Journal of Sound and Vibration*, 302, 197-207.
- MAYNARD, J. D., WILLIAMS, E. G. & LEE, Y. 1985. Nearfield acoustic holography: I. Theory of generalized holography and the development of NAH. *J. Acoust. Soc. Am.*, 78.
- MUZET, A. 2007. Environmental noise, sleep and health. *Sleep Med Rev*, 11, 135-42.
- NASMYTH, T. G. 1929. Noise and Annoyance. *The Lancet*, 213, 563-564.
- NEHETE, D. V., MODAK, S. V. & GUPTA, K. 2015. Structural FE model updating of cavity systems incorporating vibro-acoustic coupling. *Mechanical Systems and Signal Processing*, 50-51, 362-379.
- NG, A. K. & KOH, T. S. 2008a. Using psychoacoustics of snoring sounds to screen for obstructive sleep apnea. *30th Annual International IEEE EMBS Conference*. Vancouver, BC, Canada.
- NG, A. K. & KOH, T. S. 2008b. Using Psychoacoustics of Snoring Sounds to screen for obstructive sleep apnea. *30th Annual International IEEE EMBS Conference*. Vancouver, British Columbia, Canada.
- NICKOLAS VLAHOPOULOS, S.T. RAVEENDRA, CHARLES VALLANCE & SCOTT MESSER 1999. Numerical implementation and applications of a coupling algorithm for structural acoustic models with unequal discretization and partially interfacing surfaces. *Finite Element in Analysis and Design*, 32, 257-277.
- NOVAK, C. & REFAI-AHMED, G. 2005. Use of psychoacoustic metrics for the analysis of next generation computer graphic card noise. *ASME InterPACK*. California, USA.
- NOVAK, C., ULE, H., GASPAR, R. & WILEY, R. 2005. Use of psychoacoustic metrics for the analysis of next generation computer cooling fan noise. *Canadian Acoustics*, 3, 34-35.
- ÖHRSTRÖM, E., SKÅNBERG, A., SVENSSON, H. & GIDLÖF-GUNNARSSON, A. 2006. Effects of road traffic noise and the benefit of access to quietness. *Journal of Sound and Vibration*, 295, 40-59.
- PANZA, M. J. 2014. A Mathematical Images Group Model to Estimate the Sound Level in a Close-Fitting Enclosure. *Advances in Acoustics and Vibration*, 2014, 1-7.
- PARK, K., SUNG, S. & JANG, G. 2013. Magnetically induced vibration of a flexible rotating disk-spindle system due to the internal magnetic force arising from the spindle motor of a HDD. *Microsystem Technologies*, 19, 1529-1537.

- PERIS, E., WOODCOCK, J., SICA, G., SHARP, C., MOORHOUSE, A. T. & WADDINGTON, D. C. 2014. Effect of situational, attitudinal and demographic factors on railway vibration annoyance in residential areas. *J Acoust Soc Am*, 135, 194-204.
- PIERRETTE, M., MARQUIS-FAVRE, C., MOREL, J., RIOUX, L., VALLET, M., VIOLLON, S. & MOCH, A. 2012. Noise annoyance from industrial and road traffic combined noises: A survey and a total annoyance model comparison. *Journal of Environmental Psychology*, 32, 178-186.
- PREZELJ, J., LIPAR, P., BELŠAK, A. & ČUDINA, M. 2013. On acoustic very near field measurements. *Mechanical Systems and Signal Processing*, 40, 194-207.
- RAYLEIGH, J. 1896. *The Theory of Sound*, Macmillan.
- ROHRMEIER, C., FISCHER, R., MERZ, A. K., ETTL, T., HERZOG, M. & KUEHNEL, T. S. 2015. Are subjective assessments of snoring sounds reliable? *Eur Arch Otorhinolaryngol*, 272, 233-40.
- ROHRMEIER, C., HERZOG, M., HAUBNER, F. & KUEHNEL, T. S. 2012. The annoyance of snoring and psychoacoustic parameters: a step towards an objective measurement. *Eur Arch Otorhinolaryngol*, 269, 1537–1543.
- RUBER, K., KANAPATHIPILLAI, S. & RANDALL, R. 2015. Sound Transmission Loss of a Panel Backed by a Small Enclosure. *Journal of Low Frequency Noise, Vibration and Active Control*, 34, 549 – 568.
- SARKISSIAN, A. 2005. Method of superposition applied to patch near-field acoustic holography. *The Journal of the Acoustical Society of America*, 118, 671.
- SCHÄFFER, B., SCHLITTEMEIER, S. J., PIEREN, R., HEUTSCHI, K., BRINK, M., GRAF, R. & HELLBRÜCK, J. 2016. Short-term annoyance reactions to stationary and time-varying wind turbine and road traffic noise: A laboratory study. *The Journal of the Acoustical Society of America*, 139, 2949-2963.
- SCHELL-MAJLOOR, L., RENNIES, J., EWERT, S. D. & KOLLMEIER, B. 2015. Application of psychophysical models for audibility prediction of technical signals in real-world background noise. *Applied Acoustics*, 88, 44-51.
- SCHUHMACHER, A., HALD, J., RASMUSSEN, K. B. & HANSEN, P. C. 2003. Sound source reconstruction using inverse boundary element calculations. *The Journal of the Acoustical Society of America*, 113, 114-127.
- SHEN, I. Y. & KU, C.-P. R. 1997. A Nonclassical Vibration Analysis of a Multiple Rotating Disk and Spindle Assembly. *J. Appl. Mech* 64, 165-174.
- SHEPHERD, M. 1975. Pollution, Noise, and Mental Health. *The Lancet*, 305, 322-324.
- SONG, L., KOOPMANN, G. H. & FAHNLIN, J. B. 1991. Numerical errors associated with the method of superposition for computing acoustic fields. *The Journal of the Acoustical Society of America*, 89, 2625-2633.
- SOTTEK, R. 2015. Psychoacoustically based tonality model for the evaluation of noise with tonal components. *The Journal of the Acoustical Society of America*, 137, 2320-2320.
- STEINER, R. & HALD, J. 2000. Near-field acoustical holography without the errors and limitations caused by the use of spatial DFT. *International Journal of Acoustics and Vibration*, 6, 83-89.
- STRAUSS, W. A. 2007. *Partial Differential Equations: An Introduction*, Wiley.
- SUN, X., XUE, Z., ZHU, J., GUO, Y., YANG, Z., CHEN, L. & CHEN, J. 2016. Suspension Force Modeling for a Bearingless Permanent Magnet Synchronous Motor Using Maxwell Stress Tensor Method. *IEEE Transactions on Applied Superconductivity*, 26, 1-5.
- SUZUKI, T. 2006. Identification of multipole noise sources in low Mach number jets near the peak frequency. *The Journal of the Acoustical Society of America*, 119, 3649.

- TAJADURA-JIMÉNEZ, A. 2008. *Embodied psychoacoustics: Spatial and multisensory determinants of auditory-induced emotion* THE DEGREE OF DOCTOR OF PHILOSOPHY CHALMERS UNIVERSITY OF TECHNOLOGY
- TANDON, N., RAO, V. V. P. & AGRAWAL, V. P. 2006. Vibration and noise analysis of computer hard disk drives. *Measurement*, 39, 16-25.
- TANG, W.-C. 2007. Measurement of Vibroacoustic Performance of Close-Fitting Honeycomb Sandwich Structures. *Building Acoustics*, 14, 267–281.
- TÖPKEN, S., VERHEY, J. & WEBER, R. 2010. Perceptual space of multiple complex tones. *Proceedings of 20th International Congress on Acoustics*. Sydney, Australia.
- TORIJA, A. J. & FLINDELL, I. H. 2014. Differences in subjective loudness and annoyance depending on the road traffic noise spectrum. *J Acoust Soc Am*, 135, 1-4.
- TSENG, C. W., SHEN, J. Y. & SHEN, I. Y. 2003. Vibration of Rotating-Shaft HDD Spindle Motors With Flexible Stationary Parts. *IEEE TRANSACTIONS ON MAGNETICS*, 39, 794-799.
- VEGGERBERG, K. & ZHENG, A. 2009. Real-time noise source identification using field programmable gate array (FPGA) technology. *Proceedings of Meetings on Acoustics*, 5.
- VERGNAULT, E., MALASPINAS, O. & SAGAUT, P. 2013. Noise source identification with the lattice Boltzmann method. *J Acoust Soc Am*, 133, 1293-305.
- VERONESI, W. A. & MAYNARD, J. D. 1987. Nearfield acoustic holography (NAH) II. Holographic reconstruction algorithms and computer implementation. *The Journal of the Acoustical Society of America*, 81, 1307-1322.
- VERONESI, W. A. & MAYNARD, J. D. 1989. Digital holographic reconstruction of sources with arbitrarily shaped surfaces. *The Journal of the Acoustical Society of America*, 85, 588-598.
- WALLACE, C. E. 1972. Radiation Resistance of a Rectangular Panel. *The Journal of the Acoustical Society of America*, 51, 946-952.
- WANG, J. W., JIA, Q. W. & WANG, Y. Y. 2010. Hard Disk Drive Seeking Acoustics Reduction By a New Two-Degree-of-Freedom Seeking Controller. *IEEE Transactions on Magnetics*, 46.
- WANG, M. E. & CROCKER, M. J. 1983. On the application of coherence techniques for source identification in a multiple noise source environment. *J Acoust Soc Am*, 74, 861.
- WANG, R., CHEN, J. & LI, J. Q. 2012. Study of the influence factors on the accuracy of sound field reconstruction based on wave superposition method. *Journal of Physics: Conference Series*, 364, 012045.
- WANG, Y. S., SHEN, G. Q. & XING, Y. F. 2014. A sound quality model for objective synthesis evaluation of vehicle interior noise based on artificial neural network. *Mechanical Systems and Signal Processing*, 45, 255-266.
- WANG, Z. & WU, S. F. 1997. Helmholtz equation-least-squares method for reconstructing the acoustic pressure field. *The Journal of the Acoustical Society of America*, 102, 2020-2032.
- WICKELMAIER, F. & SCHMID, C. 2004. A Matlab function to estimate choice model parameters from paired-comparison data. *Behavior Research Methods, Instruments, & Computers*, 36, 29-40.
- WILLEMSSEN, A. M. & RAO, M. D. 2010. Characterization of sound quality of impulsive sounds using loudness based metric. *Proceedings of 20th International Congress on Acoustics*. Sydney, Australia.
- WILLIAMS, E. G. 1999. *Fourier acoustics sound radiation and nearfield acoustical holography*, San Diego, Calif. : Academic Press.
- WILLIAMS, E. G. & MAYNARD, J. D. 1980. Holographic Imaging without the Wavelength Resolution Limit. *Physical Review Letters*, 45, pp.554-557.

- WILLIAMS, E. G. & MAYNARD, J. D. 1982. Numerical evaluation of the Rayleigh integral for planar radiators using the FFT. *J Acoust Soc Am*, 72, 2020-2030.
- WOLFGANG, K. H. P. & MELBA, P. 1962. *Classical Electricity and Magnetism 2nd edn*, (Reading, MA: Addison-Wesley.
- WOOD, R. 2009. Future hard disk drive systems. *Journal of Magnetism and Magnetic Materials*, 321, 555-561.
- WU, H., JIANG, W. & ZHANG, H. 2016. A mapping relationship based near-field acoustic holography with spherical fundamental solutions for Helmholtz equation. *Journal of Sound and Vibration*, 373, 66-88.
- WU, S. F. 2000. On reconstruction of acoustic pressure fields using the Helmholtz equation least squares method. *The Journal of the Acoustical Society of America*, 107, 2511-2522.
- WU, T. W. & SEYBERT, A. F. 1991. A weighted residual formulation for the CHIEF method in acoustics. *The Journal of the Acoustical Society of America*, 90, 1608-1614.
- YANAGISAWA, H., YOKOO, S., MURAKAMI, T., OHTOMI, K. & HOSAKA, R. Effect of Tonal Harmonic Feature in Product Noise on Emotional Quality. 2011 London. Springer London, 469-476.
- YANG, J. P. & CHEN, S. X. 2002. Vibration predictions and verifications of disk drive spindle system with ball bearings. *Computers and Structures*, 80, 1409-1418.
- YANG, M., DE COENSEL, B. & KANG, J. 2015. Presence of 1/f noise in the temporal structure of psychoacoustic parameters of natural and urban sounds. *J Acoust Soc Am*, 138, 916-27.
- ZHANG, X. Z., THOMAS, J. H., BI, C. X. & PASCAL, J. C. 2012. Reconstruction of nonstationary sound fields based on the time domain plane wave superposition method. *J Acoust Soc Am*, 132, 2427-36.
- ZHANG, Z., VLAHOPOULOS, N., RAVEENDRA, S. T., ALLEN, T. & ZHANG, K. Y. 2000. A computational acoustic field reconstruction process based on an indirect boundary element formulation. *The Journal of the Acoustical Society of America*, 108, 2167-2178.